ELECTROKINETIC AND POROELASTIC CHARACTERIZATION OF POROUS MEDIA: APPLICATION TO CO_2 STORAGE MONITORING

Dissertation

for the purpose of obtaining the degree of doctor
at Delft University of Technology
by the authority of the Rector Magnificus prof.dr.ir. T.H.J.J. van der Hagen
chair of the Board for Doctorates
to be defended publicly on
Monday 12 March 2018 at 15:00 o'clock

by

Oleksandr KIRICHEK

Master of Science in Civil Engineering,
Prydniprovska State Academy of Civil Engineering and Architectur, Ukraine
born in Dnipropetrovsk, Ukraine.

This dissertation has been approved by the promotor and the copromotor.

Composition of the doctoral committee:

Rector Magnificus,	chairman
Prof. dr. ir. C.P.A. Wapenaar	Delft University of Technology, promotor
Dr. R. Ghose	Delft University of Technology, copromotor

Independent members:

Prof. dr. ir. E.C. Slob	Delft University of Technology
Prof. dr. W.R. Rossen	Delft University of Technology
Dr. E. Dubois	Sorbonne University, France
Dr. J.H. Brouwer	TNO Utrecht
Dr. C. Chassagne	Delft University of Technology

Keywords: electrokinetics, dielectric spectroscopy, poroelasticity, CO_2 monitoring

Cover by: Alex Kirichek

ISBN 978-94-6186-902-9

An electronic version of this dissertation is available at
http://repository.tudelft.nl/.

CONTENTS

LIST OF ABBREVIATIONS

AC	Alternating Current
ADC	Analog-to-Digital Converter
CCS	Carbon Capture and Storage
CT	Computed Tomography
DC	Direct Current
DS	Dielectric Spectroscopy
EIS	Electrical Impedance Spectroscopy
EP	Electrode Polarization
ERT	Electrical Resistivity Tomography
FIFO	First In First Out
FPGA	Field Programmable Gate Array
IP	Induced Polarization
NI	National Instrument
SIP	Spectral Induced Polarisation
VI	Virtual Instrument
VSP	Vertical Seismic Profiling

1

INTRODUCTION

Starting is easy,
persistence is an art.

Proverb

In the process of carbon capture and storage (CCS), waste CO_2 is captured from large concentrated point sources e.g., fossil fuel power plants, transported to a storage site, and then deposited in high-porosity and high-permeability geological formations in such way that the stored CO_2 can no more enter the atmosphere. It is a potential means for reducing the anthropogenic contribution of fossil fuel emissions to global warming and ocean acidification.

Sufficient and robust assessment of the potential storage site, storage complex and surrounding area are the first critical steps in ensuring that a potential storage site has no significant risk of leakage and eliminate as far as possible negative effects and any risks to the environment and human health. A full compliance with health, safety and environment standards has to be ensured during CO_2 injection and permanent storage.

According to a report of the European Commission [European Commission, 2011], "the goal of the characterization of the storage site is to assess the site's containment, injectivity, capacity, integrity, hydrodynamics, and monitorability in order to ensure safe and permanent storage of CO_2. Collection of primary data either through evaluation of existing data or through exploration activities is critical for evaluating the suitability of a particular site. The modeling and data analysis needs to provide sufficient confidence on the evaluation of containment, injectivity, capacity, integrity, and hydrodynamics of the site.

The process of identifying a site will consist of a series of assessments that progressively change scale, commencing with regional assessments to basin-scale assessments to more detailed exploration of specific locations. The usual locations for geological disposal of CO_2 are depleted hydrocarbon reservoirs and deep saline aquifers. The saline

aquifers are more numerous than depleted hydrocarbon reservoirs, and they have significantly more pore volume available for geological storage of CO_2. The characterization of these aquifers requires detailed studies because they are typically not explored for prospecting. Fractures, faults and existing wellbores are critical discontinuities along which release of pressure, CO_2 phase changes and CO_2 leakage can occur.

The site characterization has to be based on data specifically oriented towards CO_2 storage. Characterization based primarily on data acquired for the purpose of oil and gas exploration may be incorrectly focused, as the data may have been acquired in an inappropriate manner or at incorrect geological locations for CO_2 storage." Thus, new CO_2-storage-oriented surveys have to be conducted for further prospecting. Geophysical surveying is well suited for CO_2 storage monitoring. Time-lapse seismic surveys have been successfully tested at Ketzin and Sleipner CO_2 storage sites [Arts et al., 2004, Lüth et al., 2011]. The tests reveal a high potential for tracking the CO_2 plume propagation in the reservoir. Electrical methods are particularly suited for CO_2 storage monitoring in saline aquifers since electrical properties are strongly controlled by the ionic characteristics of the pore-filling fluids. Hence, the injection of CO_2 will result in an imminent contrast in conductivity during the CO_2 injection in the reservoir. In the past the feasibility of CO_2 monitoring has been investigated using geoelectrical methods at Ketzin storage site (Germany). The monitoring has been conducted by means of cross-hole and surface-to-downhole electrical resistivity tomography after CO_2 was injected in a saline aquifer [Kiessling et al., 2010, Schmidt-Hattenberger et al., 2011]. These studies proved that geolectrical methods have sufficient potential to track the stored CO_2 in the reservoir.

The uncertainty in the geophysical interpretation of the CO_2 storage monitoring data can be unacceptably large [Chadwick et al., 2008]. Therefore, laboratory experiments are required for calibrating the field data to facilitate the field data processing and interpretation. The advantage of laboratory measurements is in defined geometries and boundary conditions of the investigated media. The core samples can be cored out from the CO_2 storage reservoir and used for different CO_2 and water injection scenarios. Geophysical seismic and electrical measurements can be continuously carried out during CO_2 and water saturation processes into reservoir rock. Later, these measurements can serve as a reference for field data interpretation.

Both seismic and electrical measurements are sensitive to the properties of pore fluids and reservoir rocks. Thus, these measurements can provide quantitative information about alterations in subsurface structures and processes which can occur during the CO_2 injection and permanent storage. Quantitative analyses of geophysical data require a detailed understanding of the underlying physics. Both methods are particularly sensitive to a wide range of reservoir properties (see Table 1.1) The prediction of these parameters can be done rigorously when the values of the physical parameters involved are more accurately known. Firstly, the geometries and composition of the reservoir and/or cap rock can be tailored in order to increase signal-to-noise ratio of the acquired data. This can facilitate verification of different acquisition geometries and data processing methods. Secondly, the temperature, pore and confining pressures, and composition of pore-filling material can be well-controlled by experimental setup. The controlled nature of laboratory experiment provide a desired equilibrium of the system, e.g. desired phase of

injected CO_2. Hence, the link between geophysical parameters, reservoir properties and pressure/temperature conditions can be investigated systemically in the laboratory.

Table 1.1: Properties of the CO_2 storage reservoir that can be detected with seismic and electrical geophysical methods

Electrokinetic theory	Poroelastic theory
porosity	porosity
fluid saturation	fluid saturation
water salinity	permeability
grain size	viscosity
temperature	grain and fluid densities
zeta potential	solid and fluid bulk moduli

The goal of this research is to develop and experimentally validate a new integrated geophysical quantitative approach for characterization in order to assess the properties of the CO_2 storage reservoir and their dynamic changes.

The thesis is structured as follows. Chapter 2 introduces a new laboratory setup which was designed and built to investigate ultrasonic and electrical properties of the porous reservoir rock under elevated pressures and temperatures. This setup allows to perform different injection scenarios and monitor the changes in a reservoir by ultrasonic and electrical measurements. The measurements are conducted under realistic in-situ conditions simultaneously. In Chapter 3, innovative analytical expressions for the electrokinetic response of granular media are presented. The derived models are applied to available laboratory measurements on porous media representing CO_2 storage reservoir at any salinity. A new practical approach presented in Chapter 4 accounts for extracting the bulk polarization signature from the captured electrical response of CO_2- and water-saturated sandstone by decoupling electrode polarization and pseudo-inductance effects. As the next step, in Chapter 5 the developed analytical theory is applied to predict the reservoir properties from the obtained bulk polarization of the porous rock. Important acoustic attributes in a porous medium, P-wave velocity dispersion and attenuation, are estimated from the ultrasonic laboratory data and modeled using pertinent theories of poroelasticity in Chapter 6. Chapter 7 discusses the possibility of simultaneous use of electrical and acoustic data for quantitative reservoir characterization. Low frequency and high frequency integration examples are particularly analyzed. Finally, conclusions of this work are provided in Chapter 8.

2

EXPERIMENTAL SETUP FOR CAPTURING ELECTRICAL AND SEISMIC SIGNATURES OF RESERVOIR ROCK DURING THE CO_2 STORAGE

The highest activity a human being can attain is learning for understanding, because to understand is to be free.

Baruch Spinoza

In this chapter a new laboratory facility, that has been built for the CO_2 sequestration purposes, is presented. The setup allows monitoring of the CO_2 plume migration within a reservoir rock by means of seismic and electrical geophysical measurements. Core flooding experiments can be conducted under realistic reservoir pressure and temperature conditions to mimic real CO_2 injection and storage scenarios. The Dielectric Spectroscopy (DS) method is adapted for the purpose of CO_2 front monitoring by means of measuring magnitude and phase of complex electrical impedance. Seismic transmission data is acquired continuously and related to the reflection data that is recorded periodically. Two laboratory experiments are presented in order to verify the temperature and pressure dependence of seismic and DS measurements captured during CO_2 saturation in a reservoir rock. The developed setup can be used to establish the range of seismic and electrical properties for a wide range of temperatures and pressures.

2.1. INTRODUCTION

Currently, there is a lack of geophysical data for CO_2 monitoring under various physical conditions and ambiguity on theories explaining seismic velocity dispersion and electrical polarization mechanisms. The laboratory environment is suitable for verification of geophysical models which can be relevant for CO_2 storage monitoring. These models can be tested in the laboratory before their deployment in the field. This can help to define boundary conditions of the models and check the sensitivity of geophysical properties to internal and external factors. These tests can occasionally result in reliable geophysical monitoring methods which can provide a scientifically-proven quantification of CO_2 storage monitoring.

Seismic methods are widely used to measure P-wave and S-wave velocities (V_p and V_s) and attenuation, of rocks at the laboratory conditions [Subramaniyan et al., 2014, Winkler and Plona, 1982]. Theses measurements can be then used to predict reservoir and fluid mobility properties. One of the first CO_2-related laboratory studies was done by Wang and Nur [1989] for Enhanced Oil Recovery purposes. The authors measured P- and S-wave velocities before and after CO_2 injection into reservoir rock which was initially saturated with n-hexadecane. Later on seismic velocities were measured during CO_2 injection into core samples which were initially saturated by an oil/water mixture [Wang et al., 1998]. In both cases, the authors conducted their experiments under realistic reservoir conditions. The measurements showed that P-velocities were very sensitive to CO_2 injection while S-velocities were less effected. One of the first studies that are related to CO_2 storage were done by Xue and Ohsumi [2004] and Xue et al. [2005]. Using an array of sixteen piezoelectric transducers, the authors monitored the gaseous CO_2 front propagation in a water-bearing reservoir rock. It was shown that the largest velocity decrease can be measured by injecting supercritical CO_2 [Xue and Lei, 2006]. As a follow up, Lei and Xue [2009] developed tomographic images of relative attenuation coefficient to refine their work in mapping CO_2 migration in a water-saturated sandstone. They reported that the attenuation coefficient increased most when supercritical CO_2 was injected. Purcell et al. [2010] performed seismic velocity measurements on a sandstone at reservoir temperatures varying pore pressure while maintaining constant confining pressure. Their results showed large velocity fluctuations with phase changes. Alemu et al. [2013] utilized computed tomography (CT) methods to monitor the CO_2 distribution into brine-saturated sandstone through acoustic velocity variations. Numerous works were dedicated to velocity measurements during CO_2 injection in various type of porous rocks [e.g., Kim et al., 2016, Lebedev et al., 2013, Siggins et al., 2010, Yam, 2011, Zemke et al., 2010].

Leaving aside seismic methods, there are not much laboratory investigations that are dedicated to electrical measurement for CO_2 storage monitoring. Nakatsuka et al. [2010] measured direct current (DC) electrical resistivity during CO_2 flooding in reservoir rocks under reservoir conditions to predict CO_2 saturations. This work was extended further and combined with seismic velocity measurements by Kim et al. [2013] and Kim et al. [2016]. Recently the applicability of the alternating current (AC) electrical methods to CO_2 storage monitoring has also been studied in laboratory [e.g., Börner et al., 2013, 2016, Kremer et al., 2016]. In these works the effort is made to use measured complex electrical conductivity for CO_2 storage monitoring. These AC methods can provide ad-

ditional information about the rocks, e.g. grain size and surface conductivity. Electrical measurements on saturated rocks are typically conducted in the laboratory in the frequency range between 0.01 Hz and 3 MHz [e.g., Börner et al., 1996, Kavian et al., 2012, Lesmes and Frye, 2001, Slater and Glaser, 2003]. Typically, a four electrodes system is utilized for Spectral Induced Polarization (SIP) measurements at frequencies between 0.01 Hz and 10 kHz. These measurements correspond to the frequency range of the field geophysical surveys. The impedance measurements at higher frequencies, 20 Hz - 5 MHz, are conventionally called Electrical Impedance Spectroscopy (EIS) or Dielectric Spectroscopy (DS). This method can be utilized with a two- or four-electrode system. The former can be used if the electrode polarization contribution is negligible or can be easily compensated for [Buck, 1969]. The latter helps to minimize the electrode polarization effect [MacDonald and Kenan, 1987]. The interpretation of the measurements is difficult due to the interference of various polarization effects [Kemna et al., 2012]. These effects may overlap each other in the frequency domain, making the interpretation of the measured data even more challenging. Therefore, the unwanted effects need to be minimized during designing of the setup or compensated using equivalent circuit theory during the data processing [Zimmermann et al., 2008].

Core-flooding experiments in the context of CO_2 storage are typically conducted under elevated pressure (P) and temperature (T) conditions, i.e. P>75 bar and T>35 °C, to mimic real conditions of a CO_2 sequestration reservoir [Sun et al., 2016]. These experiments provide additional information about alterations of reservoir properties due to CO_2 injection. Typically, core-flooding experiments are conducted to investigate the CO_2 behavior during and after the injection into reservoir rock. These experiments are usually carried out in a controlled pressure-temperature-volume systems. Therefore, core-flooding experiments are coupled to a geophysical acquisition system since in this case the pore and confining pressures as well as temperature can be reliably controlled during simultaneous ultrasonic and electrical measurements in the laboratory environment. The goals of using such a dedicated and extensive laboratory facility for geophysical monitoring of CO_2 storage are as follows:

1. applying realistic boundary conditions for the reservoir properties (e.g. confining and pore pressures, temperature, saturation, permeability, salinity, etc.);
2. testing realistic field geometry (cap rock, far field effect);
3. confirming novel ideas, for example, joint seismic and electrical monitoring that can potentially reduce the uncertainties in reservoir characterization;
4. implementing in the laboratory seismic array measurements with surface-seismic acquisition geometry;
5. measuring frequency-dependent seismic and electrical properties;
6. testing wide range of frequencies which are used in AC electrical measurements;
7. capturing the effects of the different polarization mechanisms which occur in porous media;
8. predicting the phase of the fluid that is contained in the pore space;

In this research a new laboratory setup was developed at Delft University of Technology. The goal of this chapter is to show the utility of the developed setup and to investigate the sensitivity of ultrasonic and electrical measurements. First, a description of the setup and its features is presented. Then, the sensitivity of ultrasonic and electrical properties of saturated porous rocks under elevated pressures and temperatures is investigated. In particular, two different injection scenarios are considered under realistic in-situ conditions. Ultrasonic and electrical measurements are performed for continuous monitoring of the changes in the reservoir during injections of NaCl solution and supercritical CO_2.

2.2. DESCRIPTION OF THE SETUP

2.2.1. TESTING MATERIAL

Several quarried sandstone rocks are used as standard porous media for laboratory experiments. The data obtained from these tests are usually compared with similar data derived from experiments conducted using reservoir cores. These rocks are chosen because they are relatively inexpensive, readily available, and relatively homogeneous. In this study the experiments are conducted on Bentheimer sandstone, which is an outcrop sandstone from the Gildehausen quarry, near the village of Bentheim (Germany). This sedimentary rock has predominantly sand-sized grains which are composed of quartz held together by silica. The relatively high porosity and permeability of Bentheimer sandstone makes it a good testing material for core-flood experiments. Some physical properties of this Bentheimer sandstone are listed in Table 2.1 [Peksa et al., 2015].

Table 2.1: Physical and mechanical properties of Bentheimer sandstone

Property	Value
Mineral composition	95% quartz 3% feldspar 2% kaolinite
Sorting	well-sorted
Grain bonding	contacts
Grain diameter	0.1 - 0.3 mm
Porosity	19-25%
Permeability	1 - 1.5 D
Poissons's ratio	0.22
Deformation modulus	18.38 GPa
Maximum stress	38.93 MPa

The tested core sample has the following dimensions: $0.3 \times 0.074 \times 0.03$ m^3. It is cored out of a single Bentheimer sandstone block with an average porosity of 22%. The sample is cored perpendicular to the bedding and dried in an oven for 24 hours. In order to measure the electrical properties of the rock, in total 8 pairs of planar electrodes are positioned on to the lateral sides of the core. Figure 2.1 (a) shows 6 pairs of electrodes which are attached to the widest side of the core. These electrodes are made with a cross-sectional area of 0.05×0.01 m^2. Two pairs of electrodes are glued to the narrowest side of

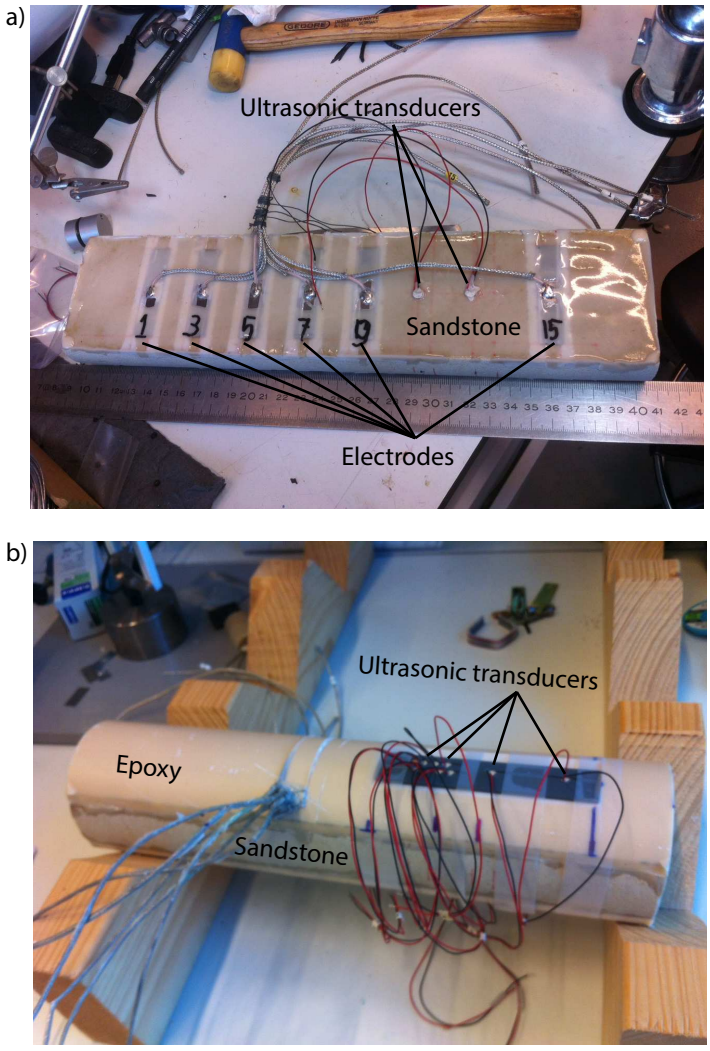

Figure 2.1: a) Positioning of electrodes and seismic transducers on the sandstone core. b) Coupling of the epoxy layer with ultrasonic transducers to the core.

the core. These electrodes have dimensions of 0.02×0.01 m^2.

Piezoelectric transducers are used to acquire the ultrasonic signal from the rock. Two transducers are coupled to the core as is shown in Figure 2.1 (a). The next stage is the building of two epoxy layers on both widest sides of the core. This step is shown in Figure 2.1 (b). The purpose of the layered sample is to mimic the cap rock and the reservoir. The plate with ultrasonic transducers is fixed on top of the epoxy layer. The positioning of the transducers is shown in Figure 2.1 (c) Three thermocouples are used in order to ensure the temperature equilibrium over the length of the core. Two thermocouples

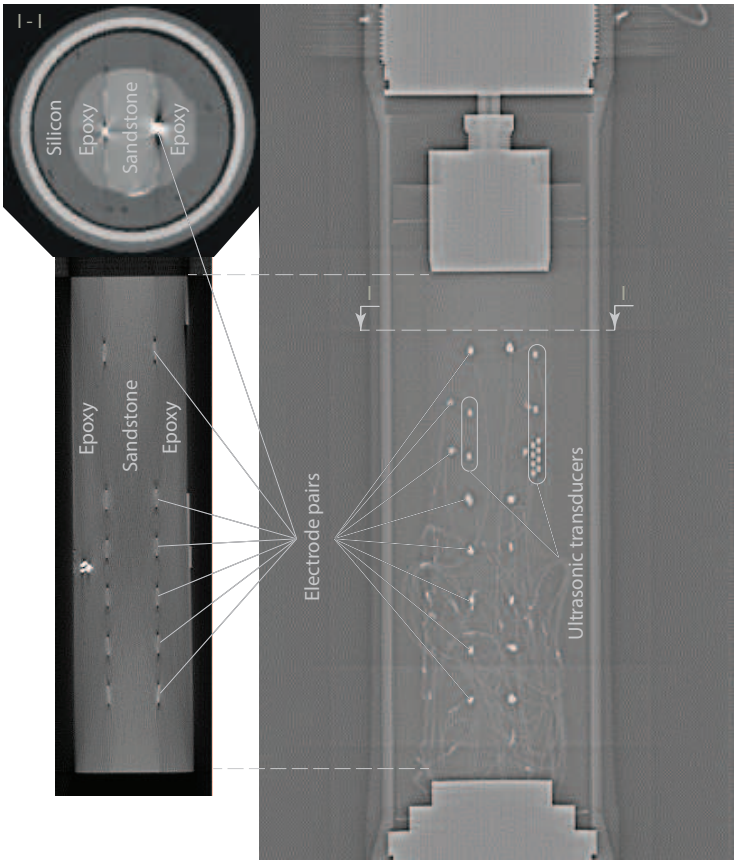

Figure 2.2: CT-scan of the sample inside the pressure chamber. A more detailed description of the sample is given in Appendix

are implemented inside the core and one thermocouple gives the temperature of the injected fluid.

The final step of building the sample is encasing of the core into a silicone rubber sleeve. The silicone sleeve is used to ensure that no fluid seepage occurs between the core holder and the core. The sleeve prevents direct fluid contact within the vessel. The ductility of the sleeve allows a confining overburden pressure to be transferred to the core to simulate elevated reservoir pressure. The core within the sleeve is placed inside a core holder which is capable of simulating reservoir pressures up to 600 bar. This pressure is applied by filling the annular space between the silicone sleeve and the core holder with light oil and then compressing the oil with an ISCO syringe pump to obtain the desired overburden pressure. The core holder has a vertical orientation in order to minimize the gravitational instabilities and fingering effects during the fluid injections. A lateral CT-scan of the sample illustrating the positioning of electrode pairs and seismic transducers is presented in Figure 2.2.

Figure 2.3: Experimental setup. 1 – sample in the pressure vessel, 2 – oven, 3, 4, 5 – ISCO pumps, 6 – density meter, 7 – pressure difference gauge, 8 – strip chart recorder, 9 – Agilent multiplexer switch, 10 – Wayne Kerr Precision Component Analyser 6640A, 11 – Agilent 33210A function generator, 12 – ENI 2100L RF amplifier, 13 – NI PXIe-1082 chassis with NI PXIe-7962R FlexRIO FPGA and NI FlexRIO modules, 14 – Multichannel bridge, 15 – Yokogawa DL4200 oscilloscope. More detailed description of the sample is given in Appendix

2.2.2. LABORATORY SETUP

A photo of the complete experimental setup is shown in Figure 2.3. The pressure cell is contained in a temperature controlled oven which duplicates precise reservoir conditions of temperature and eliminates complication of data analysis due to fluctuations in the external ambient temperature. The use of the correct reservoir temperature and pressure ensures that the required phase of the injected fluid will occur within the core sample.

Both ends of the core holder contain a port for fluid injection. Two pressure transducers and two thermocouples are mounted directly across the core holder and measure the pressure differential and temperature between the injection and the production ends. Pressure transducers and thermocouples are directly connected to a strip chart recorder which provides a continuous pressure temperature profiles of the test. A digital readout also appears on a multi-channel terminal from which the test operator takes readings as a backup.

Two ISCO syringe pumps are used for injecting the fluids into the core. A third pump is utilized for controlling the confining pressure inside the pressure cell. All ISCO pumps are pulsation-free positive-displacement pumps. They can inject the fluids under various injection scenarios of constant flow-rate, constant pressure, constant pressure with

adjustable pressure ramp and reaching a target injection volume. The pumps could be operated directly using the keypads placed in front of them or using the monitoring software installed on a PC connected to the apparatus. Syringe pumps such as these provide a very smooth displacing action which eliminates pressure shocks to the core material. The pumps are capable of injecting at rates of 1 ml/min at pressures up to 250 bar with an accuracy of 0.01 ml. A flow meter is attached at the production side of the pressure cell. It is used to monitor the density of the injected fluid.

2.2.3. DIELECTRIC SPECTROSCOPY MEASUREMENTS

In this study a two-terminal electrode system is employed. Wayne Kerr Precision Component Analyzer 6640A is used as a measuring system to acquire the electrical impedance data over the frequency range between 20 Hz and 3 MHz. Eight planar electrode pairs, that are directly attached to the opposite lateral surfaces of the core, are connected by coaxial cables to the multiplexer switch which enables fast successive measurement between the electrode pairs. Each electrode is home-made using nickel foil. Figure 2.2 shows the positioning of the electrode pairs on the core. The distance between the electrode pairs is 0.02 m. All electrodes act as both current and potential terminals. The electrical properties of the specimens are determined by measuring the potential difference between the electrodes and the applied current across them. In most cases a sinusoidal excitation is imposed, and measurements of magnitude $|Z|$ and phase lag φ of the electrical impedance are repeated at different frequencies.

In order to obtain the true impedance of the specimen, the residual parameters associated with the test fixture must be removed from the measured data. Calibration measurements have been performed in open-circuit and short-circuit conditions. The short circuit measured the residual impedance in the test leads, and the open circuit measured the combined effect of the stray admittance and the residual impedance. Impedance measurements of highly conductive specimens may be significantly affected by cable inductance, normally at frequencies greater than 100 kHz. Therefore, the inductance of the cable has to be minimized by employing coaxial cables.

A proper calibration of the electrical system with material of known electrical properties is further required to investigate the accuracy of the measured data. In particular, a cell constant, which accounts for the different electric field distribution as a function of electrode spacing, has to be determined. In the case of a planer electrode pair, the cell constant F is the ratio between the cross-sectional area of the electrodes A and the distance between them d. This yields that the cell constant for electrode pairs 1, 2, 3, 4, 5, 8 and 6, 7 are $F_1 = 0.167$ and $F_2 = 2.7$, respectively.

2.2.4. ULTRASONIC MEASUREMENTS

An array of 10 ultrasonic transducers is fixed on top of the epoxy layer. The positioning and dimensions of transducers are shown in Figure 2.4. This geometry represents a scaled in-situ marine seismic survey acquisition geometry. To record reflection measurements, transducers S1-S2 and S3-S10 are used as sources and receivers, respectively. To acquire transmission data, transducers S11 and S12 are used as sources, while all other transducers serve as receivers.

P-wave Fuji Ceramics transducers of 1 MHz center frequency are used as sources

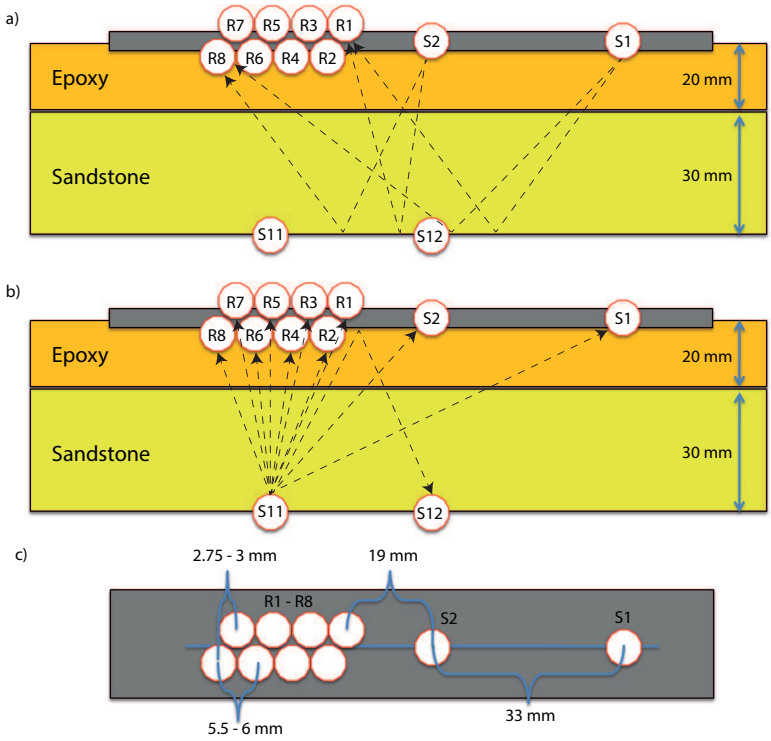

Figure 2.4: Schematic representation of the sample consisting of a plastic plate with ultrasonic transducers S1, S2, R1-R8 which is attached on to the top of the epoxy layer; two transducers S11 and S12 are coupled to the bottom layer of Bentheimer sandstone. All transducers can act as a source and a receiver. a) Scheme of periodic seismic measurements: S1 and S2 are used as sources and R1-R8 as receivers. b) Scheme of continuous seismic measurements: S11 is used as a source and all remaining transducers are used as receivers.

and receivers. The transducers are directly glued to the surface of the sample using an acoustic couplant. The source transducers are fed with a sine-wave signal from an Agilent 33210A function generator, the signal is afterwards amplified by 50 dB by means of an ENI 2100L RF amplifier. The measured signal is quality-controlled with a Yokogawa DL4200 oscilloscope. A multichannel acquisition system is used to acquire and store the data at a base station.

The acquisition workflow of the multichannel system is the following. The analogue outputs of the piezoelectric transducers are amplified and then connected to a digitizer. The digitizer's integrated field programmable gate arrays (FPGA) module performs the initial-stage signal processing by means of signal averaging. To improve the signal to noise ratio an averaging of the consecutive signal frames is performed. Preprocessed signals are sent to a base station where they are stored as binary files.

The National Instrument (NI) instrumentation hardware consists of NI PXIe-1082 chassis, NI PXIe-7962R FlexRIO FPGA module,a NI FlexRIO adapter module and a base station running the Microsoft Windows OS. Table 2.2 summarizes some relevant characteristics of the data acquisition system. As the bandwidth of the ultrasonic measure-

Table 2.2: Acquisition hardware parameters

Feature	Value Default value
Maximum system bandwidth	7 GB/s
FPGA	Virtex-5 SX50T
FPGA slices	8160
FPGA memory (block RAM)	4752 kbit
input channels	32
ADC input resolution	12 bits
ADC maximum sampling rate	50 MS/s
ADC analogue input range	2 Vpp
ADC analogue input impedance	100Ω

ments is relatively narrow, the performance of the above components should be sufficient to collect sufficient data.

The seismic acquisition programming is implemented in LabVIEW. As much of the functionality as possible is implemented as a Component Level IP. The CLIP provides clock management of the signal storage and averaging capabilities, test signal generation, and data serialization. The main LabVIEW components of the data acquisition application are, as is customary for this type of LabVIEW applications, a host Virtual Instrument (VI) and an FPGA VI. The host VI subsystem is responsible for reading data from one FPGA first in first out (FIFO) and writing it to a file. The data from four channels are serialized into one stream since there is a limit on the number of FIFO structures and each FPGA to host FIFO consumes block RAM of which the FPGA board possesses a limited amount. As a result, the design uses a total of eight FPGA to host FIFOs. The part of the FPGA VI reads data from the analog-to-digital converter (ADC) and sends it to the CLIP module. Afterwards, it reads the serialized averaged signals from the CLIP and sends it to the FPGA side of the FPGA to host FIFO. The FIFO is enabled only when there is a data available (every N frames where N is the averaging depth).

Table 2.3: Seismic acquisition parameters

Symbol	Description	Default value
f	sampling frequency	12.5 MHz
T	sample duration	80 ns
S	sampling buffer size	1024 samples
L	frame duration	81.92μs
N	averaging depth	8
W	averaging window duration	0.65538 ms

Each signal processing component is connected either to a counter or to an output of the ADC. Channels are serialized in groups of four and the output of the serializers constitute the output of the CLIP module.

The sampled data is stacked in order to maximize the signal-to-noise ratio. The hardware stacks every 256 successive signals, as opposed to the averaging in many conven-

tional averaging oscilloscopes. This is performed to reduce the amount of data that is transferred to the PC.

Table 2.3 shows a list of interdependent parameters utilized for seismic acquisition. Here, T= $1/f$, L = ST, and W = LN. The ADC output is 12-bit per channel. The design only sums up the data (division is to be performed during the post-processing of the data), not to lose precision. The ADC samples are summed up in 32-bit signed integers. Applying the default parameters results in ≈ 357,6 MiB of binary uncompressed data per minute per channel.

2.2.5. EXPERIMENTAL PROCEDURE

Two tests have been conducted using the developed laboratory setup. The goal of the experiments is to obtain a detailed insight into the following:

1. Pore fluid front dependence of the electrical and seismic measurements: continuous CO_2 inflows drive the pore water out of the sample pore volume resulting in a sharp decrease of the values of electrical and seismic properties (electrical conductivity, dielectric permittivity, P-wave velocity and P-wave attention) with time.

2. Pressure and temperature dependence of electrical and seismic measurements: electrical and seismic properties of a reservoir rock which is saturated with CO_2 in gaseous, liquid and supercritical phases have been investigated at numerous pressure levels starting with 1 bar up to 110 bar at constant temperature and over a temperature range from 26 to 38 $^{\circ}C$ at a constant pressure. Utilized pressure and temperature range covers critical temperatures of gas-liquid and liquid-supercritical CO_2 phase transition. The sharp alterations in density measurements may confirm the change of the CO_2 phase within the sample.

2.3. RESULTS AND DISCUSSION

2.3.1. CO_2 AND WATER INJECTION EXPERIMENTS

The goal of these experiments is to verify the sensitivity of contentious electrical and seismic measurements to the pore fluid substitution. Figure 2.5 illustrates the results of the first experiment. During this experiment, the CO_2 and demineralized water are injected. The measurements are presented here for one electrode pair and one transmission ultrasonic transducer pair which are located at the same height with respect to the injection point. The representative frequencies of the electrical conductivity, σ and relative electrical permittivity, ε_r are 800 Hz and 1 MHz, respectively.

The seismic transmission signals are recorded continuously by receiver S2 from the source S12 which are shown in Figure 2.4. The P-wave arrivals from the sandstone layer can be estimated from the recorded transmission measurements if the P-wave velocity is known. P-wave velocity of the epoxy is calculated from independent transmission measurements on an epoxy cylinder. It gives a velocity of epoxy of 2880 m/s. To estimate the P-velocities in the sandstone layer during the experiment the onset times should be picked and velocity of sandstone determined.

Figures 2.5 shows the electrical and ultrasonic measurements which are performed during this experiment. Initially, at the elapsed time between 0 and 0.3 hours, the pore space is flushed with five pore volumes of CO_2 (the pore volume is the total volume of

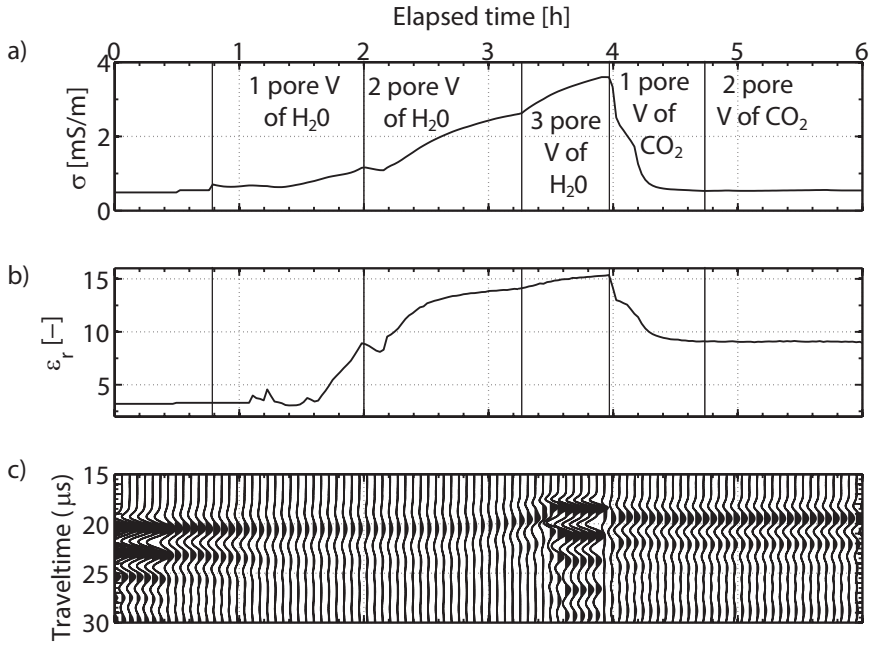

Figure 2.5: Electrical conductivity (a), relative dielectric permittivity (b) and seismic transmission (c) measurements during water and CO_2 injections into the sandstone.

very small openings in a bed of adsorbent particles). During the next 20 min the pore pressure is elevated up to 10 bar. Alterations in amplitudes of the first P-wave arrival clearly show the sensitivity of ultrasonic measurements to the pressure build up in the pore space. When the desired pressure is reached, the pore space is filled with one pore volume of demineralized water. The water injection is performed continuously with a constant flow of 1 ml/min during this stage of the experiment. The injection of one pore volume of water continues between 0.8 and 2 hours of the total time of the experiment. Figures 2.5a and b illustrate a steady elevation in the electrical conductivity and permittivity during this time period as a result of water intrusion into the domain of electric measurement geometry. The onset times of the direct transmission measurements is estimated to be 0.0184 ms and 0.0178 ms at time 1.2 and 2 hours, respectively. The length of the travelpath is defined, therefore the estimated time of the first arrival yields P-velocities of 2717 m/s and 2809 m/s at time 1.2 and 2 hours, respectively.

The injection of the second pore volume of water is done between 2 and 3.25 hours. The electrical properties are close to the equilibrium at the end of the injection. In contrast, the seismic profile shows a steady increase in the P-velocities of the saturated sandstone which reaches 2815 m/s at the end of the injection.

The third pore volume water injection is performed with a constant flow of 2 ml/min between 3.25 hours and 4 hours. Close to 4 hours both electrical and seismic equilibriums are achieved. The P-velocity of the water-saturated sandstone is 3100 m/s at the end of the water injection.

The injection of one pore volume of CO_2 into water-bearing core results in a sharp decrease in electrical properties and increase of the first arrival time in seismic measurements. The effect of the CO_2 injection can be observed around 4 hours since the start of the experiment. The profound decrease in conductivity and permittivity measurements has been observed right after the start of the CO_2 injection. This can occur due to instantaneous diffusion of the CO_2 into the system. Within 5 minutes the electrical measurements show a steady drop in the measured values till an equilibrium is reached, suggesting that the CO_2-water front reached the position of the electrode pair. The P-wave velocity has decreased to 2890 m/s due to the CO_2 injection. The injection of the second pore volume of CO_2 results in a minor change in electrical and seismic properties. The observed P-wave velocity has dropped to 2886 m/s.

2.3.2. CO_2 PHASE TRANSITION EXPERIMENT

The primary goal of the experiment is to investigate any general sensitivity of the electrical and seismic measurements to changes in pressure and temperature in a reservoir rock containing CO_2 and has a residual water saturation. Initially, the air is pumped out from the pore space of the reservoir using a vacuum pump. The rock sample is then saturated with 3 pore volumes of water. Afterwards, the CO_2 is flashed aiming to displace the water from the pore space of the reservoir. The complete displacement of water is not achieved. Therefore, the residual water saturation takes place in the pore space.

Figure 2.6 shows the measured parameters during the experiment. Pore pressure P, temperature T, density ρ, magnitude and phase of complex electrical impedance, which are later converted to electrical conductivity and permittivity σ and ε, are measured continuously. The seismic measurements are intentionally interrupted to conduct point measurements mimicking seismic reflection survey. The experiment consists of two stages: isothermal (stage 1) and isobaric (stage 2).

In stage 1, the pore pressure is gradually increased from the initial condition (P=1 bar and T=25°C) up to 111 bar pressure, keeping the temperature unchanged. During this stage, the electrical (σ and ε) and seismic signatures of the CO_2 phase transition from gaseous to liquid are continuously measured. The transition is confirmed by a density increase of the CO_2 which occurs at around 6 hours.

In stage 2, the temperature of the system is raised from 25°C up to 38°C. This stage continues till around 9,5 hours while CO_2 phase change from liquid to supercritical fluid is monitored by the electrical and seismic measurements. The confirmation of the CO_2 phase change is obtained as the CO_2 density drops around 9.6 hours. After 12 hours, the pore pressure is returned to its initial position.

Figure 2.6 illustrates the sensitivity of seismic and electrical measurements on internal pressure and temperature of the sample, as seen in the raw data of the experiments. Figure 2.6a shows the contrast between temperatures in the sample, T2 and T3, with the temperature of the injected CO_2, T1. Clearly, the time needed for establishing the temperature equilibrium in the sample is typically longer than one required for the CO_2 in the pump.

The pressures measured along injection and production end of the pressure cell, P1 and P2, are aligned in Figure 2.6b. These measurements give an indication of pore pressure. The difference of pore pressure and confining pressure, Pc, is manually controlled

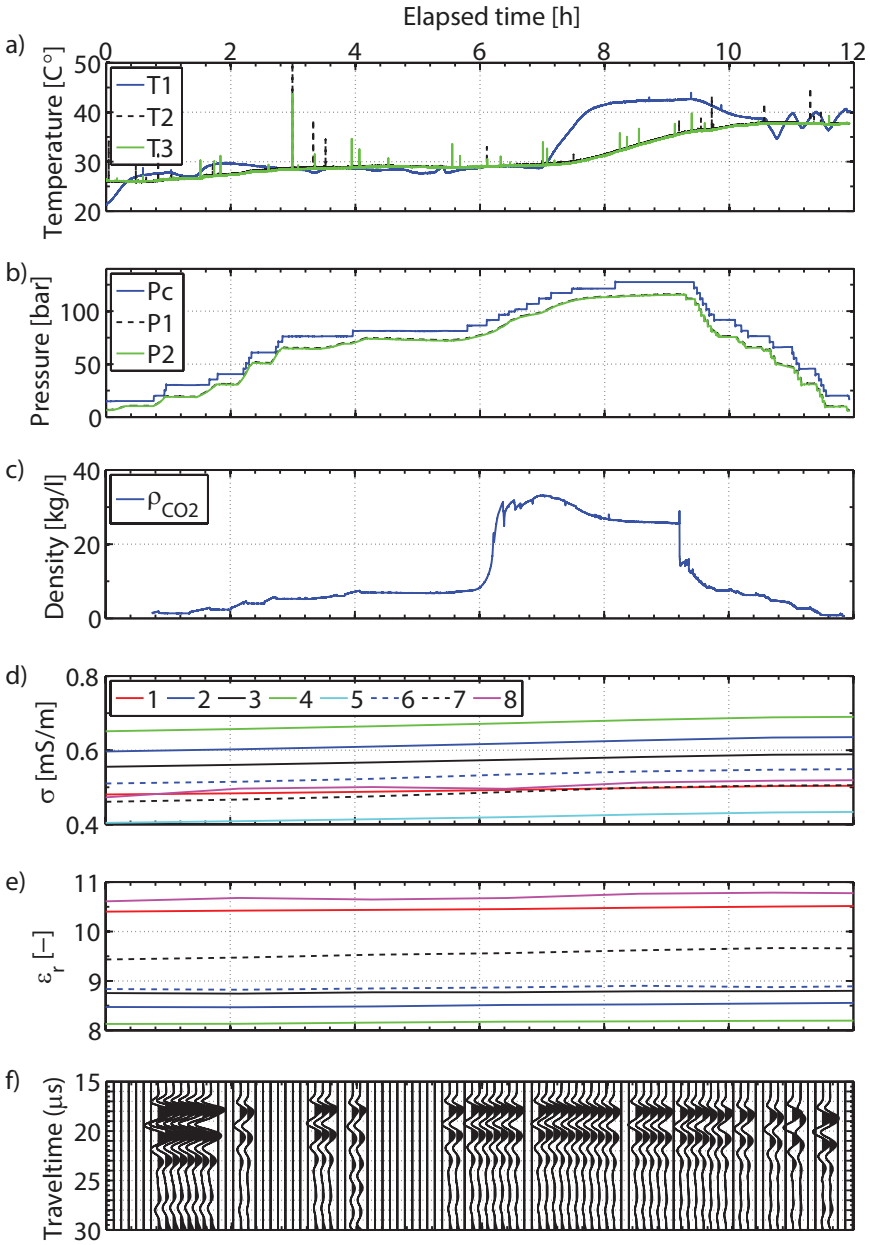

Figure 2.6: The dependence of continuous electrical and seismic measurements on pressure and temperature alterations as seen in the raw data of the experiment.

to be within the range of 5−10 bars.

Density measurements are used to confirm the CO_2 phase. A sharp jump in density

measurements indicates the CO_2 phase transition. The phase transition are indicated in Figure 2.6c.

The measured electrical conductivity, σ, is shown in Figure 2.6d. Each colour correspond to a different electrode pair, marked from 1 to 8, coupled to the lateral side of the core. The measured values of conductivity do not correspond to the heterogeneity of the porosity of the sample resulting in different residual water saturation. At the same time, the measurements exhibit quite similar trends: the conductivity increases with temperature.

Figure 2.6e shows the relative permittivity, ε_r, that exhibits the same temperature dependence as σ. The measurements from electrodes 1 and 8, however, differ from the rest. These values of measured ε_r can be influenced by the edge effect since electrode pairs 1 and 8 are positioned in the close proximity of the edge of the core.

In this experiment, ε_r shows no sensitivity to the CO_2 phase transition from gaseous to liquid and then to the supercritical state. This observation is in contrast with the measurements conducted earlier by Kirichek et al. [2013], ε_r, where a two-phase system, i.e. CO_2-bearing reservoir rock, was employed. Hence, the presence of residual water in the pores space makes the changes in ε_r due to CO_2 phase transition undetectable.

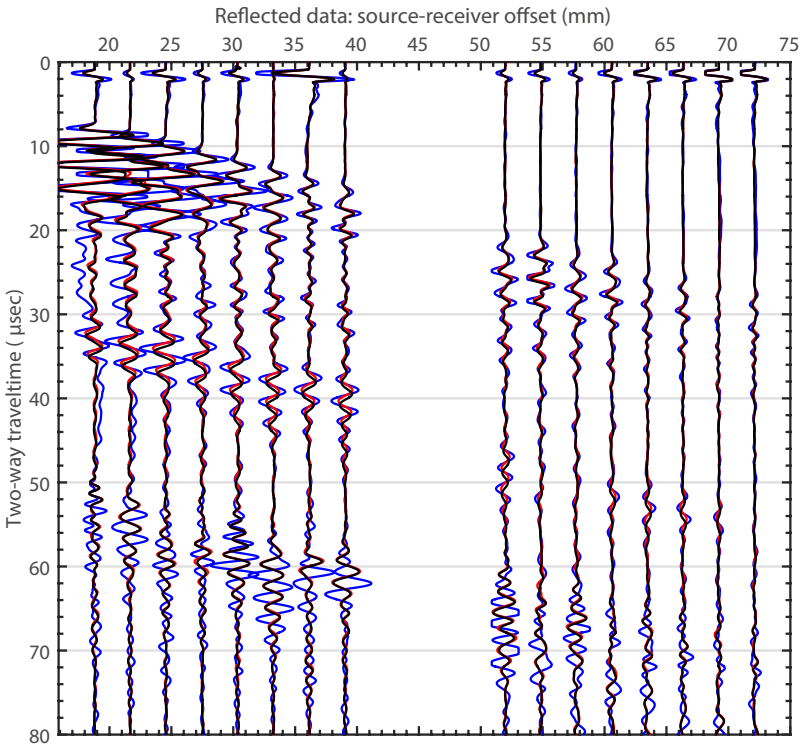

Figure 2.7: Seismic reflection supergather obtained from the concatenation of common-source gathers from sources S1 and S2 generating signals with center frequency 700 kHz. The color represents the following: blue: 10 bar, 25°C; red: 68 bar, 27°C; black: 110 bar, 35°C

Seismic transmission and reflection measurements are conducted during the experiment. Figure 2.6f shows the recorded transmissions at receiver S2 from the source S12. As the dimensions of the sample are known, the seismic velocity inside the sandstone layer can be estimated from the recorded transmission measurements if the seismic velocity inside the epoxy layer is known. Using independent transmission measurements only on an epoxy cylinder, the propagation velocity inside the epoxy is estimated as 2880 m/s. To estimate the propagation velocities during the experiment the onset times should be picked. The picking is not a trivial task as there are interfering signals. Therefore, onset times of the direct transmission for both experiments and all frequencies are defined as 0.016 ms and 0.017 ms, which translates to a velocity of between 3310 m/s and 2980 m/s, respectively. A cross-correlation method can be used in case only very small changes in velocity are detected.

Some parts of the transmission data are missing because continuous measurements have to be interrupted in order to acquire reflection measurements which are shown in Figure 2.7. This supergather is constructed by concatenating the common-source reflection gathers recorded by the receivers S3 to S10 from the source S1 and S2. Using source-receiver reciprocity, this is equivalent to having receivers at S1 and S2 and sources at S3 to S10. The reflection experiments are performed using a source signal with center frequency of 700 kHz and when CO_2 in pore spaces correspond to gaseous (P=10 bar, T=25°C), liquid (P=68 bar, T=27°C) and supercritical fluid (P=110 bar, T=35°C) phases.

2.4. CONCLUSIONS

A new laboratory setup for simultaneous electrical and seismic monitoring of the processes occurring in reservoir rock is developed. Various fluid injection scenarios show that the setup can be used for CO_2 storage monitoring purposes. The presence of CO_2 in the pore space gives the contrast in bulk electrical and seismic properties. The observed sensitivity indicates potential for a quantitative prediction of the pore contents, influence of pressure, temperature and salinity of the pore water. Finally, the electric conductivity and dielectric permittivity measurements show minor alterations due to the change of the CO_2 phase from gaseous to liquid and finally to supercritical fluid. Theses observed changes are more due to increase of temperature in the reservoir rock.

2.5. APPENDIX

The schema of the 2-layered sample placed into pressure cell is shown in Figure 2.8.

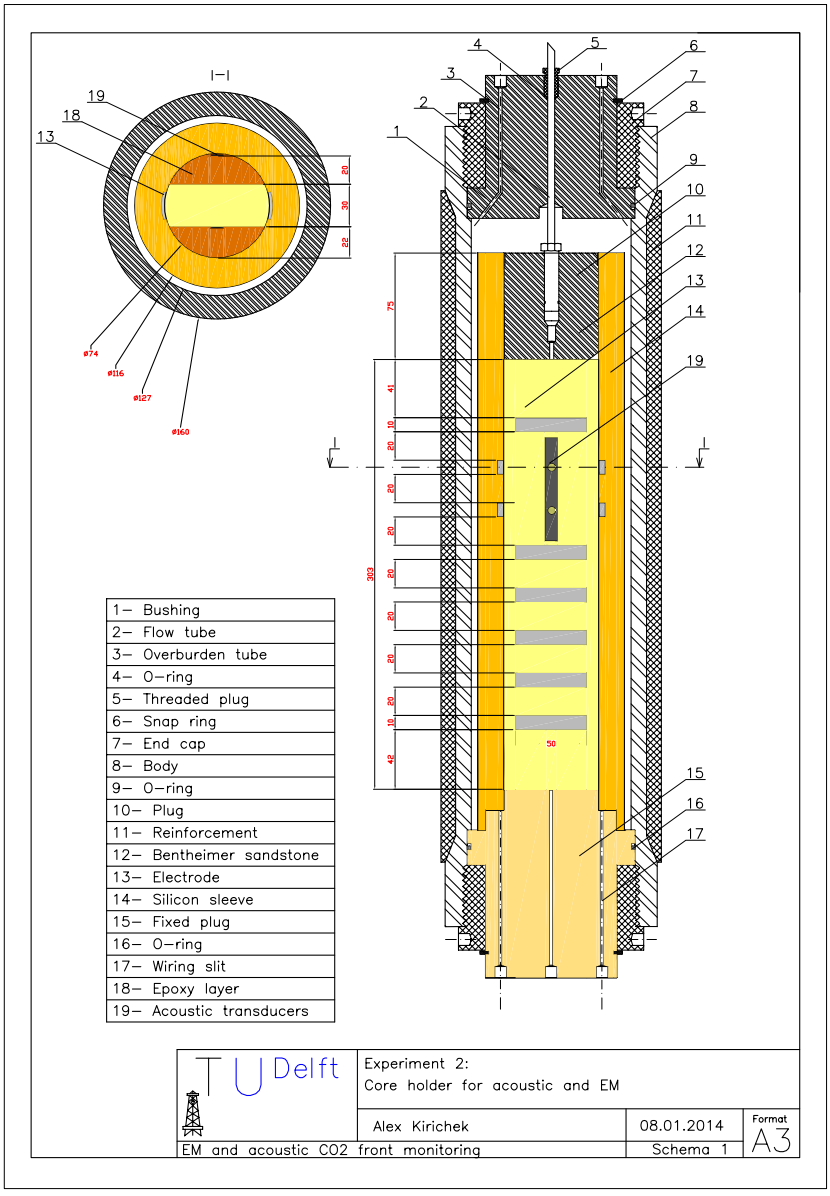

Figure 2.8: Detailed schema of the 2-layered sample within pressure cell

The details of the setup are shown in Figure 2.9.

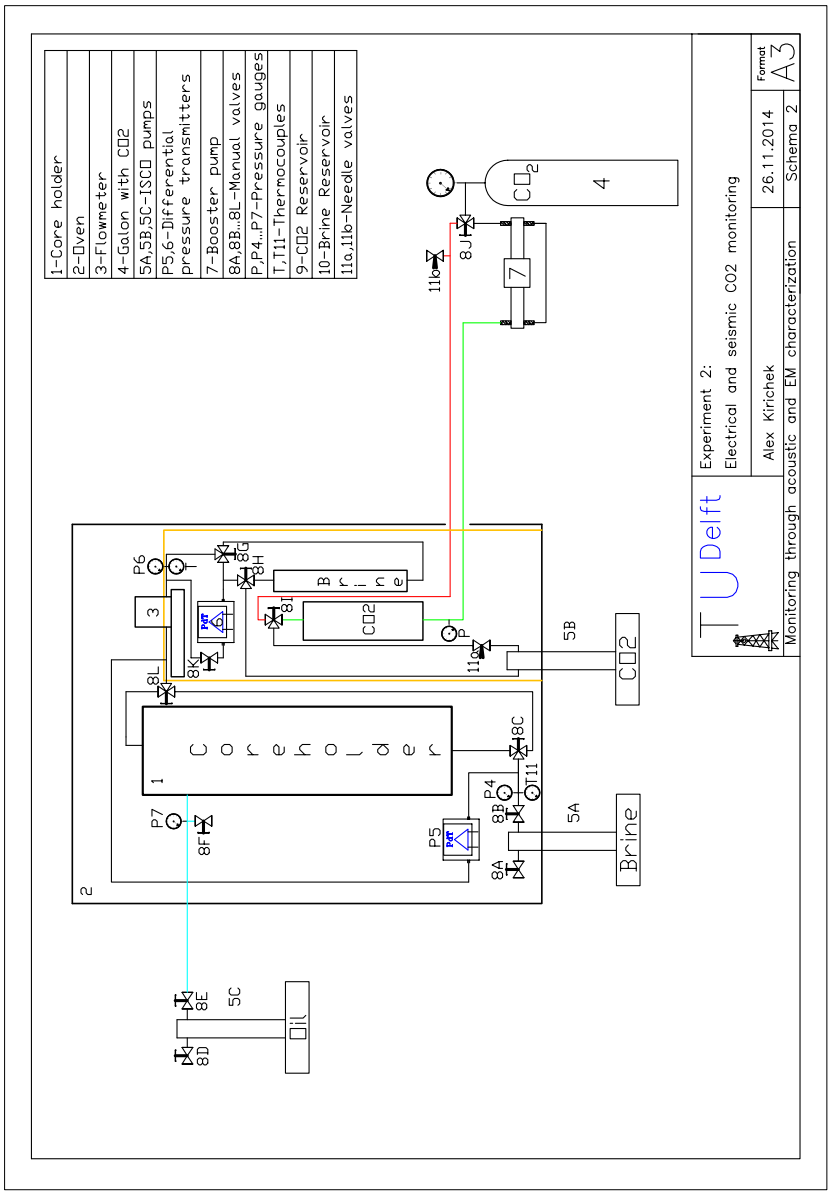

Figure 2.9: Detailed schema of the complete setup

3

NEW ELECTROKINETIC MODELS FOR THE COMPLEX ELECTRICAL CONDUCTIVITY OF POROUS MEDIA

The greatest obstacle to discovery is not ignorance -
it is the illusion of knowledge.

Daniel J. Boorstin

The low-frequency dielectric spectroscopy of porous media, where the porosity is representative for sands and sandstones, is until now always modeled using theories based on the work of Schwartz. The theory for the low-frequency dielectric spectroscopy of suspensions, on the other hand, has been developed much further over the last decades both numerically and analytically.

In this chapter, new analytical expressions for the complex conductivity of granular material, such as sands and sandstones in an electrolyte solution, are presented. These expressions have been derived using the theories developed for suspensions. It is shown that the new expressions enable to predict the measured complex conductivity of various granular material, such as packed glass beads, sands and sandstones. Because of the typical grain size of sand and sandstone particles, for any ionic strength the double layer is much thinner that the particle size. Contrary to existing theories for granular materials, the expressions we derived are valid for any ionic strength and no adjustable parameters are required.

The grains are represented by monodispersed charged spheres. It is also discussed how the expressions can be adapted in the case the particles are not spherical and the grains

Parts of this chapter have been published in Colloids and Surfaces A: Physicochemical and Engineering Aspects, 533 (2017) Kirichek et al. [2017].

are polydisperse. The derived models can be applied to a CO_2 storage reservoir rock. The considered frequency range is 0 – 10 MHz.

3.1. INTRODUCTION

DC and AC conductivity measurements are usually performed to predict the reservoir properties of granular materials and porous rocks. Most of the studies are quantitative and given as changes in conductivity in space and time. Archie's law [Archie, 1942] is typically used to derive the porosity and saturation from DC measurements. Heterogeneous pore structures in different granular materials and rocks require different geometric models for specific classes. In the case of AC conductivity measurements, the typical relaxation frequencies are usually obtained by using Cole-Cole type of models [Lesmes and Frye, 2001]. These frequencies are then linked to rock and granular material properties, e.g. porosity and grain [Revil et al., 2012, Sen et al., 1981].

In the present chapter, porous media consisting of grains and electrolyte are considered. Typically, compacted and uncompacted sands, sandstones are representative for the porous material which is normally located in CO_2 storage reservoirs and estuarine regions. Percolation thresholds are not considered, nor is pore clogging. This implies that the models which will be discussed are valid for porous media in which each grain has nearly all of its surface in contact with the electrolyte. This does not mean that the distance between particles should be large, as discuss in a forthcoming section.

Because the typical size of the grains is of the order of microns, it can be estimated that one of the relaxation frequencies associated to the ionic diffusion on the lengthscale of a grain is of the order of $f_a \equiv D/\left(2\pi a^2\right) \simeq$ [1-300 Hz], where $D \simeq 2 \cdot 10^{-9}$ m^2/s is taken as the typical diffusion coefficient of an ion and $a \simeq \left[10\ \mu\text{m} - 1\ \mu\text{m}\right]$ the typical radius of a grain. This relaxation is called α relaxation by some authors [e.g., Grosse and Delgado, 1984, Revil, 2013]. Another relaxation exists, usually at higher frequency (depending on ionic strength and grain size), associated to the ionic diffusion at the lengthscale of the electric double layer around each of the grains. The corresponding relaxation, called Maxwell-Wagner-O'Konski relaxation, is also referred to as δ or β relaxation by the same authors. The Maxwell-Wagner-O'Konski relaxation frequency is defined by $f_0 \equiv D\kappa^2/(2\pi)$ where κ^{-1} represents the double layer thickness. This thickness is estimated to be in the range $f_0 \simeq$ [0.1-10 MHz] for monovalent salt concentrations between 0.1 and 10 mM. A third relaxation frequency can be associated with the polarization of water molecules. The associated relaxation frequency is termed γ relaxation [e.g., Grosse and Delgado, 1984, Revil, 2013] and leads to a strong decrease of the water dielectric permittivity in the GHz range. In the present chapter this relaxation is not studied as the frequency range considered is $0 - 10$ MHz.

Models that are more elaborate than the Cole-Cole model enable to give additional information about the grain properties, such as the grain's surface charge. The surface charge of grains is an important property of the granular material as it can, for instance, be used to predict the variation of conductivity upon a pH change due to chemical reactions, or be linked to the retention and transport of contaminants and nutrients within the porous media. Current models in geophysics for granular type of porous media are based on the work of Schwartz [Schwarz, 1962], who was one of the pioneers, along with O' Konski [O'Konski, 1955, 1960] in setting-up the first models for the dielectric response of a colloidal particle in an applied electric field. In colloid science, their models have been extended by, among others, Fixman [Fixman, 1980, 1983], Hinch [Hinch et al., 1984], O' Brien [O'Brien, 1982, 1986]. In 1981, DeLacey and White presented a

full numerical model for the dielectric response of a charged sphere at any electrolyte concentration, electric field frequency [DeLacey and White, 1981]. In 2008, an analytical model was presented that reproduced this full numerical solution within a few percent inaccuracy [Chassagne and Bedeaux, 2008].

In the first section, we will show how the analytical model for the polarization of a charged grain presented in Chassagne and Bedeaux [2008] can be incorporated in the Maxwell-Wagner and Bruggeman expressions for the conductivity of a porous system like a CO_2 storage reservoir. These expressions can be found for example in Sen et al. [1981]. The models will be compared with other existing models and available measurement data in the second section. Finally, it is discussed how these expressions can be adapted in the case the particles are not spherical and the grains are polydisperse.

3.2. THE COMPLEX CONDUCTIVITY OF POROUS MEDIA

In this section, new relations for the conductivity of a porous medium consisting of compacted, immobile, charged spheres are derived. As illustrated in Figure 3.1, we make the assumption that the spherical particles have most of their surface in contact with the electrolyte. We, therefore, do not consider percolation thresholds nor clogging of the interstitial cavities. The general relations between the different permittivities of the system

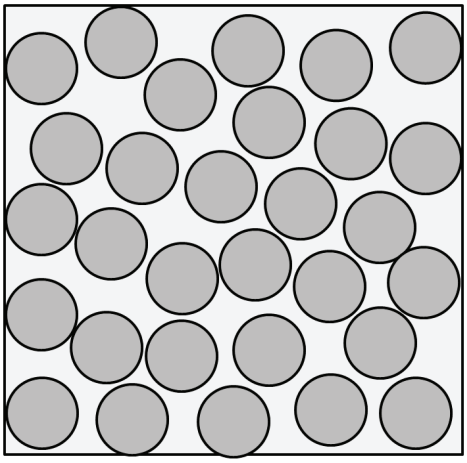

Figure 3.1: The porous media is seen as packed, immobile spheres in an electrolyte.

from first principles are derived [Reynolds and Hough, 1957]. In this work ε_i^* stands for the complex dielectric permittivity of substance i. The relationship between the complex electrical conductivity σ^* and ε^* is given by:

$$\varepsilon^* \equiv \frac{\sigma^*}{i\omega\varepsilon_0}, \tag{3.1}$$

with

$$\sigma^* = \sigma + i\omega\varepsilon_0\varepsilon, \tag{3.2}$$

where ε is the relative dielectric permittivity of the studied medium, ε_0 is the permittivity of vacuum and ω is the angular frequency of the applied electric field.

A two-phase system is considered. The subscripts g and e stands for grain and electrolyte, respectively. The volume fraction ϕ_s is linked to the porosity ϕ by

$$\phi_s = 1 - \phi. \tag{3.3}$$

Let the two substances have dielectric permittivities ε_g^* and ε_e^* and occupy the volume fractions ϕ_s and $(1-\phi_s)$, respectively. The electric displacement of the mixture is given by

$$\overline{D} = \frac{1}{V}\int_{V_g} D dV + \frac{1}{V}\int_{V_e} D dV = \phi_s \overline{D}_g + (1-\phi_s)\overline{D}_e, \tag{3.4}$$

where V_g and V_e are volumes of grains and electrolyte, respectively. In the same way, the average electric field $\overline{E}$ is derived by

$$\overline{E} = \phi_s \overline{E}_g + (1-\phi_s)\overline{E}_e. \tag{3.5}$$

Wiener [1912] proposed that the dielectric constant of the mixture and of each component can be written as

$$\begin{aligned} \overline{D} &= \varepsilon_m^* \overline{E}, \\ \overline{D}_g &= \varepsilon_g^* \overline{E}_g, \\ \overline{D}_e &= \varepsilon_e^* \overline{E}_e. \end{aligned} \tag{3.6}$$

From Equations 3.4 and 3.5 it follows that

$$\begin{aligned} \varepsilon_m^* &= \varepsilon_g^* \phi_s \frac{\overline{E}_g}{\overline{E}} + \varepsilon_e^* (1-\phi_s)\frac{\overline{E}_e}{\overline{E}}, \\ 1 &= \phi_s \frac{\overline{E}_g}{\overline{E}} + (1-\phi_s)\frac{\overline{E}_e}{\overline{E}}. \end{aligned} \tag{3.7}$$

Rearranging these equations leads to

$$\varepsilon_m^* = \varepsilon_e^* + \left(\varepsilon_g^* - \varepsilon_e^*\right)\phi_s \frac{\overline{E}_g}{\overline{E}} \tag{3.8}$$

and

$$\left(\varepsilon_m^* - \varepsilon_g^*\right)\phi_s \frac{\overline{E}_g}{\overline{E}} + \left(\varepsilon_m^* - \varepsilon_e^*\right)(1-\phi_s)\frac{\overline{E}_e}{\overline{E}} = 0. \tag{3.9}$$

Theoretically the two last equations are equivalent but when approximations have to be made about $\overline{E}_k/\overline{E}$, that is no longer true. Equation 3.8 is typically used for the case of particles dispersed in a continuous medium. This relationship is called Maxwell-Wagner approximation. In the literature other names are associated with this type of approximation, e.g Clausius-Mossotti, Garnett and Lorentz, Maxwell-Garnett. Hereinafter the name Maxwell-Wagner is used to avoid confusions.

Equation 3.9 is used when the particle size of the two components is of the same order of magnitude. This approximation is known as Bruggeman model. $\overline{E}_k/\overline{E}$ is derived for Maxwell-Wagner and Bruggeman models in the following subsections.

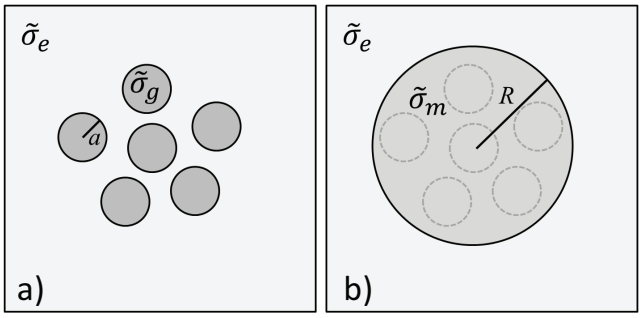

Figure 3.2: The porous media is seen as packed, immobile spheres in an electrolyte.

3.2.1. MAXWELL-WAGNER MODEL

The Maxwell-Wagner expression is briefly recalled, as this will enable us to discuss how this expression can be adapted to account for the polarization of the grains under the influence of the applied electric field. The full derivations can be found in Grosse [2002]

For a dilute suspension, the term $\overline{E}_g/\overline{E}$ in Equation 3.119 can be evaluated by assuming that the electrical conductivity around a particle is σ_e^* and, equivalently, the complex permittivity is ε_e^*. Figure 3.2a shows a system with N non-interacting spherical grains. Each grain which has a complex conductivity σ_g^* and a dipolar coefficientβ^* is embedded in a medium of complex conductivity σ_e^*. The electric potential at a given distance of the dipoles then reads

$$\Psi^* = -\mathbf{E}\cdot\mathbf{r}\left[1 - N\beta^*\left(\frac{a}{r}\right)^3\right], \tag{3.10}$$

where a is the characteristic radius of a grain with a dipolar coefficient β^*. The system consisting of N dipoles and its surrounding fluid can be also considered as an homogeneous medium of dipolar coefficient β_m^*. This scenario is depicted in Figure 3.2b. In this case, the electric potential outside this medium yields

$$\Psi_{out}^* = -\mathbf{E}\cdot\mathbf{r}\left[1 - \beta_m^*\left(\frac{R}{r}\right)^3\right], \tag{3.11}$$

where R is the characteristic length of pseudo-homogeneous medium of complex conductivity σ_m^*. Laplace can be applied to the interior of the pseudo-homogeneous medium

$$\Delta\Psi_{in}^*(r < R) = 0, \tag{3.12}$$

yielding

$$\Psi_{in}^*(r < R) = A \times \mathbf{E}\cdot\mathbf{r}, \tag{3.13}$$

where A is an integration constant. This constant can be eliminated using the following boundary conditions

$$\begin{aligned} \sigma_m^*\left(\frac{\partial\Psi_{in}^*}{\partial r}\right)_{r=R} &= \sigma_e^*\left(\frac{\partial\Psi_{out}^*}{\partial r}\right)_{r=R}, \\ \Psi_{in}^*(R) &= \Psi_{out}^*(R), \end{aligned} \tag{3.14}$$

which yield

$$\beta_m^* = \frac{\sigma_m^* - \sigma_e^*}{\sigma_m^* + 2\sigma_e^*}. \tag{3.15}$$

Equating Equation 3.10 and Equation 3.11 leads to

$$\beta_m^* = \beta^* \frac{Na^3}{R^3} = \beta^* \phi_s, \tag{3.16}$$

where ϕ_s is the volume fraction associated to the N particles. From the previous equation it can be deduced that

$$\sigma_m^* = \sigma_e^*(\omega) \frac{1 + 2\phi_s \beta^*}{1 - \phi_s \beta^*}. \tag{3.17}$$

In order to obtain the traditional Maxwell–Wagner relation, it is necessary to assume that

$$\beta^* = \frac{\sigma_g^* - \sigma_e^*}{\sigma_g^* + 2\sigma_e^*}. \tag{3.18}$$

The combination of Equations 3.17 and 3.18 leads to

$$\frac{\sigma_m^* - \sigma_e^*}{\sigma_m^* + 2\sigma_e^*} = \phi_s \frac{\sigma_g^* - \sigma_e^*}{\sigma_g^* + 2\sigma_e^*}. \tag{3.19}$$

This relation is given in terms of ε^* as Equation 6 in Sen et al. [1981]. As stated by Sen et al. under their Equation 6, the Maxwell-Wagner expression is also known as the Clausius-Mossotti or Maxwell-Garnett relation. In most experimental studies, the core material of a colloidal particle can be considered as purely dielectric (non-conducting). This is the case for most silica-based particles for example. The medium can then be seen as an electrolyte solution in which there are the dielectric holes. Equation 3.19 leads to, assuming σ_g =0:

$$\begin{aligned} \sigma_m &= \sigma_e \frac{2(1-\phi_s)}{2+\phi_s}, \\ \sigma_m &= \sigma_e \quad \text{for} \quad \phi_s << 1. \end{aligned} \tag{3.20}$$

For low volume fractions, the medium conductivity is in good approximation equal to the conductivity of the electrolyte.

Alternatively, it is possible to consider the system as N spheres of complex conductivity σ_e^* embedded in an medium of complex conductivity σ_g^*. The porous media in this case is an insulating medium in which there are pockets of electrolyte. One then gets:

$$\frac{\sigma_m^* - \sigma_g^*}{\sigma_m^* + 2\sigma_g^*} = (1-\phi_s) \frac{\sigma_e^* - \sigma_g^*}{\sigma_e^* + 2\sigma_g^*}, \tag{3.21}$$

which, assuming $\sigma_e >> \sigma_g$, leads to

$$\sigma_m = \sigma_g \frac{1 + 2(1-\phi_s)}{1 - (1-\phi_s)}, \tag{3.22}$$

$$\sigma_m = 0 \quad \text{for} \quad \sigma_g = 0. \tag{3.23}$$

This last relation implies that the matrix of grains, which can be seen as a porous media with pockets of water, is not conducting.

In the case of sands and sandstones, one would be tempted to prefer Equation 3.21 over Equation 3.19, as intuitively there is more volume occupied by the grains than by the water. However, the restrictions imposed on Equation 3.19 do not depend on the volumetric ratio between grains and water. The two major hypotheses made to derive Equation 3.19 are: (a) the grains are surrounded by electrolyte (this does not mean that the volume of electrolyte should be more important than the volume of grains) and (b) the interaction between grains are neglected. As discussed by Sen et al. [1981], the pore space remains connected in the first order of approximation in most experimental studies, with the grains touching each other only at or on small, isolated regions of contact (see p.784/785 in Sen et al. [1981]). This implies that the fluid phase remains continuous to very low values of the porosity (very high values of the volume fraction) and this validates hypothesis (a). As for hypothesis (b), the major consequence of dipole-dipole interaction is usually that the dipoles tend to re-orient in the electric field, bringing particles in contact along the electric field lines. This movement is not possible in sand, as the particles are too large and too compacted to move. Multiple effects can most probably be neglected as well in first approximation and, therefore, hypothesis (b) should be quite measurable. Hypotheses (a) and (b) enable to approximate the porous medium as a concentrated suspension of (spherical) grains which are immobile. Each grain is assumed to have the same dipolar coefficient as it would have without the presence of its neighbors.

In Chassagne and Bedeaux [2008] an analytical expression is given for the dipolar coefficient of a spherical charged particle in an electrolyte, which reproduces within a few percent the dipolar coefficient found by solving numerically the full set of electrokinetic equations as presented in DeLacey and White [1981]. The expression is valid for the whole range of particle's charge, ionic strength and applied field frequency. A restriction for this expression is that it has been derived assuming there is no interaction between particles. This means in particular that a limiting case is when the electrolyte concentration is so low that the grains' double layers start to overlap significantly. In DeLacey and White [1981], Chassagne and Bedeaux [2008] the colloidal particle could have an electrophoretic mobility. As stated above, in the present case, the particles are immobile. This implies that the electrophoretic term (defined as $\tilde{K}_U$ in Chassagne and Bedeaux [2008]) is set equal to zero in the expression of β given by Equation 64 in Chassagne and Bedeaux [2008]. Adapting Equation 64 for the case of a non-moving sphere with a double layer thickness that is smaller than the particle size (a valid assumption for micrometric particles in nearly all experimental conditions) leads to Equation 49 in Chassagne and Bedeaux [2008] which is given by (adapting the notations to the ones used in the present article):

$$\beta^* = \frac{\sigma_g^* - \sigma_e^* + \sigma_{//}^* + \sigma_\perp^*}{\sigma_g^* + 2\sigma_e^* + \sigma_{//}^* - 2\sigma_\perp^*}, \tag{3.24}$$

where $\sigma_{//}^*$ and $\sigma_\perp^*$ accounts for the conductivities parallel and perpendicular to the grain's surface that arises from the polarization of the double layer. The derivation of the surface charge density is given in Appendix A. The Stern layer contribution can be also consid-

ered as shown in Appendix B. In case there is no Stern layer, $\sigma^*_{//}$ and $\sigma^*_{\perp}$ are given by

$$\begin{aligned} \sigma^*_{//} &= \sigma_{//} = 2\frac{\sigma_e}{\kappa a}\left[\exp\left(\frac{e|\zeta|}{2kT}\right)-1\right], \\ \sigma^*_{\perp} &= -\frac{J_1}{J_2}\sigma_{//}, \end{aligned} \tag{3.25}$$

where ζ is the zeta potential of the particle, k is the Boltzmann constant and T the temperature. The relation between zeta potential and surface charge density is discussed in Appendix A. The Debye layer thickness κ^{-1} is given by

$$\kappa^{-1} = \sqrt{\frac{\epsilon_0 \epsilon_e D}{\sigma_e}}. \tag{3.26}$$

Furthermore

$$\begin{aligned} J_1 &= 1+\lambda_n a, \\ J_2 &= 1+(1+\lambda_n a)^2, \\ \lambda_n^2 &= \frac{i\omega}{D}, \end{aligned} \tag{3.27}$$

where D is the typical ionic diffusion coefficient. For simplicity, we here only consider a symmetric monovalent electrolyte of valence 1 and assume that the diffusion coefficients of the cation and the anion are equal. More general expressions can be found in Chassagne and Bedeaux [2008]. One generally defines

$$Du = \frac{\sigma_{//}}{\sigma_e} = \frac{2}{\kappa a}\left[exp\left(\frac{e|\zeta|}{2kT}\right)-1\right]. \tag{3.28}$$

The factor Du is the so-called "Dukhin number" which expresses the ratio between the parallel surface conductivity due to the ions in the double layer and the bulk conductivity. This ratio was first given by Bikerman in 1940 Bikerman [1940], but given the name of Dukhin who made significant progress in the work of particle polarization in electric fields in the 1970-80's Dukhin [1974].

A similar expression for Du is given by Equation 37 in Lyklema and Minor [1998]. This expression is also valid for non-monovalent salts and this leads to the inclusion of valences z_k in their expression ($z_1 = -z_2 = 1$ is used here). Finally, the terms involving m_2 and Θ_2 are corrections for the ionic velocity in the neighborhood of the particle and the contribution of the conduction of the ions in the Stern layer respectively. From Equations 3.24 – 3.28, one can get

$$\beta^* = \frac{\sigma^*_g - \sigma^*_e + \sigma_{//}(1-J_1/J_2)}{\sigma^*_g + 2\sigma^*_e + \sigma_{//}(1+2J_1/J_2)}. \tag{3.29}$$

The combination of Equations 3.17 and 3.29 provides a new relation for the Maxwell-Wagner expression for charged spheres:

$$\sigma^*_m = \sigma^*_e \frac{\left[\sigma^*_g + 2\sigma^*_e + \sigma_{//}(1+2J_1/J_2)\right] + 2\phi_s\left[\sigma^*_g - \sigma^*_e + \sigma_{//}(1-J_1/J_2)\right]}{\left[\sigma^*_g + 2\sigma^*_e + \sigma_{//}(1+2J_1/J_2)\right] - \phi_s\left[\sigma^*_g - \sigma^*_e + \sigma_{//}(1-J_1/J_2)\right]}. \tag{3.30}$$

DC ELECTRIC FIELDS

In laboratory and field experiments, DC electric fields are traditionally used, primarily to avoid crosstalks and electromagnetic interferences within the equipment and wiring. In that case, one gets $J_1/J_2 = 1/2$. As $\sigma_g = 0$, it leads to

$$\beta^*(\omega) = \frac{-1 + Du/2}{2 + 2Du}. \tag{3.31}$$

Assuming that Du is small (which is a reasonable assumption when κa is quite large), one gets

$$\beta^*(\omega) \simeq \frac{-1}{2}\left(1 - \frac{3}{2}Du\right). \tag{3.32}$$

Substituting this result into Equation 3.17 leads to

$$\sigma_m = \sigma_e \frac{1 - \phi_s(1 - 3Du/2)}{1 + \phi_s(1 - 3Du/2)/2}, \tag{3.33}$$

which is the conductivity of a sandstone consisting of charged spheres in an electrolyte. One can verify that for $\sigma_{//} = 0$, i.e. uncharged spheres, one recovers the traditional Maxwell-Wagner expression, Equation 3.19. To obtain porosity, the porous medium conductivity σ_m is usually fitted as function of the electrolyte conductivity σ_e according to Archie's law Archie [1942] that reads

$$\sigma_m = \phi^m \sigma_e, \tag{3.34}$$

where m is an empirical coefficient, often called the cementation exponent (or index) Sen et al. [1981], found by fitting the data. Making the equivalence between Equation 3.33 and Equation 3.34 gives the following theoretical expression for m:

$$m \equiv ln\left[\frac{1 - (1-\phi)(1 - 3Du/2)}{1 + (1-\phi)(1 - 3Du/2)/2}\right] / ln[\phi]. \tag{3.35}$$

3.2.2. BRUGGEMAN MODEL

The Bruggeman model is an alternative to the Maxwell-Wagner model given above. In order to derive the Bruggeman expression, one traditionally makes use of the Maxwell-Wagner relation Equation 3.19. The derivation is based on the evaluation of the mean medium conductivity σ_{m+1} of a two-component mixture at a step $m+1$ as function of the conductivity σ_m at step m (Note that the subscript m should not be confused with Archie's cementation exponent m). Between step m and $m+1$, a small amount of one component is added to the mixture and therefore the mean conductivity of the medium will slightly change between the steps. A derivation can be found in Sen et al. [1981]. Instead of using Equation 3.19, Equation 3.17 is used to find a more general expression for the Bruggeman equation.

Let us assume that at step $m = 1$ the medium is composed of only electrolyte, thus $\sigma^*_{m=1} = \sigma^*_e$. The initial volume occupied by the electrolyte is V. At each next step m, a small volume dv_m of spheres and a small volume dv_e of electrolyte is added to the medium. Rewriting Equation 3.17 one finds that

$$\frac{\sigma^*_{m+1} - \sigma^*_m}{\sigma^*_{m+1} + 2\sigma^*_m} = \phi_{m+1}\beta^*_m, \tag{3.36}$$

where the grain volume fraction at step $m+1$ is defined by the ratio between the volume of spheres added and the total volume (this definition stems from the derivations given in Equations 3.10 – 3.16) :

$$\phi_{m+1} = \frac{dv_m}{V_m + v_m}. \tag{3.37}$$

The total volume $V_m + v_m$ is the sum of the volume of electrolyte V_m and the volume v_m of grains at step m.

The volume of spheres added is given by

$$dv_m = a^3 dN, \tag{3.38}$$

where dN represents the number of spheres added at the step $m+1$. By definition the volume fraction of the spheres is given by

$$\phi_s = \frac{v_m}{V_m + v_m} \tag{3.39}$$

and, thus,

$$d\phi_s = \frac{V_m}{(V_m + v_m)^2} dv_m = (1-\phi_s)\frac{dv_m}{V_m + v_m} = (1-\phi_s)\phi_{m+1}. \tag{3.40}$$

From Equations 3.36, 3.40, using the fact that $\sigma^*_{m+1} \simeq \sigma^*_m$ and $\sigma^*_{m+1} - \sigma^*_m \equiv d\sigma^*_m$ one gets:

$$\frac{d\sigma^*_m}{3\sigma^*_m} = \frac{d\phi_s}{1-\phi_s}\beta^*_m, \tag{3.41}$$

The dipolar coefficient β_m of a sphere at step m is found from adapting Equation 3.29 leading to

$$\beta^*_m = \frac{\sigma^*_g - \sigma^*_m + \sigma_{//}(1 - J_1/J_2)}{\sigma^*_g + 2\sigma^*_m + \sigma_{//}(1 + 2J_1/J_2)}. \tag{3.42}$$

Combining Equations 3.41 and 3.42, one can set-up the integral:

$$\int_{\sigma^*_e}^{\sigma^*_m} \frac{\sigma^*_g + 2\sigma^* + \sigma_{//}(1 + 2J_1/J_2)}{\sigma^*_g - \sigma^* + \sigma_{//}(1 - J_1/J_2)} \frac{d\sigma^*}{3\sigma^*} = \int_0^{1-\phi} \frac{d\phi_s}{1-\phi_s}. \tag{3.43}$$

This integration yields a new Bruggeman-type of relation:

$$\left(\frac{\sigma^*_e}{\sigma^*_m}\right)^{\alpha} \left(\frac{\sigma^*_m - \sigma^*_g - \sigma_{//}(1 - J_1/J_2)}{\sigma^*_e - \sigma^*_g - \sigma_{//}(1 - J_1/J_2)}\right)^{\gamma} = \phi, \tag{3.44}$$

with

$$\begin{aligned} \alpha &= \frac{\sigma^*_g + \sigma_{//}(1 + 2J_1/J_2)}{3\left(\sigma^*_g + \sigma_{//}(1 - J_1/J_2)\right)}, \\ \gamma &= \frac{\sigma^*_g + \sigma_{//}}{\sigma^*_g + \sigma_{//}(1 - J_1/J_2)}. \end{aligned} \tag{3.45}$$

In the limit of uncharged grains $\sigma_{//} = 0$ Equation 3.44 reduces to

$$\left(\frac{\sigma_e^*}{\sigma_m^*}\right)^{1/3} \frac{\sigma_g^* - \sigma_m^*}{\sigma_g^* - \sigma_e^*} = \phi, \tag{3.46}$$

which is usually referred to as the Hanai-Bruggeman-Sen formula and is equivalent to Equation 21 in Sen et al. [1981].

DC ELECTRIC FIELDS

In the DC limit one gets $\sigma_g = 0$ and $J_1/J_2 = 1/2$, leading to

$$\left(\frac{\sigma_e}{\sigma_m}\right)^{4/3} \left(\frac{\sigma_m/\sigma_e - Du/2}{1 - Du/2}\right)^2 = \phi. \tag{3.47}$$

At high ionic strengths, one expects that $Du \to 0$ and

$$\sigma_m = \sigma_e \phi^{3/2} < \sigma_e, \tag{3.48}$$

which is the limit for uncharged spheres, see Sen et al. [1981]. By analogy with Archie's law Equation 3.34, the cementation exponent is $m = 3/2$.

THE SHELL MODEL

The same mathematical derivations as given in Equations 3.10 – 3.17 can be applied to evaluate the mean complex conductivity of a charged sphere surrounded by an electric double layer. The model then obtained is called the shell model Chassagne et al. [2003]. A sketch is given in Figure 3.3.

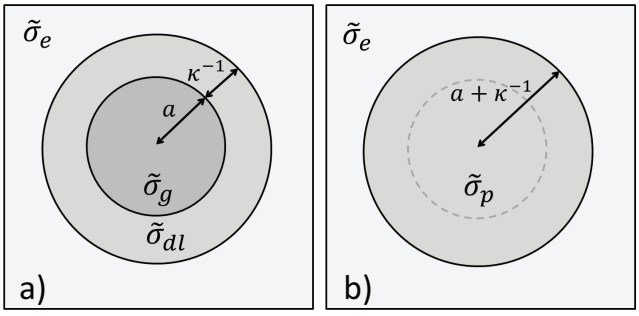

Figure 3.3: a) Sphere with radius a of complex conductivity σ_g with a double layer of complex conductivity σ_{dl} in an electrolyte solution of complex conductivity σ_e. b) Equivalent sphere of radius $a + \kappa^{-1}$ of complex conductivity σ_p in an electrolyte solution of complex conductivity σ_e.

Following the same lines of derivations as above, one can show that

$$\frac{\sigma_p^* - \sigma_{dl}^*}{\sigma_p^* + 2\sigma_{dl}^*} = \phi_{dl} \frac{\sigma_g^* - \sigma_{dl}^*}{\sigma_g^* + 2\sigma_{dl}^*}, \tag{3.49}$$

where σ_{dl}^* is the complex conductivity associated to the double layer, σ_p^* is the complex equivalent conductivity of the system consisting of the grain and its double layer (p

stands for "particle" in the broad sense) and ϕ_{dl} is the volume fraction associated to the double layer of thickness κ^{-1}. Hence

$$\phi_{dl} = \frac{a^3}{\left(a+\kappa^{-1}\right)^3} = \frac{1}{(1+1/(\kappa a))^3} \simeq 1 - \frac{3}{\kappa a}. \tag{3.50}$$

Subsequently the dipolar coefficient of the particle (grain and double layer) can be evaluated from

$$\beta^* = \frac{\sigma_p^* - \sigma_e^*}{\sigma_p^* + 2\sigma_e^*}. \tag{3.51}$$

The analogy between Equations 3.29 and 3.51 was already pointed out in Chassagne et al. [2003]. Note that the shell model does not account for the distortion of the double layer (or any other layer) under the influence of the electric field, but only its polarization. This implies that the shell model is only valid for large κa. Additional layers can similarly be added, accounting for example for a Stern layer complex conductivity. This is discussed in Appendix B.

MODEL OF SEN ET AL. [1981]

Sen et al. [1981] introduce the model of a self-similar rock. This model is based on the traditional Bruggeman expression Equation 3.46. In their model, at each step $m+1$ a small volume dv_m is added to the mixture. Like in the derivation presented above, they assume that $\sigma^*_{m=1} = \sigma_e^*$ and the volume of electrolyte is given by V at step $m = 1$. In the model of Sen et al. [1981], the expression for ϕ_{m+1}, which can be compared to Equation 3.37, is given by

$$\phi_{m+1} = \frac{dv_m}{V + v_m}. \tag{3.52}$$

The authors consider a two component mixture: one component is the electrolyte, the other is composed of electrolyte and grains, and it is this second component that is added at each step m. In their model, the volume of the first component (electrolyte) is therefore not changing and $V_m = V$. Note that the fact that V_m does not vary at each step m does not change the derivations given in Equations 3.40 – 3.46. In Sen et al. [1981] model, the component made of electrolyte and grains is seen as a continuum and has therefore the same properties at any scale. This enables them to set-up their self-similar rock model, as depicted in Figure 1 in Sen et al. [1981].

The fact that the component made of electrolyte and grains has the same properties at any particle's radius (for a given volume fraction) is only valid in the case that the dipolar coefficient of the particles do not depend on their size. This is strictly true for uncharged spheres. In that case Equation 3.29 and Equation 3.51 reduce to:

$$\beta^* = \frac{\sigma_g^* - \sigma_e^*}{\sigma_g^* + 2\sigma_e^*}. \tag{3.53}$$

which is indeed radius-independent. For charged spheres, the self-similar model is in principle not valid. In fact, for particles with different sizes but having the same surface density, we will see in the third section that the main contribution to the complex conductivity of the granular medium arises from the smallest particles if they are present in a reasonable amount.

3.2.3. COMPARISON BETWEEN MODELS FOR CHARGED GRAINS

In this subsection the newly derived expressions for the Maxwell-Wagner and Bruggeman expressions (Equations 3.30 and 3.44, respectively) are compared to other existing models.

A GENERAL MODEL

A common expression for σ_m^* of granular material is given by [e.g., Börner et al., 2016, Vinegar and Waxman, 1984]:

$$\sigma_m^* = \sigma + \sigma_{surf}^* + \sigma_{hf}^*, \tag{3.54}$$

where σ_{hf} is associated to "high-frequency effects", σ_{surf} to "surface conduction effects" and σ is defined by the standard Archie's law:

$$\sigma = \phi^m \sigma_e. \tag{3.55}$$

Note, in this case we have $\sigma_m = Re(\sigma_m) \neq \sigma$. This expression can be compared to the one we obtained for the Maxwell-Wagner expression for charged spheres. We rewrite the dipolar coefficient given in Equation 3.29:

$$\begin{aligned} \beta^* &= \frac{-1}{2} + x, \\ x &= \frac{3\left(\sigma_g^* + \sigma_{//}\right)}{2\left[\sigma_g^* + 2\sigma_e^* + \sigma_{//}\left(1 + 2J_1/J_2\right)\right]}. \end{aligned} \tag{3.56}$$

The complex conductivity of the granular medium can then be rewritten from Equation 3.17

$$\sigma_m^* = \frac{1-\phi_s}{1+\phi_s/2}\sigma_e^* + \frac{3\phi_s x \sigma_e^*}{1+\phi_s(1-x)+\phi_s^2(1/2-x/2}, \tag{3.57}$$

which leads to

$$\sigma_m^* = \frac{1-\phi_s}{1+\phi_s/2}\sigma_e + \frac{3\phi_s x \sigma_e^*}{1+\phi_s(1-x)+\phi_s^2(1/2-x)/2} + \frac{1-\phi_s}{1+\phi_s/2} i\omega\varepsilon_0\varepsilon_e. \tag{3.58}$$

The equivalence, therefore, can be made:

$$\begin{aligned} \sigma &\equiv \frac{1-\phi_s}{1+\phi_s/2}\sigma_e, \\ \sigma_{surf}^* &\equiv \frac{3\phi_s x \sigma_e^*}{1+\phi_s(1-x)+\phi_s^2(1/2-x)/2}, \\ \sigma_{hf}^* &\equiv \frac{1-\phi_s}{1+\phi_s/2} i\omega\varepsilon_0\varepsilon_e. \end{aligned} \tag{3.59}$$

Note, that in principle the decomposition is not unique and that both σ_{surf} and σ_{hf} contains high-frequency terms that are not zero. However, this decomposition is quite convenient for a better comparison with other models, as will become clear in the next subsection.

THE BUSSIAN MODEL

This model has originally been developed by Bussian [1983] and is based on the Bruggeman expression. It describes the DC electric conductivity of a granular medium formed by charged dielectric spheres in electrolyte solution. This model, and extensions thereof, are presently widely used for porous materials Revil [2013]. From Equation 3.48, the cementation exponent is given by $m = 3/2$ for uncharged spheres. Assuming that the cementation exponent will not be too different for charged spheres (which is true for small Du), Equation 3.46 can be re-written as

$$\sigma_m = \sigma_e \phi^{3/2} \left(\frac{1 - \sigma_g/\sigma_e}{1 - \sigma_g/\sigma_m} \right)^{3/2}, \tag{3.60}$$

see, for example, Appendix A of Revil and Cathles [1999]. The Bussian model is obtained by introducing a particle surface conductivity σ_s which is defined by $\sigma_g \equiv \sigma_s$. Assuming that $\sigma_s/\sigma_e \ll 1$ the Bussian model reads:

$$\sigma_m = \sigma_e \phi^{3/2} \left(1 + \frac{3}{2} \frac{\sigma_s}{\sigma_e} \left(\phi^{-3/2} - 1 \right) \right). \tag{3.61}$$

Many authors [e.g., Börner et al., 2016, Leroy et al., 2008, Revil, 2013] subsequently define a Dukhin number as

$$Du^* \equiv \frac{\sigma_s}{\sigma_e}. \tag{3.62}$$

Let us now compare the Bussian model, based on Bruggeman, with the previous model given by Equation 3.58, based on Maxwell-Wagner. Equation 3.58, which is equivalent to Equation 3.17, gives for DC conditions, using Equations 3.59:

$$\begin{aligned} \sigma_m &= \sigma + \sigma_{surf} = \frac{1 - \phi_s}{1 + \phi_s/2} \sigma_e + \sigma_{surf}, \\ \sigma_{surf} &\simeq \frac{9 \phi_s Du \sigma_e}{4[1 + \phi_s(1 - 3Du/4)]} \end{aligned} \tag{3.63}$$

with $Du \equiv \sigma_{//}/\sigma_e$. The last equivalence is obtained assuming that the term in ϕ_s^2 could be omitted in Equation 3.59. Comparing Equations 3.63 with Equation 3.61 leads to

$$\begin{aligned} m &\equiv ln\left[\frac{\phi}{3/2 - \phi/2} \right] / ln\left[\phi\right] \equiv 3/2, \\ \sigma_{surf} &\simeq \frac{3}{2} \sigma_s \left(1 - \phi^{3/2} \right). \end{aligned} \tag{3.64}$$

The approximation given in Equation 3.64 can be tested using characteristic values for the porosity. For a sandstone with porosity 20%, one finds $m = 1.21$. For an unrealistically high porosity 50%, one gets $m = 1.32$. This gives 20% difference with $m = 3/2$. This difference between the Maxwell-Wagner and the Bruggeman model can be tested at high salinity, when $Du \simeq 0$. The comparison with experimental data is done in the next subsection and we will see that the difference between the models is not very significant. It is, therefore, assumed that in good approximation,

$$\phi^{3/2} \simeq \frac{1 - \phi_s}{1 + \phi_s/2}. \tag{3.65}$$

From Equation 3.64 can be deduced that

$$\sigma_{surf} \simeq \frac{9}{4}\sigma_s \frac{\phi_s}{1+\phi_s/2}. \tag{3.66}$$

Comparing Equations 3.63 and 3.66 leads to

$$\frac{\sigma_{//}}{\sigma_s} \equiv \frac{1+\phi_s(1-3Du/4)}{1+\phi_s/2}. \tag{3.67}$$

In general, there will be some difference between $\sigma_{//}$ and σ_s. Only for low volume fraction (high porosity) one will have $\sigma_{//} = \sigma_s$. In that case, the Equation 3.65 is a very good approximation.

Some authors [e.g., Leroy et al., 2008, Revil, 2013] have accounted for a complex surface conductivity σ_s by extending the Bussian model. They define (see Equation 58 in Leroy et al. [2008])

$$\sigma_s^* \sim \frac{3}{a}\Sigma_S^*. \tag{3.68}$$

The complex conductivity Σ_S^* is obtained from the derivation originally performed by Schwarz [1962]. In Appendix C this surface conductivity Σ_S^* is discussed and linked to $\sigma_{//}$. The presence of the factor 2 is also explained in the Appendix. The conductivity σ_s has to be scaled by a as Leroy et al. [2008] express Σ_S^* as function of Γ's which are surface charge density (number/m^2) and not ionic densities (number/m^3). In Appendix C Σ_S^* is given as function of the ionic density n_k (number/m^3).

3.2.4. COMPARISON WITH MEASUREMENTS

In this subsection, the newly derived expressions for the Maxwell-Wagner and Bruggeman expressions for charged spheres are compared to experimental data. All ionic conductivities are taken equal to the values found in Handbooks. The relative dielectric permittivity of water is taken to be $\varepsilon_e = 80$ and the relative dielectric permittivity of the grain is taken to be the value for silica $\varepsilon_g = 5$. The grains are assumed to be non conductive.

DC ELECTRIC FIELDS MEASUREMENTS

At low frequencies, for silica-based grains one can assume that $\sigma_g^* = \sigma_g \ll \sigma_e$ and the Maxwell-Wagner and the Bruggeman expressions Equations 3.33 and 3.47 for uncharged grains ($Du = 0$) in an electrolyte reduce to

$$\begin{aligned} \sigma_m^{Du=0} &= \sigma_e \frac{1-\phi_s}{1+\phi_s/2} \quad \text{(Maxwell-Wagner)}, \\ \sigma_m^{Du=0} &= \sigma_e \left(1-\phi_s\right)^{3/2} \quad \text{(Bruggeman)}. \end{aligned} \tag{3.69}$$

For low volume fractions, both expressions reduce to:

$$\frac{\sigma_m^{Du=0}}{\sigma_e} = \left(1-\frac{3}{2}\phi_s\right) \quad \text{for} \quad \phi_s \ll 1. \tag{3.70}$$

From Archie' law, one gets:

$$\frac{\sigma_m^{Du=0}}{\sigma_e} = (1-\phi_s)^m = 1 - m\phi_s \quad \text{for} \quad \phi_s \ll 1. \tag{3.71}$$

From the equivalence it follows that $m = 3/2$.

Note that for the Bruggeman expression $m = 3/2$ is valid for the whole range of volume fractions (for uncharged spheres). For the Maxwell-Wagner expression, the equivalence is only true at low volume fractions. For arbitrary volume fractions Equation 3.35 should be used with $Du = 0$. Figure 3.4 shows the differences between the Maxwell-Wagner and the Bruggeman expressions in the case of glass spheres of different diameter. The data is taken from Bolève et al. [2007]. The porosity required to fit the high ionic conductivity is 0.4 for the Maxwell-Wagner expression and 0.46 for the Bruggeman expression. For all sizes the surface charge is determined as function of ionic strength following the procedure given in Appendices A and B (see Figure 3.10 in Appendix A). As can be seen from Figure 3.4, for all particle sizes, the medium conductivity σ_m reduces to $\sigma_m^{Du=0}$ for $\sigma_e \geq 10^{-2}$S/m as expected. It is verified that for all particle sizes a value of $q = 0.0062$ C/m^2 could be used to model the data, regardless of ionic strength. This is possible because of the small dependency of q on σ_e at low σ_e. For large σ_e the Dukhin number is in all cases in good approximation zero. As the available measurements data presented in Figure 3.5 are obtained for different porosities, it is convenient to renormalise the data using Equations 3.69 by

$$\sigma_{eff} = \sigma_m / \sigma_m^{Du=0}. \tag{3.72}$$

This normalization ensures that at high electrolyte conductivity (where $Du = 0$) all the data should be on the $\sigma_{eff} = \sigma_e$ line. The similarly normalized Equations 3.30 and 3.44 are used to evaluate the theoretical curves. For all datasets, both porosity and mean particle size are known. As can be seen in Figure 3.5 there are little differences between the Maxwell-Wagner and the Bruggeman approaches. Both models reproduce quite well the data, and the values found for the surface charge are within reasonable values for silica-based grains, see Appendix B. It is also clear that for all systems investigated, the Maxwell-Wagner and the Bruggeman models for uncharged spheres can safely be used for ionic conductivities larger than 10^{-2} S/m. This is to be expected, as the grains are all about $a \simeq 10\ \mu m$ and therefore, for $\sigma_e = 10^{-2}$ S/m,

$$\kappa a \simeq a\sqrt{\frac{\sigma_e}{\varepsilon_0 \varepsilon_e D}} \simeq 850. \tag{3.73}$$

For the largest surface charge tested ($q = 0.3$ C/m^2), this gives $Du \simeq 0.5$.

The radius of a grain particle, a is related to permeability of porous rock κ_Λ, [Revil and Cathles, 1999, Revil and Florsch, 2010]. The relationship for mono-disperse spherical particles reads

$$\kappa_\Lambda = \frac{a^2\phi^3}{180\left(1-\phi\right)^2}. \tag{3.74}$$

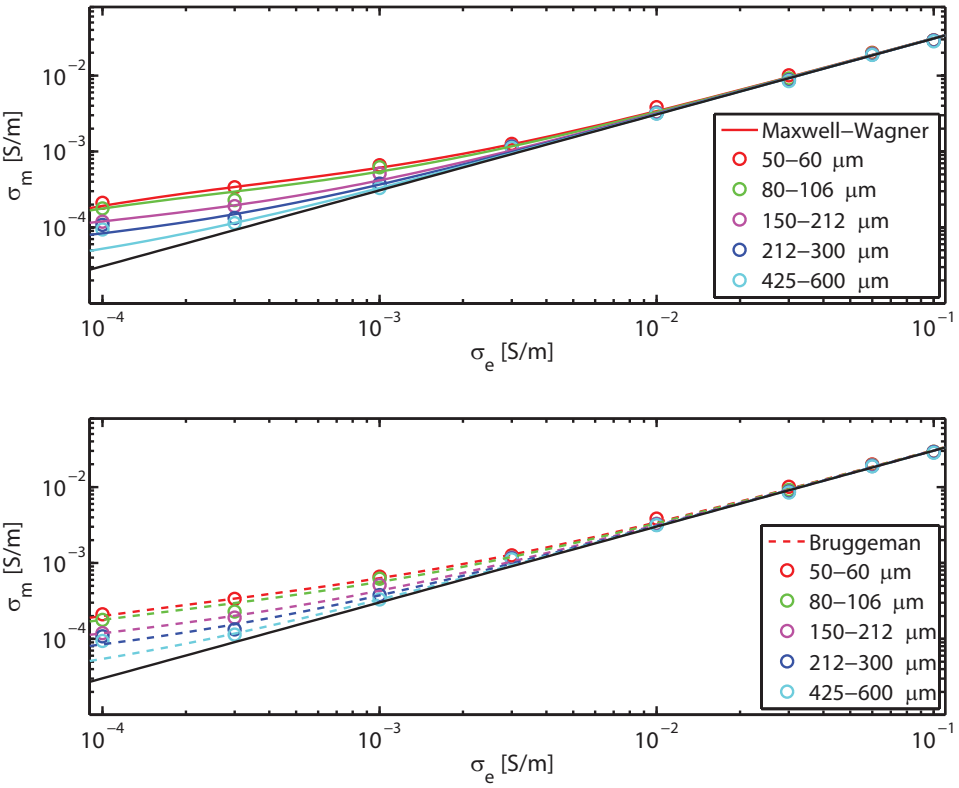

Figure 3.4: Comparison between the Maxwell-Wagner and Bruggeman expressions for charged spheres using a dataset for glass beads, given in Bolève et al. [2007].

3.2.5. AC ELECTRIC FIELDS MEASUREMENTS

Measurements in AC electric fields are quite difficult to perform as unwanted effects hamper the measurements, such as electrode polarization in the case of 2 electrodes measurements Chassagne et al. [2016], or crosstalks in the case of 4 electrodes measurements [Niu et al., 2016].

In the present subsection, the developed Maxwell-Wagner and Bruggeman expressions for charged spheres are tested. As what was observed for DC electric fields, the Maxwell-Wagner and Bruggeman expressions give very close results in the case of AC fields, as can be observed in Figure 3.6. In particular both expressions give the same relaxation frequencies, which was to be expected. Iin the remainder of the subsection the Maxwell-Wagner relation is utilized.

The measured data from Börner et al. [2016] is used in this study. The two experiments represent the dielectric response of the same sandstone of 40% porosity, saturated with 3 mM NaCl, at 25 degrees Celcius and a pressure of 5 MPa. (experiments no 8 and 15 in Börner et al. [2016]), before any injection of gas (hour 14 of the experiment, dark blue line in Figure 9 of Börner et al. [2016]). As can be seen in the figure, even though

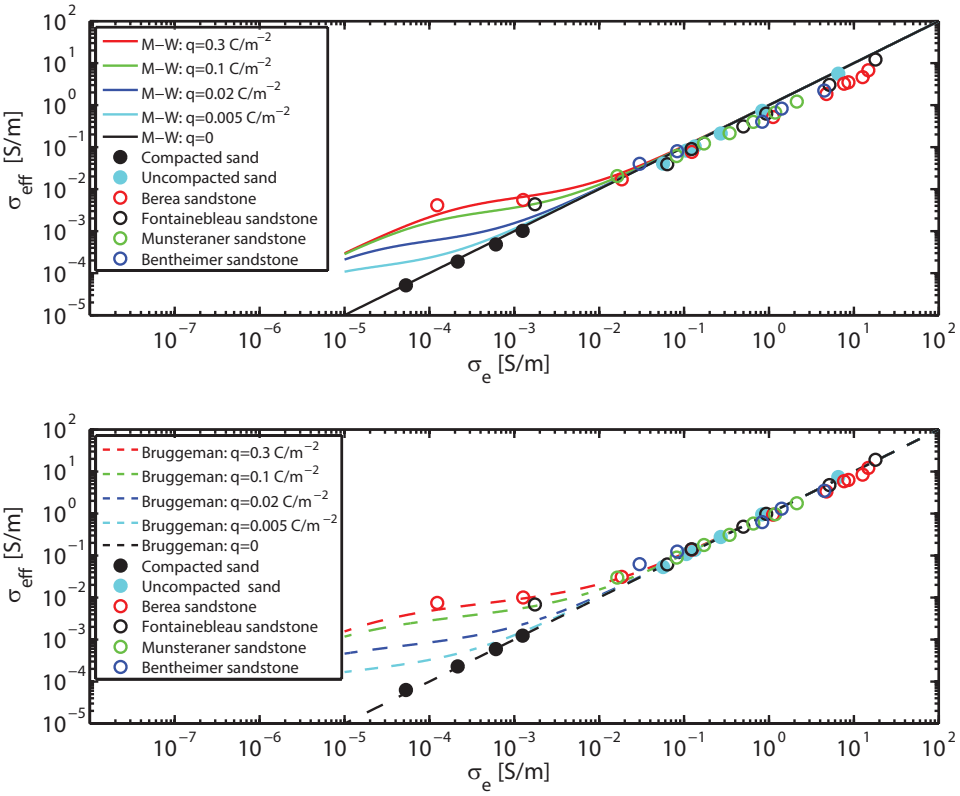

Figure 3.5: Comparison of Maxwell-Wagner and Bruggeman models for granular media with a constant charge density. The conductivity of granular media is normalized in order to avoid the dependence of electrical conductivity on porosity. The data for consolidated sand, unconsolidated sand, Berea sandstone, Fontainebleau sandstone and Munsteraner sandstone are taken from Koch et al. [2012], Slater and Glaser [2003], Glover et al. [1994], Revil et al. [2014] and Weller et al. [2011], respectively. The conductivity of Bentheimer sandstone is measured using the setup described in Chapter 2 with the frequency of 10 kHz.

the values found are quite close in both experiments, the values of the medium conductivity differ by 9%, even though the conductivity of the electrolyte was the same in both experiments (0.037 S/m, see Table 2 in Börner et al. [2016]). An electrolyte conductivity of 0.037 S/m corresponds roughly to a salinity of 2.5 mM NaCl. It is not clear why this salinity does not correspond to the salinity given in Table 2. If the electrolyte conductivity is measured at the end of the experiment, it could be that some chemical reaction has occurred within the porous media resulting in a lowered electrolyte conductivity. As can be seen from Figure 3.7, there is a good match between the dielectric permittivity data and the theoretical prediction when a value of $a = 20$ μm, a surface charge of 0.5 C/m^2 and an electrolyte conductivity of 0.037 S/m are used. At low frequencies, the theoretical prediction becomes constant, while the data shows some increase, most probably due to parasitic electrode effects. At the highest measured frequencies some deviation also occurs that can be due to some unaccounted crosstalks. The electric conductiv-

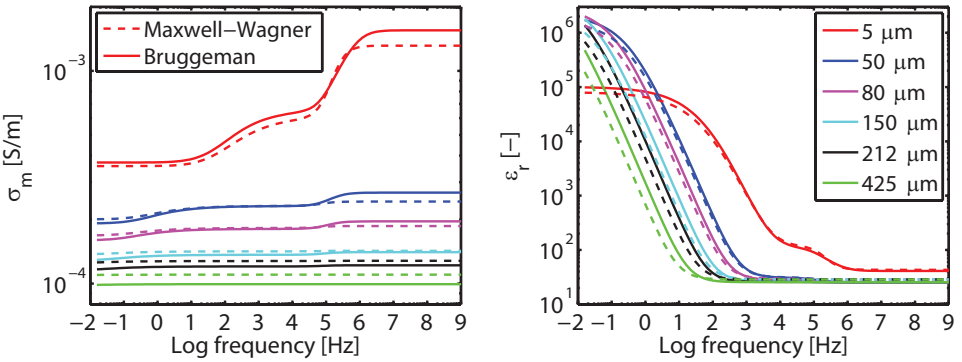

Figure 3.6: Comparison between the Maxwell-Wagner and Bruggeman expressions for charged spheres using various grain sizes.

ity found using the expression for charged spheres is slightly higher (by 20%) than the measured one, which is closer to the conductivity found using the expression for uncharged spheres. One can try to improve the fit, which would be possible by accounting for a Stern layer for example (see Appendix B), as the amount of adjustable parameters is minimized.

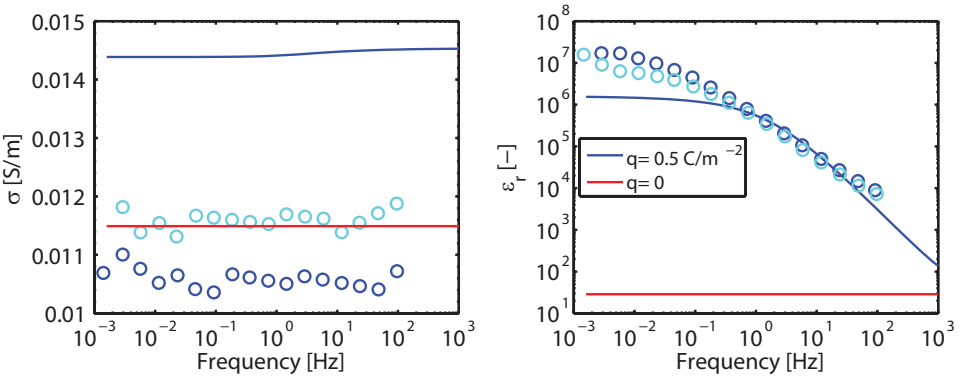

Figure 3.7: Conductivity and dielectric permittivity of a sandstone saturated with 3 mM NaCl. The symbols represent two different datasets from from Börner et al. [2016] . The red solid line shows Maxwell-Wagner relation for uncharged spheres, the blue solid line shows the Maxwell-Wagner expression for charged spheres. The following parameters are used: $a = 20\mu$m and a surface charge of 0.5 C/m^2.

Recently, experiments were performed on a Portland sandstone, which contained some amount of illite and kaolinite, as function of frequency, for a large range of ionic strength Niu et al. [2016]. In that article, the measurements were analyzed using an extended Bussian model making use of a Schwartz-like surface conductivity. Niu et al. [2016] and references therein are referred for further details. From the low-frequency data given in this paper a relation between the medium and electrolyte conductivity, given in Figure 3.8a, was found that enabled to estimate the Dukhin number Du, see

Figure 3.8b, using Equation 3.33. Note that in case of using the porosity given by the authors (0.2), Du becomes negative at high ionic conductivities, which is the consequence of the fact that the medium conductivity would then be larger than the conductivity of a comparable medium (in terms of same porosity and particle size) but composed of uncharged spheres, which is theoretically impossible. This is reflected in the crossing of the full blue curve and the experimental curve (red circles) in Figure 3.8a. For most of the experimental data given in Figure 3.5, it is also usually found that the Maxwell-Wagner expression for uncharged spheres gives slightly highly values than the measured ones at high salinity, and that the Bruggeman expression for charged spheres performs better. The porosity has to be adjusted to 0.05 in order to get a positive Dukhin number. This last value is not realistic, but as can be seen in Figure 3.8b the Du numbers found from using porosities of 0.2 and 0.05 are quite close for the lowest conductivities. This can be understood by realizing that for low frequencies and for large Du Equation 3.30 gives

$$\sigma_m \simeq \sigma_e \frac{1+Du(1+\phi_s/2)}{1+Du(1-\phi_s/4)}, \tag{3.75}$$

which gives quite small differences for σ_m for ϕ_s between 0.8 and 0.95. In the remainder of this subsection, the porosity will be kept equal to 0.2.

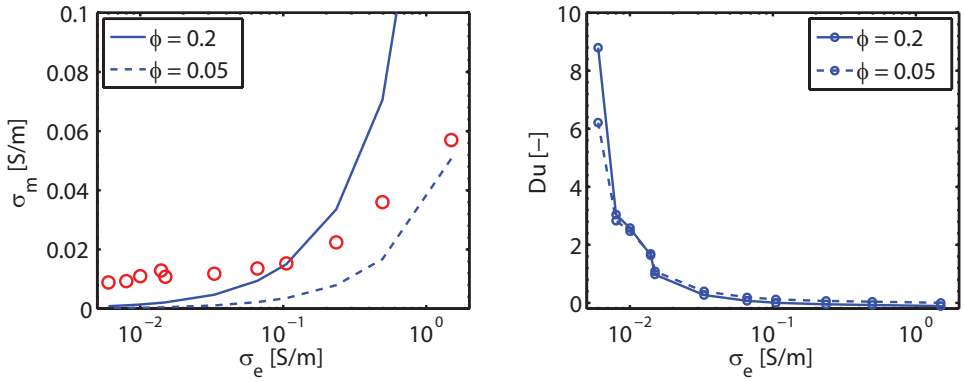

Figure 3.8: Estimation of Du using measured data from Niu et al. [2016]. The values obtained for Du for a 0.2 porosity are given in Table 1 as $Du(\sigma_m)$ using Du and a as adjustable parameters. (a): $Du(\sigma_m)$ used as fit; (b) $Du(\varepsilon_m)$ used as fit. See text for details.

Some of the data given in Niu et al. [2016] is replotted and fitted according to the Maxwell-Wagner expression for charged spheres. Again, the number of adjustable variables is minimal. As recognized by Niu et al. [2016] (their comment in the legend of their Figure 5), some artifacts are observed at very low and very high frequency. Like for the data of Börner et al. [2016], parasitic electrode effects are present at very low frequencies, resulting in an increase in the dielectric permittivity with decreasing frequencies, whereas a constant value is expected. At high frequencies, other unwanted effects took place, resulting in unrealistic high values for the dielectric permittivity. In order to account for these high-frequencies effects, we adjust the dielectric permittivity of the electrolyte in the variable σ_e for each salinity to match the model prediction with the high

frequency value of the sandstone permittivity. The values used in the model are given in Table 1. Two types of fits are performed. Figure 3.9a shows the result of the low frequency fit of the conductivity done be adjusting $Du(\sigma_m)$ and Figure 3.9b shows the result of the dielectric permittivity fit done be adjusting $Du(\varepsilon_m)$. A value of 7 μm is found to be the best grain size for all the fits. The value of q_0 given in Table 1 could then be calculated for $Du(\sigma_m$ or $\varepsilon_m)$, a and σ_e. The model clearly does not reproduce the features of the 0.105 S/m data for either the $Du(\varepsilon_m)$ or the $Du(\sigma_m)$ fit. For lower ionic conductivities, the model gives reasonable predictions. Note however the large difference between the fit parameters for the 0.015 and 0.014 S/m conductivity data. They arise from the unexpected large differences between the conductivities for these datasets.

$$\sigma_m \simeq \sigma_e \frac{1+Du(1+\phi_s/2)}{1+Du(1-\phi_s/4)}, \tag{3.76}$$

which gives quite small differences for σ_m for ϕ_s between 80% and 95%. In the remainder of this subsection, the porosity will be kept equal to 20%.

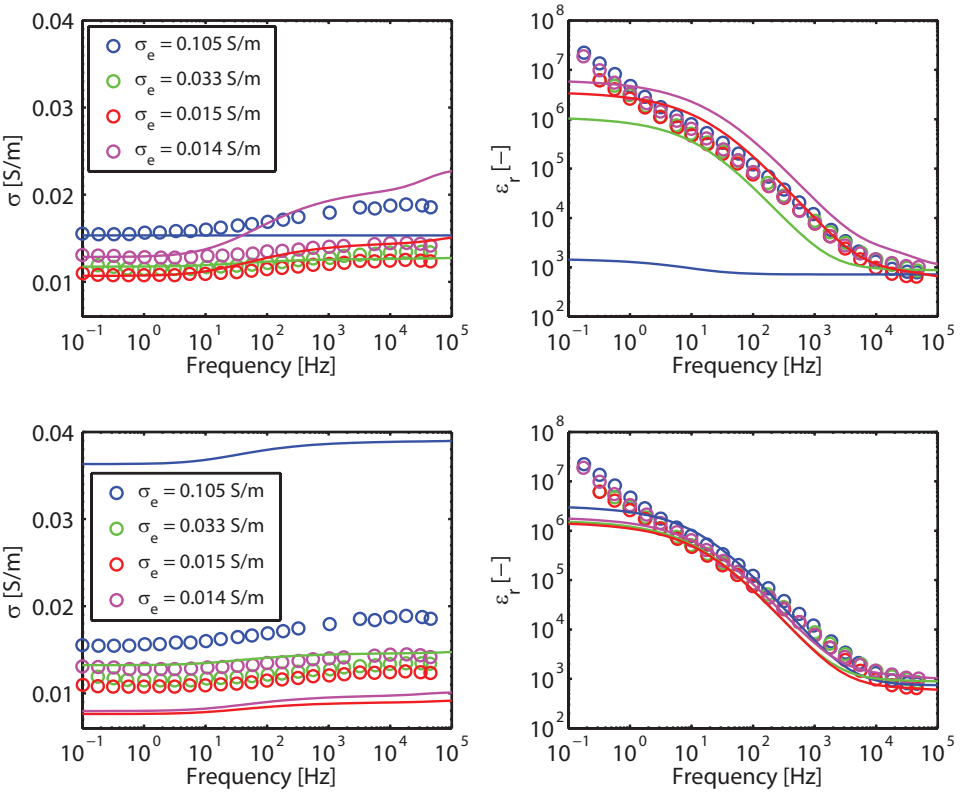

Figure 3.9: Comparison of measured data from Niu et al. [2016] and the Maxwell-Wagner expression for charged spheres.

Table 3.1: Values used in the model (see text for details)

σ_e [S/m]	0.105	0.033	0.015	0.014
a [μm]	7	7	7	7
ε_e	5000	6000	4000	7000
$Du(\varepsilon_m)$	0.2461	0.3214	0.4999	0.6095
q_0 [C/m^2]	0.2461	0.3214	0.4999	0.6095
$Du(\sigma_m)$	0.0031	0.2699	0.9753	1.6444
q_0 [C/m^2]	0.02	0.4	0.65	1.03

3.3. MODELS FOR NON-SPHERICAL AND POLYDISPERSE SPHERES

In the previous subsection it was shown that the Maxwell-Wagner and Bruggeman models for charged spheres enable one to estimate reasonably accurately the different amplitudes and relaxation frequencies of the complex conductivity of granular systems. The fits were not perfect for several reasons. One reason is the uncertainty of the measurement data. Dielectric spectroscopy measurements are very difficult to perform accurately at low and high frequencies for many technical reasons. From the results of the previous section, it can be seen that even small deviations for the conductivity data results in large changes in the fit results. High frequency inaccuracies in the dielectric permittivity increment (resulting from inaccuracies in the phase measurement), on the other hand, can better be compensated for. The other reasons for the discrepancies between the model and the data stem from the model. The model was derived assuming that the particles were all monodisperse spheres. Sandstones can contain polydisperse and/or non-spherical particles. In the present section we will briefly discuss on how to account for non-sphericity and polydispersity.

3.3.1. NON-SPHERICAL PARTICLES

The dipolar coefficient in Equation 3.24, that was used to set-up both the Maxwell-Wagner and the Bruggeman expressions for charged spheres, can quite easily be extended for charged spheroidal particles. Such general expression is given as Equation 1 in Chassagne and Bedeaux [2008]. Sen et al. give in the Appendix of Sen et al. [1981] similar expressions for uncharged spheroidal particles and the associated the Bruggeman expression. Clays can in first approximation be approximated by either prolate or oblate spheroids Chassagne et al. [2009].

3.3.2. POLYDISPERSE SAMPLES

The Maxwell-Wagner and the Bruggeman expressions for charged spheres can easily be extended to account for polydispersity. Let us assume that the granular material is polydisperse. For the sake of argument we only consider a granular material composed of two types of grains (labeled 1 and 2), but the reasoning be extended to more classes of particles in a straightforward manner. A relation between the different volume fractions is given by

$$1 = \frac{V_{tot}}{V_{tot}} = \frac{V_w + V_1 + V_2}{V_{tot}} = \phi_s^w + \phi_s^1 + \phi_s^2 = \phi_s^w + \phi_s, \tag{3.77}$$

where ϕ_s^w, ϕ_s^1, ϕ_s^2 represent the volume fractions of water, particles of type 1 and particles of type 2. Equation 3.17 gives

$$\sigma_m^* = \sigma_e^* \frac{1 + 2(\phi_s^1 \beta_1^* + \phi_s^2 \beta_2^*)}{1 - (\phi_s^1 \beta_1^* + \phi_s^2 \beta_2^*)}. \tag{3.78}$$

Each dipolar coefficient can be written

$$\beta_k^*(\omega = 0) \simeq \frac{-1}{2}\left(1 - \frac{3}{2} Du_k\right), \tag{3.79}$$

which enables to derive the DC conductivity of the polydisperse granular medium as

$$\sigma_m = \frac{1 - \phi_s}{1 + \phi_s/2}\sigma_e + \frac{9(\phi_s^1 Du_1 + \phi_s^2 Du_2)\sigma_e}{4[1 + \phi_s - 3/4(\phi_s^1 Du_1 + \phi_s^2 Du_2)]}. \tag{3.80}$$

From this equation it appears that the second term on the right-hand-side will be dominated by the particle type displaying the highest product $(\phi_s Du)$. This could be particularly important in the case of shale sands as the clay fraction particles have typically a smaller size and higher charge than the sand particles. If their volume fraction ϕ_s is large enough, the medium conductivity σ_m at low salinity will therefore be dominated by the clay fraction.

3.4. CONCLUSION

In this chapter, analytical expressions for the electrokinetic response of immobile grains representative for (un)compacted sands and sandstones in an electrolyte solution are presented. The grains can be charged and the associated electrolyte can be of any ionic strength. The main assumption made is that the grains' double layers do not overlap. The extension to spheroidal particles and polydisperse grains is given. The derived models can be applied to a CO_2 storage reservoir rock. Two main expressions are presented, one based on the Maxwell-Wagner and the other on the Bruggeman formalism. It is found that both expressions lead to not-so-different results, and that they could correctly reproduce the features of some representative measured datasets given in the third section, using at most two adjustable parameters. These parameters, the mean particle size and the particle's mean surface charge (or the mean particle size and mean Dukhin number) are found to be in the range of what can be expected for sands and sandstones. Percolation thresholds are not considered, nor is pore clogging. This implies that the models are valid for porous media in which each particle (grain) has nearly all of its surface in contact with the electrolyte.

3.5. APPENDIX A: pH DEPENDENCE OF THE SURFACE CHARGE

So far, we only particles with a given zeta potential have been considered and the zeta potential has been defined as being the surface potential of the particle: this implies that it has been assumed that there is no Stern layer. The surface potential of the particle should be linked to its surface charge since surface charge is a measurable quantity (by

titration for example). The relation between surface charge density $q_{eq}(a)$ and potential $\Psi_{eq}(a)$ is given by Gauss' law:

$$\left(\frac{\partial \Psi_{eq}}{\partial r}\right)_{r=a} = \frac{-q_{eq}(a)}{\varepsilon_0 \varepsilon_e}. \tag{3.81}$$

Solving this equation requires to solve the non-linear Poisson-Boltzmann equation, however there exists a very good approximation for symmetric monovalent electrolytes [Russel et al., 1989]:

$$q_{eq}(a) = \frac{\varepsilon_0 \varepsilon_e kT}{e} \kappa \left[2 \sinh\left(\frac{e\Psi_{eq}(a)}{2kT}\right) + \frac{4}{\kappa a} \tanh\left(\frac{e\Psi_{eq}(a)}{4kT}\right)\right]. \tag{3.82}$$

In most cases encountered experimentally $\kappa a >> 1$ and Equation 3.82 can be simplified to provide an expression for $\Psi_{eq}(a)$:

$$\frac{e\Psi_{eq}(a)}{kT} = 2 \operatorname{asinh}\left(\frac{eq_{eq}(a)}{2\varepsilon_0 \varepsilon_e kT\kappa}\right). \tag{3.83}$$

It is emphasized that $q_{eq}(a)$ is the surface charge density in the absence of any applied electric field and that this surface charge can be pH/pK dependent. From the value of $q_{eq}(\text{pH,pK})$ the zeta potential $\zeta(\text{pH,pK})$ can be back-calculated assuming that (1) there is no Stern layer and (2) the shear plane is located at $r = a$ from which one gets

$$\Psi_{eq}(a) = \zeta. \tag{3.84}$$

The salt-concentration dependence in Equation 3.82 through the term κ only reflects the presence of the double-layer close to the particle's surface, i.e. the presence of indifferent ions (ions that do not chemically interact with the surface). Some authors [Revil

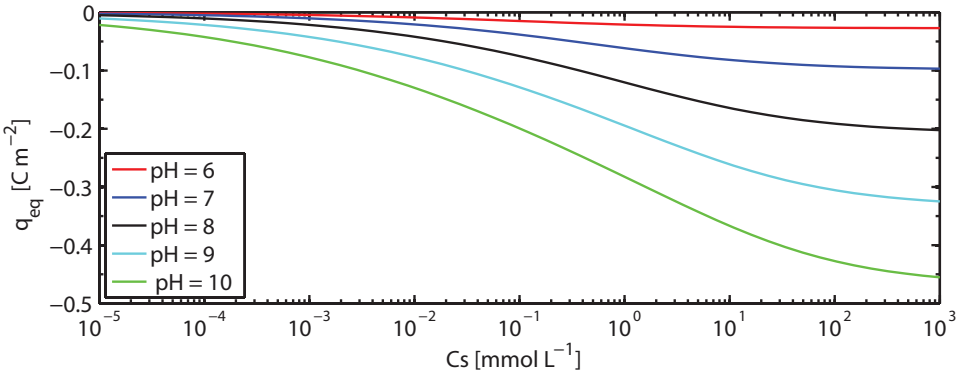

Figure 3.10: Evolution of the surface charge density with salt concentration

and Glover, 1997] define $q_{eq}(a) = Q_S^0 = e\Gamma_S^0$ in terms of charge dissociation parameters. They have extremely complicated expressions as they account for multiple chemical reactions. To give insight in what they do, only one reaction will be considered, ie:

$$-AH = -A^- + H^+. \tag{3.85}$$

The corresponding mass action law for the surface equilibrium is given by:

$$a_{H^+}\frac{\Gamma_{A^-}}{\Gamma_{AH}} = K\exp\left(\frac{e\Psi_{eq}(a)}{kT}\right), \tag{3.86}$$

where the activity coefficient a_{H^+} and the dissociation constant K are related to the pH of the solution and the pK of the chemical reaction by

$$\begin{aligned} \mathrm{pH} &= -\log(a_{H^+}), \\ \mathrm{pK} &= -\log(K). \end{aligned} \tag{3.87}$$

The pH can be measured and the pK can be found in the Handbook of Chemistry. The total concentration of surface sites reads:

$$\Gamma^0 = \Gamma_{A^-} + \Gamma_{AH}, \tag{3.88}$$

while the surface charge density originating from the dissociated groups reads:

$$q_{eq}(a) = Q_S^0 = e\Gamma_S^0 = -e\Gamma_{A^-}. \tag{3.89}$$

Combining the previous equations leads to:

$$\Gamma^0 = \Gamma_{A^-}\left[1 + \frac{10^{-\mathrm{pH}}}{K\exp\left(e\Psi_{eq}(a)/kT\right)}\right]. \tag{3.90}$$

Note that usually one defines

$$\Psi_N = \frac{kT}{e}\left[\mathrm{pK} - \mathrm{pH}\right]\ln(10), \tag{3.91}$$

in which case it is possible to write:

$$\Gamma^0 = \Gamma_{A^-}\left[1 + \frac{1}{\exp\left(e\left[\Psi_{eq}(a) - \Psi_N\right]/kT\right)}\right], \tag{3.92}$$

from which one gets:

$$q_{eq}(a) = \frac{-e\Gamma^0\exp\left(e\left[\Psi_{eq}(a) - \Psi_N\right]/kT\right)}{\exp\left(e\left[\Psi_{eq}(a) - \Psi_N\right]/kT\right) + 1}. \tag{3.93}$$

In order to solve this equation, one should know $\Psi_{eq}(a)$. An expression is given in Equation 3.82 which links $\Psi_{eq}(a)$ and $q_{eq}(a)$. This gives us two equations with two unknowns.

3.6. APPENDIX B: INCLUSION OF A STERN LAYER

Ions in the Stern layer can also contribute to the medium conductivity and will also depend on the existing dissociated surface sites. However, expressions for including a Stern layer contribution will depend on several factors that are difficult, if not impossible to

quantify, to name a few: the exact position of the shear plane (defining which ions in the Stern layer will be mobile or not), the mobility of the ions in the Stern layer (which is most probably different from their bulk mobility), the spatial extension of the chemisorbed ions (which will define the inner and outer Helmholtz plane) [Dukhin, 1952]. This is why the Stern layer conductivity (which can be in theory a complex number i.e. frequency-dependent) is usually chosen to be an adjustable variable and included in the dipolar coefficient as an additional shell layer.

In the traditional description of the Stern layer however, the Stern layer is seen as a dielectric medium, with no conductivity. One relates the surface potential $\Psi_{eq}(a)$ to the electric potential at the beginning of the diffuse layer $\Psi_{eq}(a+d)$ by an unknown Stern layer capacitance C_{Stern}

$$C_{Stern} = \frac{q_{eq}(a)}{\Psi_{eq}(a) - \Psi_{eq}(a+d)} \tag{3.94}$$

When this occurs Equation 3.82 should be changed into [Russel et al., 1989]:

$$q_{eq}(a+d) = \frac{\varepsilon_0 \varepsilon_e kT}{e} \kappa \left[2\sinh\left(\frac{e\Psi_{eq}(a+d)}{2kT} \right) + \frac{4}{\kappa a} \tanh\left(\frac{e\Psi_{eq}(a+d)}{4kT} \right) \right], \tag{3.95}$$

as $q_{eq}(a+d)$ now represents the surface charge at the beginning of the diffuse double layer. Solving the set of Equations 3.93,3.94 and 3.95 together with

$$q_{eq}(a) + q_{eq}(a+d) = 0 \tag{3.96}$$

gives the value of surface charge density of the particle, $q_{eq}(a)$, as function of ionic strength, pH and pK. From the same equations $\Psi_{eq}(a)$ and $\Psi_{eq}(a+d)$ can be obtained. The zeta potential is not mentioned in this case. Above it was assumed that in the case of no Stern layer,

$$\Psi_{eq}(a) = \zeta \tag{3.97}$$

In the presence of a Stern layer it is usually assumed that

$$\Psi_{eq}(a+d) = \zeta. \tag{3.98}$$

As d and C_{Stern} remain unknown, changing the position of the shear plane will only affect these parameters, so there is no benefit is discussing its exact position. The following example gives the surface charge of silica as function of ionic strength assuming that the Stern layer is a dielectric medium, using the following parameters, taken from Behrens and Grier [2001]: $pK = 7.5$, $C_{Stern} = 2.9$ [F/m^2], $\Gamma^0 = 8$ nm^{-2}.

The traditional description of the Stern layer discussed above is to be adapted when an electric field is applied to the system. It is then usually assumed that (part of) ions are mobile within the Stern layer. This implies that the Stern layer is not a pure dielectric medium, and that a Stern layer conductance should be accounted for. A Stern layer conductivity can easily be added to the dipolar coefficient Equation 3.24, following the procedure given in the shell model subsection. This leads to the new dipolar coefficient [Chassagne et al., 2003]

$$\beta^* = \frac{\sigma_g^* - \sigma_e^* + \sigma_{//}(1 - J_1/J_2) + \sigma_{//}^{*St} + \sigma_{\perp}^{*St}}{\sigma_g^* + 2\sigma_e^* + \sigma_{//}(1 + 2J_1/J_2) + \sigma_{//}^{*St} - \sigma_{\perp}^{*St}}, \tag{3.99}$$

where $\sigma_{//}^{*St}$ and $\sigma_{\perp}^{*St}$ are the (complex) conductivities for the Stern layer parallel and perpendicular to the particle's surface. By fitting data on suspensions, it was found that

$$\sigma_{//}^{*St} = \sigma_{\perp}^{*St} = St \times \sigma_e, \tag{3.100}$$

where St is a real coefficient, which make both $\sigma_{//}^{*St}$ and $\sigma_{\perp}^{*St}$ real variables. This choice gives the same local field as when no Stern layer is introduced and corresponds to what many authors do: St is similar to the Θ introduced by Lyklema and Minor [1998] and similar coefficients have been used by Kijlstra et al. [1992] and Rosen et al. [1993].

3.7. APPENDIX C: ELECTROKINETIC THEORY

GENERAL EQUATIONS

A general set of equations of standard Elekrokinetic theory can be found in DeLacey and White [1981]-Mangelsdorf and White [1997]. Here, the analysis to electrolytes of type "symmetric" electrolytes with equal ionic diffusion coefficients $D_+ = D_- = D$ and of valence $z_+ = -z_- = 1$ is presented. The considered charged particle is a spherical and dielectric of radius a and is subjected to an electric field E_0 of radial frequency ω. The origin of the spherical coordinate system is the center of the particle. No fluid flow and no Stern layer contributions are considered.

The following variables are considered:

- Ψ_{eq} the equilibrium potential, no applied electric field
- $n_{+,eq}$ the ionic density of positively charged ions, no applied electric field
- $n_{-,eq}$ the ionic density of negatively charged ions, no applied electric field
- ψ the potential due to the applied electric field
- n_+ the ionic density of positively charged ions due to the applied electric field
- n_- the ionic density of negatively charged ions due to the applied electric field

$$\begin{aligned} \Psi_{total} &= \Psi_{eq} + \delta\Psi, \\ n_{+,total} &= n_{+,eq} + \delta n_+, \\ n_{-,total} &= n_{-,eq} + \delta n_-, \end{aligned} \tag{3.101}$$

where, due to the spherical symmetry of the system

$$\begin{aligned} \delta\Psi &= (\psi - r)E_0\cos\theta, \\ \delta n_+ &= n_+ E_0\cos\theta, \\ \delta n_- &= n_- E_0\cos\theta, \end{aligned} \tag{3.102}$$

with θ being the angle of the direction of the electric field.
In the case with no applied electric field, one obtains $\delta\Psi = \delta n_+ = \delta n_- = E_0 = 0$. Futhermore, the following is introduced in Chassagne and Bedeaux [2008]:

$$\begin{aligned} n_n &= n_+ + n_- \quad (\text{similarly: } n_{n,eq} = n_{+,eq} + n_{-,eq}), \\ n_c &= n_+ - n_- \quad (\text{similarly: } n_{c,eq} = n_{+,eq} - n_{-,eq}). \end{aligned} \tag{3.103}$$

with

$$\begin{aligned} n_+ &= \frac{1}{2}(n_n + n_c) \quad \text{and} \quad n_- = \frac{1}{2}(n_n - n_c), \\ n_{+,eq} &= \frac{1}{2}\left(n_{n,eq} + n_{c,eq}\right) \quad \text{and} \quad n_{-,eq} = \frac{1}{2}\left(n_{n,eq} - n_{c,eq}\right). \end{aligned} \tag{3.104}$$

The operator L that will be needed in the following is defined on a function f by:

$$Lf = \frac{1}{r}\frac{d^2}{dr^2} rf - \frac{2f}{r^2}. \tag{3.105}$$

NO APPLIED ELECTRIC FIELD

In the case with no applied electric field, the Poisson equation relates Ψ_{eq} to $n_{c,eq}$ by:

$$\nabla^2 \Psi_{eq} = \frac{-e}{\varepsilon_0 \varepsilon_1} n_{c,eq}, \tag{3.106}$$

where e is the absolute value of the electron charge, ε_1 the relative dielectric permittivity of the solvent and ε_0 is the dielectric permittivity of vacuum. The electrochemical potential $\mu_{i,eq}$ of ion i is defined by:

$$\mu_{i,eq} = z_i e \Psi_{eq} + \mu^0_{i,eq} + kT \ln\left(\frac{n_{i,eq}}{n_0}\right), \tag{3.107}$$

where $\mu^0_{i,eq}$ and n_0 are reference chemical potential and density, respectively. k is the Boltzmann constant and T is the temperature. The ionic fluxes are defined by:

$$\mathbf{J}_{i,eq} = \frac{-D n_{i,eq}}{kT} \nabla \mu_{i,eq}. \tag{3.108}$$

Since the electrochemical potential in the system is constant one can write

$$\begin{aligned} \mu_{i,eq}(r) &= \mu_{i,eq}(\infty), \\ z_i e \Psi_{eq} + \mu^0_{i,eq} + kT \ln\left(\frac{n_i}{n_0}\right) &= z_i e \cdot 0 + \mu^0_{i,eq} + kT \ln\left(\frac{n_\infty}{n_0}\right). \end{aligned} \tag{3.109}$$

This leads to the Boltzmann distribution:

$$n_{i,eq} = n_\infty \exp\left(\frac{-e z_i \Psi_{eq}}{kT}\right). \tag{3.110}$$

Hence, one can write

$$\begin{aligned} n_{+,eq} &= n_\infty \exp\left(\frac{-e\Psi_{eq}}{kT}\right) \quad \text{and} \quad n_{-,eq} = n_\infty \exp\left(\frac{e\Psi_{eq}}{kT}\right), \\ n_{n,eq} &= 2n_\infty \cosh\left(\frac{e\Psi_{eq}}{kT}\right) \quad \text{and} \quad n_{c,eq} = -2n_\infty \sinh\left(\frac{e\Psi_{eq}}{kT}\right), \\ \Delta\left(\frac{e\Psi_{eq}}{kT}\right) &= \frac{1}{r}\frac{\partial^2}{\partial r^2}\left(r\frac{e\Psi_{eq}}{kT}\right) = \kappa^2 \sinh\left(\frac{e\Psi_{eq}}{kT}\right). \end{aligned} \tag{3.111}$$

The slip plane is defined, where the zeta potential is defined, as to coincide with the surface of the particle:

$$\Psi_{eq}(r=a)=\zeta. \tag{3.112}$$

Far from the particle and its double layer (where $\sinh(\Psi_{eq})\simeq\Psi_{eq}$), the potential has the asymptotic expression:

$$\Psi^{+}_{eq}=\Psi_0 a\exp(\kappa a-\kappa r)/r, \tag{3.113}$$

where Ψ_0 is an unknown coefficient which depends on ζ and κ and that can be found by numerical integration in the general case.

WITH APPLIED ELECTRIC FIELD

The electrolyte is considered to be at rest in the frame of reference, hence forces of hydrodynamical origin are not considered. A more general set of equations can be found in DeLacey and White [1981] and Mangelsdorf and White [1997]. If the applied electric field is considered, Poisson links $\delta\Psi$ to δn_c by

$$\nabla^2\delta\Psi=\frac{-1}{\varepsilon_0\varepsilon_1}\sum ez_i\delta n_i=\frac{-e}{\varepsilon_0\varepsilon_1}\delta n_c. \tag{3.114}$$

The Nernst-Planck (conservation of mass) equation can be written:

$$i\omega\delta n_i=D\vec{\nabla}\cdot\left[n_{i,eq}\vec{\nabla}\left(\frac{z_i e}{kT}\delta\Psi+\frac{\delta n_i}{n_{i,eq}}\right)\right]. \tag{3.115}$$

Using the fact that

$$\vec{\nabla}n_{i,eq}=-\frac{ez_i}{kT}n_{i,eq}\vec{\nabla}\Psi_{eq}, \tag{3.116}$$

one can get:

$$\frac{i\omega}{D}\delta n_i=\triangle\delta n_i+\frac{ez_i}{kT}\left[-\frac{ez_i}{kT}n_{i,eq}\vec{\nabla}\Psi_{eq}\vec{\nabla}\delta\Psi+n_{i,eq}\triangle\delta\Psi+\vec{\nabla}\delta n_i\vec{\nabla}\Psi_{eq}+\delta n_i\triangle\Psi_{eq}\right].$$

From Equation 3.102 one has:

$$\begin{aligned}
\frac{d\delta\Psi}{dr} &= \left(\frac{d\psi}{dr}-1\right)E_0\cos\theta,\\
\triangle_r\delta\Psi &= \frac{-e}{\varepsilon_0\varepsilon_1}(n_+-n_-)E_0\cos\theta=(L\psi)E_0\cos\theta,\\
\frac{d\delta n_i}{dr} &= \frac{dn_i}{dr}E_0\cos\theta,\\
\triangle_r\delta n_i &= \left(\triangle n_i-\frac{2n_i}{r^2}\right)E_0\cos\theta=E_0\cos\theta Ln_i.
\end{aligned} \tag{3.117}$$

This leads to:

$$\begin{aligned}
\frac{i\omega}{D}n_i = {} & Ln_i+\frac{z_i e}{kT}\frac{d\Psi_{eq}}{dr}\left[\frac{-z_i e}{kT}\left(\frac{d\psi}{dr}-1\right)n_{i,eq}+\frac{dn_i}{dr}\right]\\
& -\frac{z_i e^2 n_{i,eq}}{\varepsilon_0\varepsilon_1 kT}(n_+-n_-)+n_i\frac{z_i e}{kT}\left[\frac{d^2\Psi_{eq}}{dr^2}+\frac{2}{r}\frac{d\Psi_{eq}}{dr}\right].
\end{aligned} \tag{3.118}$$

Rewriting this equation in terms of n_n and n_c, one gets:

$$\begin{aligned} Ln_n &= \frac{i\omega}{D}n_n + \frac{e}{kT}\frac{d\Psi_{eq}}{dr}\left[\frac{e}{kT}\left(\frac{d\psi}{dr}-1\right)n_{n,eq} - \frac{dn_c}{dr}\right] + \frac{e^2 n_{c,eq} n_c}{\varepsilon_0\varepsilon_1 kT} - n_c\frac{e}{kT}\left[\frac{d^2\Psi_{eq}}{dr^2} + \frac{2}{r}\frac{d\Psi_{eq}}{dr}\right], \\ Ln_c &= \frac{i\omega}{D}n_c + \frac{e}{kT}\frac{d\Psi_{eq}}{dr}\left[\frac{e}{kT}\left(\frac{d\psi}{dr}-1\right)n_{c,eq} - \frac{dn_n}{dr}\right] + \frac{e^2 n_{n,eq} n_c}{\varepsilon_0\varepsilon_1 kT} - n_n\frac{e}{kT}\left[\frac{d^2\Psi_{eq}}{dr^2} + \frac{2}{r}\frac{d\Psi_{eq}}{dr}\right]. \end{aligned}$$

The Poisson equation reduces to:

$$L\psi = \frac{-e}{\varepsilon_0\varepsilon_1}(n_+ - n_-) = \frac{-e}{\varepsilon_0\varepsilon_1}n_c. \tag{3.119}$$

The boundary conditions at the surface of the particle for the electric potentials are:

$$\begin{aligned} \varepsilon_0\varepsilon_2\left(\frac{d(\delta\Psi_2)}{dr}\right)_{r=a} &= \varepsilon_0\varepsilon_1\left(\frac{d(\delta\Psi)}{dr}\right)_{r=a}, \\ \delta\Psi_2(a) &= \delta\Psi(a), \end{aligned} \tag{3.120}$$

where $\delta\Psi_2$ is the potential inside the dielectric sphere and is a solution of the Laplace equation ($\Delta\delta\Psi_2 = 0$), which gives:

$$\delta\Psi_2 = -E_2 r\cos\theta, \tag{3.121}$$

where E_2 is a coefficient that can be eliminated by combining Equations 3.120:

$$\begin{aligned} \left(\frac{d(\delta\Psi)}{dr}\right)_{r=a} &= \frac{\varepsilon_2}{\varepsilon_1}\frac{\delta\Psi(a)}{a}, \\ \left(\frac{d\psi}{dr}\right)_{r=a} - \frac{\varepsilon_2}{\varepsilon_1}\frac{\psi(a)}{a} &= \frac{\varepsilon_1-\varepsilon_2}{\varepsilon_1}. \end{aligned} \tag{3.122}$$

The no-flux condition provides the last boundary condition:

$$(\mathbf{J}_i\cdot\mathbf{e}_r)_{r=a} = 0, \tag{3.123}$$

which for the electrolyte considered here leads to:

$$\begin{aligned} \frac{d}{dr}\left[e\delta\Psi + kT\frac{\delta n_+}{n_{+,eq}}\right]_{r=a} &= 0, \\ \frac{d}{dr}\left[-e\delta\Psi + kT\frac{\delta n_-}{n_{-,eq}}\right]_{r=a} &= 0. \end{aligned} \tag{3.124}$$

These equations give:

$$\begin{aligned} n_{+,eq}\frac{e}{kT}\left(\frac{d\psi}{dr}-1\right) + \frac{dn_+}{dr} + n_+\frac{e}{kT}\frac{d\Psi_{eq}}{dx} &= 0 \quad \text{in} \quad r=a, \\ -n_{-,eq}\frac{e}{kT}\left(\frac{d\psi}{dr}-1\right) + \frac{dn_-}{dr} - n_-\frac{e}{kT}\frac{d\Psi_{eq}}{dr} &= 0 \quad \text{in} \quad r=a. \end{aligned} \tag{3.125}$$

Summing and substracting these two equations one gets:

$$\begin{aligned}\frac{e}{kT}\left(\frac{d\psi}{dr}-1\right)n_{c,eq}+\frac{dn_n}{dr}+n_c\frac{e}{kT}\frac{d\Psi_{eq}}{dr} &= 0 \quad \text{in} \quad r=a,\\ \frac{e}{kT}\left(\frac{d\psi}{dr}-1\right)n_{n,eq}+\frac{dn_c}{dr}+n_n\frac{e}{kT}\frac{d\Psi_{eq}}{dr} &= 0 \quad \text{in} \quad r=a.\end{aligned} \tag{3.126}$$

Beyond the double layer (for $r \gg a+\kappa^{-1}$), one has:

$$\begin{aligned}\Psi_{eq} &\rightarrow 0,\\ \frac{d\Psi_{eq}}{dr} &\rightarrow 0\\ n_{c,eq} &\rightarrow 0,\\ n_{n,eq} &\rightarrow 2n_\infty\end{aligned} \tag{3.127}$$

and the equations eqs.(3.119) reduce to:

$$\begin{aligned}Ln_n^+ &= \frac{i\omega}{D}n_n^+,\\ Ln_c^+ &= \left(\kappa^2+\frac{i\omega}{D}\right)n_c^+,\end{aligned} \tag{3.128}$$

which can be solved analytically [Chassagne et al., 2003]:

$$\begin{aligned}n_n^+ &= C_n\frac{1+\lambda_n r}{r^2}\exp\left[-\lambda_n(r-a)\right] \quad \text{and} \quad \lambda_n=\sqrt{i\omega/D},\\ n_c^+ &= C_c\frac{1+\lambda_c r}{r^2}\exp\left[-\lambda_c(r-a)\right] \quad \text{and} \quad \lambda_c=\sqrt{\kappa^2+i\omega/D}.\end{aligned}$$

As $n_c^+ \simeq 0$ beyond the double layer, Equation 3.119 can be solved analytically beyond the double layer in:

$$\begin{aligned}\psi^+ &= \beta\frac{a^3}{r^2},\\ \frac{d\psi^+}{dr} &= \frac{-2}{r}\psi^+,\end{aligned} \tag{3.129}$$

where β is the dipolar coefficient to be found.

ANALYTICAL THEORY

In Chassagne et al. [2003] a new analysis is presented. The analysis is presented here in a different way.

The boundary conditions, Equations 3.120 and 3.123, are now replaced by new ones which will allow us to get an analytical solution. New boundary conditions, can be written for the symmetric electrolyte as:

$$\delta\Psi^+(a)=\delta\Psi_2(a), \tag{3.130}$$

$$\varepsilon_0\varepsilon_2\left(\frac{\partial\delta\Psi_2}{\partial r}\right)_{r=a}-\varepsilon_0\varepsilon_1\left(\frac{\partial\delta\Psi^+}{\partial r}\right)_{r=a}=\delta\rho^S(a), \tag{3.131}$$

$$i\omega\delta n_i^S(a)=-\nabla\cdot\mathbf{J}_{i,\shortparallel}^S(a)-J_{i,\perp}^+(a), \tag{3.132}$$

where:

$$\begin{aligned}
\delta\Psi^+(r) &= \left(-r+\beta\frac{a^3}{r^2}\right)E_0\cos\theta \quad \text{as one has:} \quad \Delta\delta\Psi^+=0,\\
\delta\Psi_2(r) &= -E_2 r\cos\theta,\\
\delta\rho^S(a) &= \sum_i ez_i\delta n_i^S(a)=e\delta n_+^S(a)-e\delta n_-^S(a)=e\delta n_c^S(a),\\
\delta n_i^S(a) &= \frac{1}{a^2}\int_a^\infty r^2\left[\delta n_i-\delta n_i^+\right]dr,\\
\mathbf{J}_{i,\shortparallel}^S(a) &= \frac{1}{a}\int_a^\infty r\left[\mathbf{J}_{i,\shortparallel}-\mathbf{J}_{i,\shortparallel}^+\right]dr,\\
&= \frac{-D}{a}\int_a^\infty r\left[n_{i,eq}-n_{i,eq}^+\right]dr\cdot\nabla_{\shortparallel}\left[\frac{z_ie}{kT}\delta\Psi^+(a)+\frac{\delta n_i^+(a)}{n_\infty}\right].
\end{aligned} \tag{3.133}$$

$\nabla_{\shortparallel}\left[z_ie\delta\Psi(r)/kT+\delta n_i(r)/n_\infty\right]$ and $\nabla_{\shortparallel}\left[z_ie\delta\Psi^+(r)/kT+\delta n_i^+(r)/n_\infty\right]$ are assumed to vary slowly in the double layer and are equal to the extrapolated value $\nabla_{\shortparallel}\left[z_ie\delta\Psi^+(a)/kT+\delta n_i^+(a)/n_\infty\right]$. This means that one can make the common local equilibrium assumption for the electrochemical potentials $\delta\mu_i$ and $\delta\mu_i^+$

$$J_{i,\perp}^+(a)=-D\frac{\partial}{\partial r}\left[\frac{z_ien_\infty}{kT}\delta\Psi^+(r)+\delta n_i^+(r)\right]_{r=a}. \tag{3.134}$$

One defines J_1 and J_2 such that:

$$\begin{aligned}
\delta n_n^+(a) &= C_n\frac{J_1}{a^2}E_0\cos\theta \quad \text{with} \quad J_1=1+\lambda_n a,\\
\left(\frac{\partial\delta n_n^+}{\partial r}\right)_{r=a} &= -C_n\frac{J_2}{a^3}E_0\cos\theta \quad \text{with} \quad J_2=2+2\lambda_n a+\lambda_n^2a^2.
\end{aligned} \tag{3.135}$$

The two first boundary conditions lead to:

$$\begin{aligned}
E_2 &= E_0\left(1-\beta\right),\\
\delta\rho^S(a) &= \left[\varepsilon_0\varepsilon_2\left(\beta-1\right)+\varepsilon_0\varepsilon_1\left(1+2\beta\right)\right]E_0\cos\theta.
\end{aligned} \tag{3.136}$$

Note that one can also evaluate $\delta\rho^S(a)$ from:

$$\begin{aligned}
\delta\rho^S(a) &= e\delta n_c^S(a)=\frac{e}{a^2}\int_a^\infty r^2\left[\delta n_c-\delta n_c^+\right]dr\\
&= \frac{-\varepsilon_0\varepsilon_1}{a^2}\int_a^{a+\kappa^{-1}}r^2\Delta\left(\delta\Psi-\delta\Psi^+\right)dr=\frac{-\varepsilon_0\varepsilon_1}{a^2}\int_a^{a+\kappa^{-1}}\frac{\partial}{\partial}\left(r^2\frac{\partial\left(\delta\Psi-\delta\Psi^+\right)}{\partial r}\right)dr\\
&= \varepsilon_0\varepsilon_1\left[\frac{\varepsilon_2}{\varepsilon_1}\left(\frac{\partial\delta\Psi_2}{\partial r}\right)_{r=a}-\left(\frac{\partial\delta\Psi^+}{\partial r}\right)_{r=a}\right]\\
&= -\varepsilon_0\varepsilon_2E_2\cos\theta+\varepsilon_0\varepsilon_1\left(1+2\beta\right)E_0\cos\theta=\left[\varepsilon_0\varepsilon_2\left(\beta-1\right)+\varepsilon_0\varepsilon_1\left(1+2\beta\right)\right]E_0\cos\theta.
\end{aligned}$$

In order to evaluate the third boundary condition one has to get:

$$J^{+}_{i,\perp}(a) = D\left[\frac{z_i e n_\infty}{kT}\left(1+2\beta\right) + \frac{J_2}{2a^3}C_n\right]E_0\cos\theta, \tag{3.137}$$

$$\begin{aligned}
\mathbf{J}^{S}_{i,\shortparallel}(a) &= \frac{-D}{a}\int_a^\infty r\left[n_{i,eq}-n^{+}_{i,eq}\right]dr\cdot\frac{1}{a}\frac{\partial}{\partial\theta}\left[\frac{z_i e}{kT}\delta\Psi^{+}(a)+\frac{\delta n^{+}_i(a)}{n_\infty}\right]\cdot\mathbf{e}_\theta \\
&= \frac{D}{a}\left[\frac{z_i e}{kT}\left(\beta-1\right)+\frac{J_1}{2n_\infty a^3}C_n\right]E_0\sin\theta\cdot\int_a^\infty r\left[n_{i,eq}-n^{+}_{i,eq}\right]dr\cdot\mathbf{e}_\theta, \\
\nabla\cdot\mathbf{J}^{S}_{i,\shortparallel}(a) &= \frac{1}{a\sin\theta}\frac{\partial}{\partial\theta}\left[\sin\theta J^{S}_{i,\shortparallel}(a)\right] \\
&= \frac{2D}{a^2}\left[\frac{z_i e}{kT}\left(\beta-1\right)+\frac{J_1}{2n_\infty a^3}C_n\right]E_0\cos\theta\cdot\int_a^\infty r\left[n_{i,eq}-n^{+}_{i,eq}\right]dr.
\end{aligned}$$

Writting the last boundary condition as a function of δn^S_n and δn^S_c, one gets:

$$\begin{aligned}
i\omega e\delta n^S_n(a) &= i\omega\left[e\delta n^S_+(a)+e\delta n^S_-(a)\right] = -\nabla\cdot\left[e\mathbf{J}^S_{+,\shortparallel}(a)+e\mathbf{J}^S_{-,\shortparallel}(a)\right]-\left[eJ^+_{-,\perp}(a)+eJ^+_{+,\perp}(a)\right], \\
i\omega e\delta n^S_c(a) &= i\omega\left[e\delta n^S_+(a)-e\delta n^S_-(a)\right] = -\nabla\cdot\left[e\mathbf{J}^S_{+,\shortparallel}(a)-e\mathbf{J}^S_{-,\shortparallel}(a)\right]-\left[eJ^+_{-,\perp}(a)-eJ^+_{+,\perp}(a)\right].
\end{aligned}$$

One gets:

$$\begin{aligned}
\left[eJ^+_{-,\perp}(a)+eJ^+_{+,\perp}(a)\right] &= eD\frac{J_2}{a^3}C_nE_0\cos\theta \\
&= \sigma_1 C_n\frac{J_2kT}{2en_\infty a^3}E_0\cos\theta,
\end{aligned} \tag{3.138}$$

$$\begin{aligned}
\left[eJ^+_{-,\perp}(a)-eJ^+_{+,\perp}(a)\right] &= D\frac{2e^2n_\infty}{kT}\left(1+2\beta\right)E_0\cos\theta \\
&= \varepsilon_0\varepsilon_1 D\kappa^2\left(1+2\beta\right)E_0\cos\theta \\
&= \sigma_1\left(1+2\beta\right)E_0\cos\theta
\end{aligned} \tag{3.139}$$

with

$$\begin{aligned}
\sigma^*_2 &= i\omega\varepsilon_0\varepsilon_2 \quad\text{and}\quad \sigma^*_1 = \sigma_1 + i\omega\varepsilon_0\varepsilon_1, \\
\sigma_1 &= \varepsilon_0\varepsilon_1\kappa^2 D.
\end{aligned} \tag{3.140}$$

One has also:

$$\begin{aligned}
-\nabla\cdot\left[e\mathbf{J}^S_{+,\shortparallel}(a)+e\mathbf{J}^S_{-,\shortparallel}(a)\right] &= \sigma_1\left[2\left(\beta-1\right)I_{c,eq}+\frac{J_1kT}{en_\infty a^3}C_nI_{n,eq}\right]E_0\cos\theta, \\
-\nabla\cdot\left[e\mathbf{J}^S_{+,\shortparallel}(a)-e\mathbf{J}^S_{-,\shortparallel}(a)\right] &= \sigma_1\left[2\left(\beta-1\right)I_{n,eq}+\frac{J_1kT}{en_\infty a^3}C_nI_{c,eq}\right]E_0\cos\theta,
\end{aligned}$$

where

$$\begin{aligned} I_{n,eq} &= \frac{-1}{2a^2 n_\infty}\int_a^\infty r\left[n_{n,eq}-n^+_{n,eq}\right]dr \\ &= \frac{-1}{a^2}\int_a^\infty r\left[\cosh(\frac{e\Psi_{eq}}{kT})-1\right]dr, \qquad (3.141) \\ I_{c,eq} &= \frac{-1}{2a^2 n_\infty}\int_a^\infty r\left[n_{c,eq}-n^+_{c,eq}\right]dr \\ &= \frac{1}{a^2}\int_a^\infty r\sinh\left(\frac{e\Psi_{eq}}{kT}\right)dr, \qquad (3.142) \end{aligned}$$

where one can use the fact that

$$\begin{aligned} \Psi^+_{eq} &= 0, \\ n^+_{c,eq} &= 0, \\ n^+_{n,eq} &= 2n_\infty. \qquad (3.143) \end{aligned}$$

$I_{c,eq}$ can be further evaluated:

$$\begin{aligned} I_{c,eq} &= \frac{-1}{2a^2 n_\infty}\int_a^\infty r\left[n_{c,eq}-n^+_{c,eq}\right]dr = \frac{\varepsilon_0\varepsilon_1}{2ea^2 n_\infty}\int_a^\infty r\Delta\left(\Psi_{eq}-\Psi^+_{eq}\right)dr \\ &= \frac{\varepsilon_0\varepsilon_1}{2a^2 n_\infty e}\int_a^\infty \frac{\partial^2}{\partial r^2}\left(r\Psi_{eq}\right)dr \\ &= \frac{-1}{(\kappa a)^2}\left[\frac{e\Psi_{eq}(a)}{kT}+a\left(\frac{\partial\left(e\Psi_{eq}/kT\right)}{\partial r}\right)_{r=a}\right]. \qquad (3.144) \end{aligned}$$

Finally, one gets:

$$\begin{aligned} i\omega e\delta n^S_n(a) &= i\omega\left[e\delta n^S_+(a)+e\delta n^S_-(a)\right] \\ &= K_1\left[2\left(\beta-1\right)I_{c,eq}+\frac{kT}{en_\infty a^3}C_n\left(J_1 I_{n,eq}-\frac{J_2}{2}\right)\right]E_0\cos\theta, \\ i\omega e\delta n^S_c(a) &= i\omega\left[e\delta n^S_+(a)-e\delta n^S_-(a)\right] \\ &= K_1\left[2\left(\beta-1\right)I_{n,eq}+\frac{kT}{en_\infty a^3}C_n J_1 I_{c,eq}-\left(1+2\beta\right)\right]E_0\cos\theta. \end{aligned}$$

One has 4 equations and 5 unknown: $C_n, E_2, \beta, \delta n^S_i(a)$ and one needs therefore a fifth equation. This equation is provided by the explicit form of $\delta n^S_i(a)$ in the low-zeta potential case [Chassagne and Bedeaux, 2008], and by a relation between the $\delta n^S_i(a)$ in the high potential case.
One assumes the relation between $\delta n^S_n(a)$ and $\delta n^S_c(a)$ be:

$$\delta n^S_n(a) = \gamma\delta n^S_c(a). \qquad (3.145)$$

From the two equations for $\delta\rho^S(a) = e\delta n^S_c(a)$ one finds:

$$\begin{aligned} i\omega\varepsilon_0\varepsilon_2\left(\beta-1\right)+i\omega\varepsilon_0\varepsilon_1\left(1+2\beta\right) &= \sigma_1\left[2\left(\beta-1\right)I_{n,eq}+\frac{kT}{en_\infty a^3}C_n J_1 I_{c,eq}-\left(1+2\beta\right)\right], \\ I_{c,eq}\sigma_1 J_1\frac{kT}{en_\infty a^3}C_n &= \beta\left(\sigma^*_2+2\sigma^*_1-2\sigma_1 I_{n,eq}\right)-\sigma^*_2+\sigma^*_1+2K_1 I_{n,eq}. \end{aligned}$$

From the relation between $\delta n_n^S(a)$ and $\delta n_c^S(a)$ one finds:

$$\frac{kT}{en_\infty a^3}C_n = \frac{2\beta\left(\gamma I_{n,eq} - I_{c,eq} - \gamma\right) - \gamma - 2\gamma I_{n,eq} + 2I_{c,eq}}{\left(I_{n,eq} - \gamma I_{c,eq}\right)J_1 - J_2/2}. \tag{3.146}$$

Inserting the value of C_n in eq.(3.146), one gets:

$$\begin{aligned}
&\beta\left[\sigma_2^* + 2\sigma_1^* - 2\sigma_1 I_{n,eq} + \sigma_1 J_1 I_{c,eq}\frac{4\left[I_{c,eq} - \gamma\left(I_{n,eq} - 1\right)\right]}{2J_1\left(I_{n,eq} - \gamma I_{c,eq}\right) - J_2}\right] \\
= &\left[\sigma_2^* - \sigma_1^* - 2\sigma_1 I_{n,eq} + \sigma_1 J_1 I_{c,eq}\frac{4\left[I_{c,eq} - \gamma\left(I_{n,eq} + 1/2\right)\right]}{2J_1\left(I_{n,eq} - \gamma I_{c,eq}\right) - J_2}\right].
\end{aligned} \tag{3.147}$$

In the semi-analytic approach that will be discuss below, the integrals $I_{c,eq}$ and $I_{n,eq}$ are evaluated numerically, having

$$\gamma = I_{n,eq}/I_{c,eq}.$$

For frequencies such as $\omega << D\kappa^2$ (which means that $\sigma_1^* \simeq \sigma_1$ and $\sigma_2^* \simeq 0(\sigma_1)$) the expression for β can be simplified into:

$$\beta = \frac{J_2 + 2I_{n,eq}\left(-J_1 + J_2\right) + 4J_1\left(I_{c,eq}^2 - I_{n,eq}^2\right)}{-2J_2 + 2I_{n,eq}\left(2J_1 + J_2\right) + 4J_1\left(I_{c,eq}^2 - I_{n,eq}^2\right)}. \tag{3.148}$$

For low zeta potentials, one can evaluate:

$$\begin{aligned}
I_{n,eq} &= 0 \quad \text{(therefore} \quad \gamma = 0\text{)} \\
I_{c,eq} &= \frac{1}{a^2}\int_a^\infty a\frac{e\zeta}{kT}\exp(-\kappa(r-a))\,dr \\
&= \frac{e\zeta}{kT}\left[\frac{\exp(-\kappa(r-a))}{-\kappa a}\right]_a^\infty \\
&= \frac{e\zeta}{kT}\frac{1}{\kappa a}.
\end{aligned} \tag{3.149}$$

One therefore obtains:

$$\beta = \frac{\sigma_2^* - \sigma_1^* - 4\left(J_1/J_2\right)\sigma_1\left(e\zeta/kT\right)^2/\left(\kappa a\right)^2}{\sigma_2^* + 2\sigma_1^* - 4\left(J_1/J_2\right)\sigma_1\left(e\zeta/kT\right)^2/\left(\kappa a\right)^2}, \tag{3.150}$$

$$C_n = a\frac{\varepsilon_0\varepsilon_1}{e}\kappa a\frac{e\zeta}{kT}\frac{2\left(\beta - 1\right)}{J_2}, \tag{3.151}$$

$$C_c = a\frac{\varepsilon_0\varepsilon_1}{e}\frac{\lambda_c a}{2 + \lambda_c a}\left(1 + 2\beta + \frac{\varepsilon_2}{\varepsilon_1}\left(\beta - 1\right)\right). \tag{3.152}$$

This is the expression for β is derived in Chassagne et al. [2003].

Note that

$$\beta = \frac{\sigma_2^* - \sigma_1^*}{\sigma_2^* + 2\sigma_1^*} \quad \text{and} \quad C_n = 0 \quad \text{if} \quad e\zeta/kT = 0. \tag{3.153}$$

For high zeta potentials, the assumption is made that the counterions dominate in the double layer, so one has:

$$\begin{aligned} I_{n,eq} &= -I_{c,eq} \quad \text{if} \quad \zeta > 0 \\ &= I_{c,eq} \quad \text{if} \quad \zeta < 0 \end{aligned}$$

The expression for the elektrokinetic surface charge density $(\partial\Psi_{eq}/\partial r)_{r=a}$ in terms of zeta potential has been tabulated and a good approximation for a symmetric electrolyte, valid for all zeta potentials and $\kappa a \gtrsim 0.5$ is:

$$\begin{aligned} I_{c,eq} &= \frac{-1}{(\kappa a)^2}\left[\frac{e\Psi_{eq}(a)}{kT} + a\left(\frac{\partial\left(e\Psi_{eq}/kT\right)}{\partial r}\right)_{r=a}\right], \\ &= \frac{-1}{(\kappa a)^2}\left[\frac{e\zeta}{kT} - \kappa a\left[2\sinh\left(\frac{e\zeta}{2kT}\right) + \frac{4}{\kappa a}\tanh\left(\frac{e\zeta}{4kT}\right)\right]\right]. \\ &\quad \text{(note that this formulation for } I_{c,eq} \text{ is also valid for low potentials)} \end{aligned}$$

This gives expression of β that is derived in Chassagne et al. [2003]

$$\beta = \frac{\sigma_2^* - \sigma_1^* + 2\sigma_1 q^*/(\kappa a)(1 - J_1/J_2)}{\sigma_2^* + 2\sigma_1^* + 2\sigma_1 q^*/(\kappa a)(1 + 2J_1/J_2)}, \tag{3.154}$$

$$q^* = 2\sinh\left(\frac{e|\zeta|}{2kT}\right) + \frac{4}{\kappa a}\tanh\left(\frac{e|\zeta|}{4kT}\right) - \frac{1}{\kappa a}\left(\frac{e|\zeta|}{kT}\right), \tag{3.155}$$

$$C_n = -a\frac{\varepsilon_0\varepsilon_1}{e}(\kappa a)^2\frac{2\beta + 1}{J_2}. \tag{3.156}$$

THE SCHWARTZ MODEL

Schwartz [Schwarz, 1962] was one of the first with O'Konski [O'Konski, 1960] to develop models for the polarization of colloids. Schwartz 's model is still widely used in the current models of the conductivity of granular material (e.g. Revil and Florsch [2010]). However the model of Schwartz, when applied to the polarization of a double layer, is by construction limited to frequencies such that $f \gg f_a$ where f_a is defined in the introduction. As discussed by Lyklema et al. [Lyklema et al., 1983], Schwartz attributed the double-layer polarization entirely to counterions bound to the spherical particle in a thin layer. Exchange between the bulk and the layer of surface conductivity was assumed to be absent. This explains why the contribution $\sigma_\perp^*$ which appears in Equation 3.24 is not apparent in the derivation of Schwartz. Without re-deriving the model found by Schwartz, it is here only shown where the differences between the full model (as found by numerical integration, and correctly reproduced by Equation 3.24) and the model of Schwartz arise. The derivation details can be found in Schwarz [1962] and Chassagne and Bedeaux [2008].

An alternating electric field $\mathbf{E}_{ext}$ of frequency ω is applied along the z-axis. Because of symmetry, spherical coordinates are chosen. The ionic density $\tilde{n}_k$ (number/m^3) of ion k and the electric potential $\tilde{\Psi}$ (V) can expressed as perturbation around their equilibrium values $n_{k,eq}$ and Ψ_{eq} (the equilibrium is defined as the situation when no electric field is applied):

$$\begin{aligned} \tilde{n}_k &= n_{k,eq} + \delta\tilde{n}_k \exp(i\omega t)\cos(\theta), \\ \tilde{\Psi} &= \Psi_{eq} + \delta\tilde{\Psi}\exp(i\omega t)\cos(\theta). \end{aligned} \tag{3.157}$$

To first order in the perturbation (neglecting the small products like $\delta\tilde{n}_k\delta\tilde{\Psi}$ terms) the ionic fluxes are given by

$$\tilde{\mathbf{J}}_k = -\frac{D_k n_{k,eq}}{kT}\nabla\left(kT\frac{\delta\tilde{n}_k\cos(\theta)}{n_{k,eq}} + z_k e\delta\tilde{\Psi}\cos(\theta)\right), \tag{3.158}$$

where D_k is the ionic diffusion of ion k and z_k its valence, e is the absolute value of the electron charge. The conservation equation yields:

$$\frac{\partial\tilde{n}_k}{\partial t} + \nabla\cdot\tilde{\mathbf{J}}_k = 0. \tag{3.159}$$

From Equations 3.158 and 3.159, one can obtain:

$$i\omega\delta\tilde{n}_k\cos(\theta) = D_k\nabla\cdot\left[n_{k,eq}\nabla\left(\frac{\delta\tilde{n}_k\cos(\theta)}{n_{k,eq}} + \frac{z_k e}{kT}\delta\tilde{\Psi}\cos(\theta)\right)\right]. \tag{3.160}$$

Each of the last two equations depends on the parallel (along r) and perpendicular (along θ) to the electric field direction:

$$\nabla = \nabla_r + \nabla_\theta. \tag{3.161}$$

In Schwartz' model there is no dependence of the variables on r implying that the term in ∇_r is zero. For distances close to $r = a$ one finds, for the ion k which represents the counterion:

$$\begin{aligned} i\omega\delta\tilde{n}_k\cos(\theta) &= D_k n_{k,eq}\nabla_\theta\cdot\left[\nabla_\theta\left(\frac{\delta\tilde{n}_k}{n_{k,eq}}\cos(\theta) + \frac{z_k e}{kT}\delta\tilde{\Psi}\cos(\theta)\right)\right] \\ &= \frac{D_k}{a^2}\frac{n_{k,eq}}{\sin(\theta)}\frac{\partial}{\partial\theta}\left[\sin(\theta)\frac{\partial}{\partial\theta}\left(\frac{\delta\tilde{n}_k}{n_{k,eq}}\cos(\theta) + \frac{z_k e}{kT}\delta\tilde{\Psi}\cos(\theta)\right)\right]. \end{aligned}$$

This last equation is Equation 15 in Schwarz [1962]. Re-arranging this equation leads to:

$$\left[\frac{i\omega a^2}{2D_k} + 1\right]\frac{\delta\tilde{n}_k}{n_{k,eq}} = -\frac{z_k e}{kT}\delta\tilde{\Psi}. \tag{3.162}$$

One can then define a characteristic time τ_k and frequency ω_k (similar to the frequency $\omega_a = 2\pi f_a$ defined in the introduction)

$$\omega_k = \frac{2D_k}{a^2} = \frac{1}{\tau_k}. \tag{3.163}$$

This is the time τ_k defined by Equation 50 in Leroy et al. [2008] and by Equation 21 in Lyklema et al. [1983]. Note, however, that Lyklema et al. [1983] (as it is done in this chapter) uses the bulk diffusion coefficient D_k whereas Leroy et al. [2008] introduces a "known Stern layer diffusion coefficient" (text under their Equation 50) as Leroy et al. [2008] that considers a particle with a polarizable Stern layer and no diffuse layer. In a later article by the same research group, see Revil and Florsch [2010], the authors state that "Surface conductivity corresponds to the electrical conduction in the electrical double layer coating the surface of the grains. Apparently, two contributions can therefore coexist. The first is the electrical conduction in the diffuse layer and the second is the electrical contribution of the Stern layer as described for instance in the dynamic Stern layer model of Zukoski and Saville [1986]. In fact the standard models for the polarization of a charged colloidal particle in an electrolyte usually only consider the polarization of the double layer, which leads to the surface conductivities $\sigma^*_\perp$ and $\sigma_{//}$ in Equation 3.24. The inclusion of the Stern layer conductivity can be done by adapting the boundary at the particle's surface Mangelsdorf and White [1997], Zukoski and Saville [1986], or by the analytical methods detailed in Appendix B. Here, the Schwartz model is applied to the polarization of the double layer only, and the Stern layer is not considered.

Equation 3.158 yields for the case considered by Schwartz:

$$\widetilde{J}_k = -\frac{D_k}{a}\left(\frac{\partial}{\partial\theta}\left[\delta\widetilde{n}_k\cos(\theta)\right] + \frac{z_k e}{kT} n_{k,eq}\frac{\partial}{\partial\theta}\left[\delta\widetilde{\Psi}\cos(\theta)\right]\right). \tag{3.164}$$

From Equation 3.162 one gets

$$\delta\widetilde{n}_k\cos(\theta) = \frac{-n_{k,eq}}{i\omega\tau_k+1}\frac{z_k e}{kT}\delta\widetilde{\Psi}\cos(\theta). \tag{3.165}$$

This equation is similar to Equation 49 in Leroy et al. [2008]. Combining Equations 3.164 and 3.165 one obtains:

$$\begin{aligned} e\widetilde{J}_k &= -\frac{z_k e^2 D_k}{kT} n_{k,eq}\left(\frac{i\omega\tau_k}{i\omega\tau_k+1}\right)\frac{1}{a}\frac{\partial}{\partial\theta}\left[\delta\widetilde{\Psi}\cos(\theta)\right] \\ &= \frac{z_k e^2 D_k}{kT} n_{k,eq}\left(\frac{i\omega\tau_k}{i\omega\tau_k+1}\right)\widetilde{E}_\theta. \end{aligned} \tag{3.166}$$

The electric field $\widetilde{E}_\theta$ is the local electric field in the vicinity of the particle due to the application of the electric field. It is from this last equation that most authors define their surface conductivity, see for example Equations 55 and 56 in Leroy et al. [2008]. Following these authors, a complex surface conductivity Σ^*_S is defined:

$$\begin{aligned} e\widetilde{J}_k &= \Sigma^*_S\widetilde{E}_\theta, \\ \Sigma^*_S &= \frac{z_k e^2 D_k}{kT} n_{k,eq}(a)\left(\frac{i\omega\tau_k}{i\omega\tau_k+1}\right). \end{aligned} \tag{3.167}$$

Contrary to the expression for the surface conductivity $\sigma_{//}$ that is given in Equation 3.25, Σ^*_S is a complex number and frequency-dependent. The reason is that Σ^*_S contains terms proportional to both $\sigma_{//}$ and $\sigma^*_\perp$. By accounting for both the parallel (along r) and perpendicular (along θ) component in Equation 3.160, it is possible to evaluate completely

the ionic fluxes. The full analytical derivation can be found in Chassagne and Bedeaux [2008]. The equivalence between Σ_S^* and $\sigma_{//}$ can however be made in the special case of frequencies such that $\omega \gg 1/\tau_k$. In that case the polarization of the double layer is mainly due to the movement of ions in the θ direction (parallel to the particle's surface) and there is nearly no influx of ions from the r direction perpendicular to the surface ($\sigma_\perp^* \simeq 0$) that would lead to an additional contribution in the parallel direction. Equation 3.167 gives for $\omega \gg 1/\tau_k$, assuming as in the previous section that $|z_k| = 1$ and $D_k = D$

$$\Sigma_S^* \rightarrow \frac{e^2 D}{kT} n_{k,eq}(a). \tag{3.168}$$

A relation between surface charge $q_{eq}(a)$ and zeta potential is given in Equation 3.83 of Appendix A. Using the fact that for an infinitely thin double layer, one has in good approximation $q_{eq}(a) \simeq e a n_{k,eq}(a)$ (where ion k represents the counterion) and one obtains:

$$n_{k,eq}(a) \simeq n_\infty \frac{2}{\kappa a} \exp\left(\frac{e\Psi_{eq}(a)}{2kT}\right). \tag{3.169}$$

As, by definition,

$$\sigma_e = \frac{2e^2 n_\infty D}{kT}, \tag{3.170}$$

it can be deduced that

$$\Sigma_S^* = \sigma_{//}/2 \quad (\text{for } \omega \gg 1/\tau_k). \tag{3.171}$$

The factor 2 appears because in Equation 3.167 only counterions were considered, and that by definition the ionic conductivity σ_e depends on both co- and counterions (hence the 2 in Equation 3.170). In the present appendix, the definition of $\sigma_{//}$ used by a large community of colloid scientists has been adopted, however, in Chassagne and Bedeaux [2008] a different definition was used, in which case Equation 3.171 would reduce to $\Sigma_S^* = \sigma_{//}$ (for $\omega \gg 1/\tau_k$).

4

DIELECTRIC SPECTROSCOPY OF SATURATED POROUS MEDIA: COMPENSATION FOR ELECTRODE POLARIZATION AND PSEUDO-INDUCTANCE EFFECT

There is no use of running fast
when you are on the wrong road...

Proverb

4-electrode setups are usually used to measure the dielectric response of sands and sandstones, as it is known that 2-electrode systems are sensitive to unwanted electrode polarization at low frequencies. Electrode polarization (EP) occurs in the frequency range where the characteristic relaxation associated to the grain size occurs.

Nonetheless, it is shown in this chapter that the parameters of interest for CO_2 storage monitoring (porosity, salinity) can easily be extracted from the frequency range 1 - 10 kHz, beyond the one affected by EP.

An additional unwanted effect ("pseudo-inductance") arises in the frequency range 10 kHz - 1 MHz. The origin of this effect is unknown. However, it is discussed that this phenomenon is not associated to any measurement error. The model we propose accounts for all three spectral regions with the pseudo-inductance as only adjustable parameter. In particular, we show that the bulk polarization region (which is the one of interest) can be modeled with no adjustable parameters.

The input parameters for the bulk polarization region are the porosity, the conductivity of the electrolyte, and the dielectric permittivities of the grains and of water. The model has been validated using laboratory measurements on a reservoir rock saturated with five different NaCl concentrations: 5 mM, 10 mM, 100 mM, 170 mM and 540 mM.

4.1. INTRODUCTION

Dielectric spectroscopy (DS) has been widely used during the last decades for environmental and engineering studies [Jougnot et al., 2010, Kemna et al., 2012, Revil et al., 2012, Slater and Glaser, 2003]. Numerous laboratory experiments have been conducted to investigate the frequency-dependence of electrical conductivity of porous rocks, e.g. unconsolidated sands [e.g., Ulrich and Slater, 2004] and sandstones [e.g., Binley et al., 2005, Knight, 1991]. Typically, DS laboratory measurements have been conducted on saturated rocks in the frequency range between 0.01 Hz and 3 MHz [e.g., Börner et al., 1996, Kavian et al., 2012, Slater and Glaser, 2003]. The DS response of a fluid-bearing reservoir rock is difficult to interpret quantitatively due to the interference of various polarization effects [Kemna et al., 2012]. These effects may overlap each other in the frequency domain [e.g., Leroy and Revil, 2009, Leroy et al., 2008].

Electrode polarization (EP) is the most common electrode/bulk effect reported in the literature for 2-electrode systems [e.g., Buck, 1969, Chassagne et al., 2016, Scheider, 1975]. This phenomenon occurs due to build-up of ions close to the surface of the measuring electrodes at low frequencies. Another low frequency polarization that is sometimes referred to in literature is called membrane polarization which is linked to the presence of overlapping double layers in pore throats [Marshall and Madden, 1959]. As the DS measurements presented in this work are done with a 2-electrode system, EP is dominant in the impedance spectra at low frequencies, and therefore, membrane polarization can not be observed.

At higher frequencies, different polarization effects have been reported. These effects are typically related to the polarization occurring in the vicinity of the sandstone grains and their double layers. At very high frequencies, the relaxation of the double layer can be observed [e.g., Garrouch and Sharma, 1994, Lesmes and Frye, 2001, Olhoeft, 1986]. These mechanistic models describe the overlapping of the polarization effects at low and high frequencies [e.g., Jougnot et al., 2010, Leroy and Revil, 2009, Okay et al., 2014]. These models have been successfully used to connect complex conductivity to the changes in the pore fluid chemistry [e.g., Lesmes and Frye, 2001, Schmutz et al., 2010, Vaudelet et al., 2011].

The interaction between the measuring equipment, electrodes and the sample can make interpretation of DS measurements even more challenging. For instance, the bulk impedance can be masked by electromagnetic pseudo-inductance effects which can produce inductive loops giving positive values in the phase spectra at high frequencies. These loops can be triggered by inductive wiring of the measurement system [MacDonald and Kenan, 1987] or the measurement system itself [Zimmermann et al., 2008]. Normally, this effect is taken into account during the design of a laboratory test facility to reduce its contribution.

This work is focused on DS of saturated sandstones in the frequency range 20 Hz - 3 MHz, where EP, bulk polarization and pseudo-inductance effect are most pronounced.

In this case, it is shown that the pseudo-inductance effect is not related to experimental errors, but rather to a property of the sandstone grains, most probably related to the Stern layer conductivity. In this chapter a full theoretical model for the frequency-dependent response of electrolyte and grains is presented. Each of the polarization effects (pseudo-inductance effect, EP and bulk polarization) is specifically described.

This chapter consists of four sections. In the first section a theoretical description of electrode polarization, bulk polarization, and pseudo-inductance complex conductivities is given as a function of the system parameters, i.e. porosity, conductivities and dielectric permittivities of water and grains. In the second section an equivalent circuit model is derived, for which the circuit elements can be identified with the complex conductivities found in the first section. An alternative circuit is also given based on traditional circuit elements. In the third section a short overview of the laboratory experimental setup which is used to measure the DS of NaCl solution in a saturated reservoir rock is given. Finally, in the fourth section a new model is applied to predict the desired bulk properties from measured DS of a fully saturated reservoir rock for 5 different NaCl solution concentrations.

4.2. ELECTRODE POLARIZATION

Electrode polarization (EP) is observed at low frequencies in the present 2-electrode measuring system. Typically, EP arises due to ion build-up close to the electrode surface. This effect is associated with a characteristic frequency ω_{ep} which is defined as [e.g., Buck, 1969, Chassagne et al., 2016, Hollingsworth and Saville, 2003]

$$\omega_{ep} \approx \frac{2D_0\kappa}{d}, \tag{4.1}$$

where d is the distance between the electrodes. It is verified that EP is indeed shifted to higher frequencies in these experiments in accordance with Equation 4.1, as the ionic strength is increased and/or d is diminished.

In this work C_s is in the range 5 - 540 mmol/l and two electrodes separations are used: d = 0.03 m and d = 0.074 m. The characteristic frequency for the EP effect is thus in the frequency range 20 - 200 Hz (from Equation 4.1). EP is often represented as a capacitor connected in series to the bulk impedance in an equivalent circuit approach [see Maruska and Stevens, 1988, Scheider, 1975]. In this research, the EP contribution has been derived from the set of electrokinetic equations presented in Buck [1969] and Chassagne et al. [2016]. The expression of EP for one phase systems, e.g. electrolytes, reads

$$\sigma^*_{ep}(\omega) = \frac{i\omega\varepsilon_{ep}\varepsilon_0\kappa d}{2}, \tag{4.2}$$

where ε_{ep} is the electrical permittivity of the phase. For electrolyte solutions (no porous media), $\varepsilon_{ep} = \varepsilon_e$. In the case of multiphase systems, such as suspensions or porous media, it remains to be investigated whether $\varepsilon_{ep} = \varepsilon_e$ or $\varepsilon_{ep} = \varepsilon_{bulk}$ [Chassagne et al., 2016].

4.3. PSEUDO-INDUCTANCE EFFECT

DS measurements show that the electrical impedance has a positive phase in the middle frequency range (10 kHz – 1 MHz). A positive phase is usually the signature of the

presence of inductors in electric circuits. Therefore, this effect is called as "pseudo-inductance". It has been observed that the characteristic frequency of this polarization depends on the electrode separation d. From a dimension point of view, one could argue that $\omega_L \sim D/(dl)$, where D is the characteristic ionic diffusion coefficient and l is the characteristic length. It is clear that $l \ll \kappa^{-1}$ since $\omega_L \gg \omega_{ep}$. In case the length l represents an actual length, it would be of the order of a Stern layer thickness. This is why a hypothesis is made that the pseudo-inductance effect arises from an additional conductivity layer around some of the grains (see Figure 4.1). The effect is localised close to the electrodes since it disappears at larger electrode distances. A more in-depth discussion about the pseudo-inductance is given in the following section.

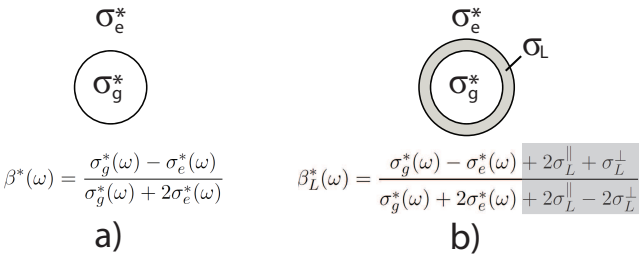

Figure 4.1: Dipolar coefficient for an uncharged grain (a) and a grain with conductive layer (b). The conductive layer conductivity σ_L can be decomposed into a parallel and perpendicular contributions ($\sigma_L^{\parallel}$ and $\sigma_L^{\perp}$).

Following Chassagne and Bedeaux [2008] but for a porous medium, a general formulation for the dipolar coefficient of a grain having an extra conductive layer, $\beta_L^*(\omega)$ can be as follows:

$$\beta_L^*(\omega) = \frac{\sigma_g^*(\omega) - \sigma_e^*(\omega) + 2\sigma_L^{\parallel} + \sigma_L^{\perp}}{\sigma_g^*(\omega) + 2\sigma_e^*(\omega) + 2\sigma_L^{\parallel} - 2\sigma_L^{\perp}}, \tag{4.3}$$

where $\sigma_L^{\perp}$ and $\sigma_L^{\parallel}$ are the perpendicular and parallel components of the extra conductive layer. The subscript L is given to this dipolar coefficient as it will be shown that it is the contribution that enables us to account for the pseudo-inductance effect. It is defined as

$$\sigma_L^{\parallel} = \alpha\sigma_e \qquad \text{and} \qquad \sigma_L^{\perp} = \mu\sigma_e, \tag{4.4}$$

where α and μ are real dimensionless coefficients. It has been found that it is possible to take $\sigma_L^{\perp} \approx \sigma_e$ in order to correctly fit the data, leaving α as the only adjustable parameter. Using Equation 4.3, the complex electrical conductivity corresponding to the response of grains with an extra conductive layer, $\sigma_L^*(\omega)$ reads:

$$\sigma_L^*(\omega) = \sigma_e^*(\omega)\,\frac{1 + 2(1-\phi)\beta_L^*(\omega)}{1 - (1-\phi)\beta_L^*(\omega)}. \tag{4.5}$$

4.4. FULL MODEL

Traditionally, DS measurements have been analyzed by means of equivalent electrical circuits. The classical equivalent circuit approach is based on the use of simple R, C, L

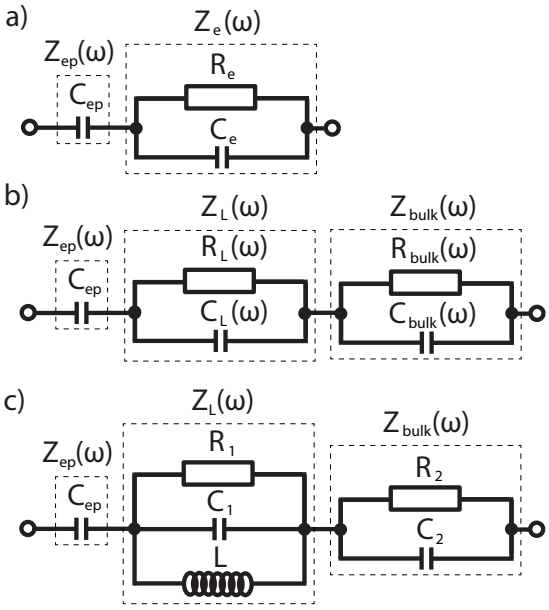

Figure 4.2: Equivalent circuit representation of the measured electrical impedance. $Z_{ep}(\omega)$, $Z_L(\omega)$ and $Z_{bulk}(\omega)$ are electrical impedances of electrode polarization, pseudo-inductance and bulk polarization, respectively. a) Equivalent circuit representation for an electrolyte solution. b) Pseudo-equivalent circuit representation with frequency-dependent R_L and C_L. c) Equivalent circuits representation with traditional R, C, L elements.

elements. It has been shown explicitly that composite systems can also be modeled by equivalent circuits, where each circuit element can be linked to a theoretical complex conductivity, as defined in the previous section [Chassagne et al., 2016].

For electrolyte solutions (with no porous media) in presence of EP, a similar equivalent circuit has been presented by Buck [1969]. In that case, assuming that electrodes are blocking, the equivalent circuit consists of a capacitor C_{ep} in series with a capacitor and a resistor which are in parallel (see Figure 4.2a). The following equivalence can be made:

$$C_{ep} = \frac{A\kappa\varepsilon_{ep}\varepsilon_0}{2}, \qquad C_e = \frac{A\varepsilon_e\varepsilon_0}{d} \qquad \text{and} \qquad R_e = \frac{d}{A\sigma_e}. \tag{4.6}$$

In the case of electrolyte solutions (no porous media), $\varepsilon_{ep} = \varepsilon_e$, see Equation 4.2. Note that all the circuit elements are frequency independent.

The same type of equivalence is considered when setting up the full model. The following constrains are imposed:

- Each polarization effect should be identifiable as a separate impedance in series with the others
- The equivalent circuit should account for the fact that:
    1. it should be valid for any porosity and ionic strength

2. the pseudo-inductance effect effect can or cannot be observed, depending on electrode separation.

These constrains led us to an equivalent circuit which is illustrated in Figure 4.2b. The total impedance of the system is represented by:

$$Z_{tot}(\omega) = Z_{bulk}(\omega) + \gamma Z_L(\omega) + Z_{ep}(\omega), \tag{4.7}$$

where $\gamma = 0$ for electrolyte solutions and $\gamma = 1$ for porous media.

The complex electrical conductivity of EP given in Equation 4.2, $\sigma^*_{ep}(\omega)$ and the related complex electrical impedance of EP, $Z_{ep}(\omega)$ are linked as

$$Z_{ep}(\omega) = \frac{1}{i\omega C_{ep}} = \frac{d}{A\sigma^*_{ep}(\omega)}, \tag{4.8}$$

where the capacitance of ideally polarizable planar electrodes is given by Equation 4.6.

In the case of $\phi = 1$, when only electrolyte is present, $Z_L = 0$ and $Z^*_{bulk} = d/(A\sigma^*_{bulk}(\omega))$, with $\sigma^*_{bulk}(\omega) = \sigma^*_e(\omega)$. In this case, $R_{bulk} = d/(A\sigma_e)$ and $C_{bulk} = A\varepsilon_0\varepsilon_e/d$, as found by Buck [1969].

The derivation of $\sigma^*_{bulk}(\omega)$ is discussed in details in the previous chapter and in Kirichek et al. [2017]. The following equivalence can be made:

$$R_{bulk}(\omega) = \frac{d}{\Re\left(\sigma^*_{bulk}(\omega)\right) A} \qquad \text{and} \qquad C_{bulk}(\omega) = \frac{\Im\left(\sigma^*_{bulk}(\omega)\right) A}{\omega d}, \tag{4.9}$$

where

$$\sigma^*_{bulk}(\omega) = \sigma^*_e(\omega)\,\frac{1 + 2(1-\phi)\beta^*(\omega)}{1 - (1-\phi)\beta^*(\omega)}, \tag{4.10}$$

and

$$\beta^*(\omega) = \frac{\sigma^*_g(\omega) - \sigma^*_e(\omega)}{\sigma^*_g(\omega) + 2\sigma^*_e(\omega)}. \tag{4.11}$$

Equations 4.9 implies that the circuit elements are now frequency dependent. The equivalent circuit analogy is, however, still possible [Chassagne et al., 2016]. Despite having the dimension of resistance and capacitance, $R_{bulk}(\omega)$ and $C_{bulk}(\omega)$ are not standard resistor and capacitor (as they are frequency-dependent), but they can be seen as elements similar to Warburg elements which are also frequency-dependent.

The pseudo-inductance effect is represented by the impedance $Z_L(\omega) = d/(A\sigma^*_L(\omega))$, where $\sigma^*_L(\omega)$ is given in Equation 4.5 and α is the only adjustable parameter, as discussed under Equation 4.4.

One adjustable parameter, α, therefore appears in the model. Note, that in the region of spectrum where bulk polarization dominates (1-10 kHz), $Z_{tot}(\omega) \sim Z_{bulk}(\omega)$. This implies that behaviour of the bulk polarization can be predicted with no adjustable parameter as it is commonly done [e.g., Garrouch and Sharma, 1994, Lesmes and Frye, 2001, Olhoeft, 1986].

For comparison, an alternative model is considered, still based on Equation 4.7, but where the impedances are given in terms of traditional equivalent elements:

$$Z_{ep}(\omega) = \frac{1}{i\omega C_{ep}}, \qquad \frac{1}{Z_L(\omega)} = \frac{1}{R_1} + i\omega C_1 + \frac{1}{i\omega L}, \qquad \text{and} \qquad \frac{1}{Z_{bulk}(\omega)} = \frac{1}{R_2} + i\omega C_2. \tag{4.12}$$

In this case, R_1, C_1, R_2, C_2 and L are the adjustable parameters and $Z_{tot}(\omega) = Z_{ep}(\omega) + Z_{bulk}(\omega) + Z_L(\omega)$.

4.5. LABORATORY EXPERIMENTS

A simplified sketch of the experimental setup is shown in Figure 4.3. Bentheimer sandstone is used as a core material. The relatively high porosity and permeability of Bentheimer sandstone makes it a good testing material for core-flood experiments. The sample is encased in a silicone sleeve and placed in a stainless steel core holder. The ductility of the sleeve allows a confining overburden pressure to be transferred to the core to simulate reservoir pressure. An insulating silicon rubber is used as a material for the sleeve. Thus, current leakages from the system to the core holder can be disregarded. The core, mounted within the sleeve is placed inside a core holder which is capable of simulating reservoir pressures of up to 600 bar. The core holder has a vertical orientation that allows minimizing the gravitational instabilities during the injections. A temperature controlled oven is used to reproduce realistic reservoir conditions of temperature and to eliminate complication of data analysis due to fluctuations in the external temperature.

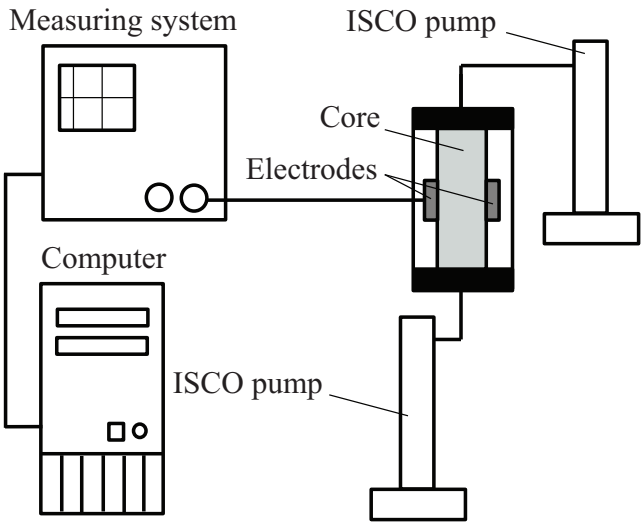

Figure 4.3: Scheme of the experimental setup

Each end of the core holder contains a port for fluid injection. Two ISCO syringe pumps are used for fluids injection into the core. One of the pumps is filled with NaCl solution and the other one is used for fluid collection from the sample. All ISCO pumps

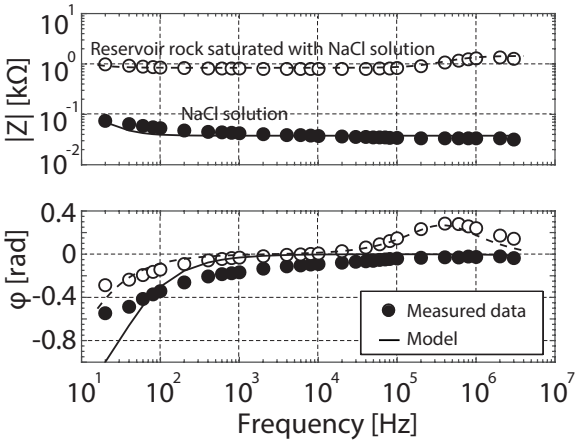

Figure 4.4: Magnitude $|Z|$ and phase φ spectra of complex electrical impedance. Hollow circles show the impedance measurements of the reservoir rock, which is saturated with 170 mmol/l NaCl solution. Black circles show the impedance of the 170 mmol/l NaCl solution. Solid and dashed lines represent models given in Figure 4.2a and 4.2b, respectively. No adjustable parameters are required in both cases for the region representing bulk polarization (between 1 kHz and 20 kHz).

provide a very smooth displacement which eliminates pressure shocks to the core material. The pumps are capable of injecting at rates of 1 ml/min at pressures up to 250 bar with an accuracy of 0.01 ml.

A Wayne Kerr Precision Component Analyzer 6640A is used as a measuring system. Coaxial cables connect the measuring device to the electrodes, which are directly attached to the lateral surface of the core on diametrically opposite sides. We use a 2-terminal electrode system in this study. Both electrodes act as current and potential terminals. The electrical properties of specimens are determined by measuring the potential difference between the electrodes and the applied current across them. The measurements of magnitude $|Z|$ and phase φ of the electrical impedance are conducted over the frequency range 20 Hz - 3 MHz. The electrical conductivity $\sigma^*(\omega)$ is converted from the measured $|Z|$ and φ as

$$\sigma^*(\omega) = \frac{d}{A|Z|e^{i\varphi}}. \tag{4.13}$$

Two sets of experiments are conducted. For the first set a NaCl solution with C_s = 5, 10, 100, 170 and 540 mmol/l is used. Dimensions of the sample are as follows: d =0.03 m and A =0.01×0.05 m^2. For the second set of experiments a NaCl solutions with C_s = 5 and 100 mmol/l are used. For this case, the dimensions are d =0.074 m and A =0.01×0.02 m^2.

4.6. RESULTS AND DISCUSSION

The DS response of the reservoir rock with NaCl solutions of various salinities, as measured in the laboratory, is shown in Figure 4.5. The measured $|Z|$ and φ are compared with estimated complex impedance following Equation 4.7. Each factor that contributes

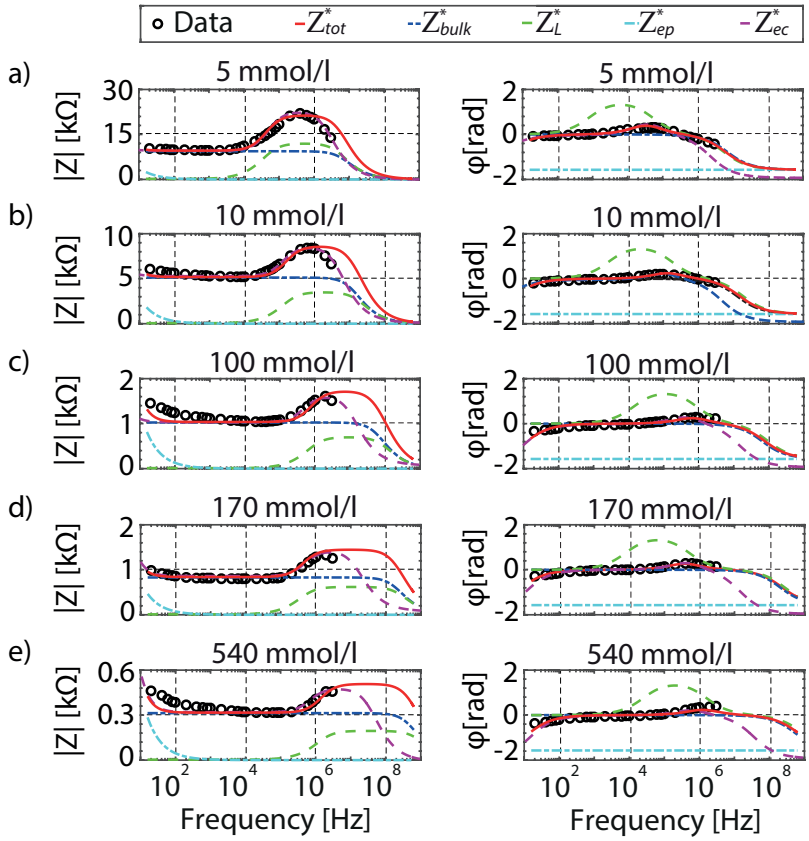

Figure 4.5: Individual contributions of EP (light blue line), pseudo-inductance (green dashed line) and bulk polarization (dark blue dashed line) to the total impedance (red solid line) of a fully saturated reservoir rock. The model for the impedance is given in Figure 4.2b. No adjustable parameter is used to generate the bulk impedance. The dashed magenta line represents the fitting according to the model presented in Figure 4.2c. Measured impedances are shown in symbols for NaCl concentrations of 5, 10, 100, 170 and 540 mmol/l. Electrode separation is 0.03 m.

to the total impedance is shown separately in Figure 4.5. From these contributions it is clear that a frequency region can be identified where the contribution of the bulk polarization (desired) is dominant. For the system in Figure 4.2b, this is between $\omega_{ep} \sim 10^3$ Hz and $\omega_L \sim 10^5$ Hz. The characteristic frequency of EP, ω_{ep} is increasing with salinity in accordance with Equation 4.1. The frequency ω_L associated with the pseudo-inductance effect is also increasing with salinity until 100 mmol/l, when the full saturation is reached. The parameters used to fit the data are given in Table 4.1. The measured impedance could be fitted either using the equivalent circuit given in Figure 4.2b and R_1, C_1, R_2, C_2, L as adjustable parameters or using the equivalent circuit given in Figure 4.2c with α as the only adjustable parameter, given in Table 4.1.

The fact that φ becomes positive in the frequency range around 100 kHz indicates the development of an inductive effect in the system. There are several possible ex-

Table 4.1: Values of $\alpha = \sigma_L^{||}/\sigma_e$ used in the modeling as shown in Figure 4.2b. See text for details.

Dimensions	5 mmol/l	10 mmol/l	100 mmol/l	170 mmol/l	540 mmol/l
α(d=0.03m)	10^{-3}	10^{-3}	10^{-3}	10^{-3}	10^{-4}
α(d=0.074m)	10^{-4}	10^{-4}	10^{-4}		

planations of the origin of this phenomenon. Inductive loops can be generated by a chemical reaction between electrode and electrolyte, e.g. oxidation of the electrodes [MacDonald and Kenan, 1987]. Component analysis of the electrolyte used in current experiments has been conducted to discard this hypothesis. No traces of chemical reaction is found. Another trigger for inductive loops can be due to inductive connecting cables [Lvovich, 2012]. In this case pseudo-inductance signatures occur at high frequencies in the impedance spectrum. The evidence of parasitic inductance in coaxial cables used here has also been checked but none is detected. Fleig et al. [1996] suggests that inductive loops can be induced in the impedance spectra at high frequencies due to the capacitive leakage to the ground. Since the measurement system used in this study is grounded, the occurrence of this artifact is highly unlikely.

To model the DS Fleig et al. [1996] use an equivalent circuit with no inductance. They propose to use instead of one, two RC (with R and C that are not frequency dependent) equivalent circuits: one for the $\Re(\sigma^*_{tot})$ and the other for $\Im(\sigma^*_{tot})$. Therefore, they have 4 adjustable parameters. Neither this model [Fleig et al., 1996] nor the alternative one shown in Figure 4.2c can be related in a way to the reservoir rock properties.

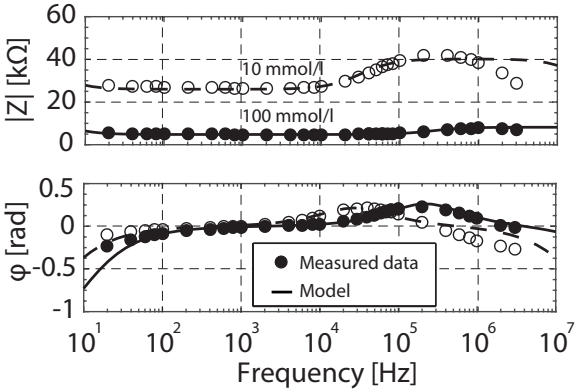

Figure 4.6: Validation of the model for d = 0.074 m. Measured impedances are shown in symbols for NaCl concentration of 10 mmol/l and 100 mmol/l. The full model is shown by the solid line.

Some other authors also found pseudo-inductance effects in their measurements [e.g., Abdulsamad et al., 2016, Fleig et al., 1996, Ward, 1990, Zimmermann et al., 2008]. All these authors found this pseudo-inductance for an electrolyte solution and not for a porous medium. Zimmermann et al. [2008], referring to the phenomenon as "contact impedance", used a 4-electrode measuring system and attributed the phenomenon to a phase error due to the inhomogeneous contact impedance of the current electrodes.

It is observed that this phenomenon is most striking when stainless steel electrodes are used for the current electrodes [e.g., Abdulsamad et al., 2016, Zimmermann et al., 2008]. In this study stainless steel electrodes are also employed, and therefore, it has been checked whether this pseudo-inductance phenomenon arises also in the measurements under similar conditions (electrolyte alone). Figure 4.4 shows the impedance measurements which are carried out on 170 mmol/l NaCl solution. For comparison, the impedance response of a reservoir rock that is saturated with the same solution is analysed. No pseudo-inductance is observed when only electrolyte is measured, yielding $\gamma(\phi = 1) = 0$. Hence, the observed pseudo-inductance arises from an effect in the porous media. This is accounted for in the full model by means of an extra conductive layer around some of the grains that polarizes due to specific interactions between these semi-conducting grains and the electrolyte ions in the proximity of the electrodes. This conductive layer includes in particular the contribution of the Stern layer. Due to EP, there is an accumulation of ions in the vicinity of the electrodes, which could lead to an increased effect of the conduction at the surface of the grains in their vicinity. From Table 4.1, it can be noted that $\sigma_L^{||}$ is increasing with ionic strength in the same way as σ_e does, since α is a constant for all $Cs < 540$ mmol/l. For salt concentrations as high as 540 mmol/l, the predicted electrical conductivity σ_e is about 25% higher than the measured one in accordance with previous theoretical and experimental findings [Bernard et al., 1992]. This might explain why the value of α is lower for 540 mmol/l than for all other considered salt concentrations. It is found that α is decreasing with increasing electrode separation (see Table 4.1), which results in shifting ω_L to lower frequencies.

Whatever may be the validity of the physical interpretation of the theoretical model, what is demonstrated here is that based on the model developed in this research, each factor contributing to the polarization can correctly be separated. In particular, it is found that the bulk contribution of ω_{ep} and ω_L is indeed represented by $Z_{bulk}(\omega)$, where the inputs for calculating $Z_{bulk}(\omega)$ are ε_g, σ_e, ε_e and ϕ, that are well known. No adjustable parameters are used.

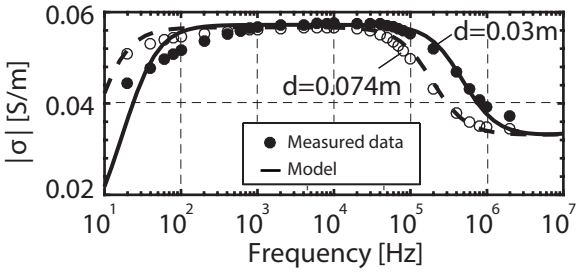

Figure 4.7: Electrical conductivity spectrum of the porous rock saturated with 100 mmol/l NaCl solution for electrode separation of 0.074m and 0.03m. Symbols and lines represent the measured data and the corresponding model, respectively.

Comparison between Figures 4.5 and 4.6 shows that the frequency related to the pseudo-inductance effect is decreasing with increasing electrode separation. This is illustrated in Figure 4.7.

From Equations 4.3, 4.5, 4.7, 4.10 and 4.11, one finds that with $\omega \ll \omega_L$, $\beta_L^*(\omega) \rightarrow 1$ and

$\beta^*_{bulk}(\omega) \rightarrow$-0.5, therefore $Z_L(\omega) \ll Z_{bulk}(\omega)$. The pseudo-inductance effect disappears for frequencies lower than ω_L. For $\omega < \omega_L$, one has therefore $Z_{tot}(\omega) = Z_{ep}(\omega) + Z_{bulk}(\omega)$ and no adjustable parameters are required to fit the measured impedance. EP dominates in the frequency range around ω_{ep}, as EP can be seen as a parallel impedance to the bulk impedance.

In Chassagne et al. [2016], the question was raised whether, in estimating C_{ep}, one should take $\varepsilon_{ep} = C_{ep}/(A\kappa\varepsilon_0) = \varepsilon_e \approx 78.8$ or ε_{bulk}. It is found that $\varepsilon_{ep} \simeq \varepsilon_{bulk}$ in the whole range of the considered salinity, where ε_{bulk} is defined as

$$\varepsilon_{bulk} = Im\left(\frac{\sigma^*_{bulk}(\omega)}{\varepsilon_0\omega}\right). \tag{4.14}$$

This result leads us to the conclusion that the grains certainly contribute to ε_{ep}.

4.7. CONCLUSION

It is shown that the Dielectric spectroscopy response of a porous sandstone saturated with NaCl solutions of different concentrations can correctly be modeled using a new protocol presented in this chapter. The model accounts for 3 distinct polarization phenomena: electrode polarization (EP), bulk polarization, and pseudo-inductance effect.

For EP, the question was raised in Chassagne et al. [2016] whether $\varepsilon_{ep} = \varepsilon_e$ or $\varepsilon_{ep} = \varepsilon_{bulk}$ in the evaluation of C_{ep}, see Equation 4.6. The EP response is correctly predicted in this case using $\varepsilon_{ep} = \varepsilon_{bulk}$ for all investigated concentrations.

The pseudo-inductance effect can also be accounted for using only one adjustable parameter. The characteristic frequency ω_L is attributed to the pseudo-inductance effect.

In the frequency range ω_{ep} - ω_L, the contribution of bulk polarization is dominant. With no adjustable parameters, the bulk response of the sandstone can be predicted.

5

QUANTITATIVE CO_2 STORAGE RESERVOIR MONITORING FROM MODELLING COMPLEX ELECTRICAL CONDUCTIVITY INCLUDING OVERLAPPING POLARIZATION EFFECTS

To be defeated and not submit, is victory;
to be victorious and rest on one's laurels, is defeat.

Jozef Pilsudski

Dielectric spectroscopy (DS) has been performed on a Bentheimer sandstone, which is saturated with either CO_2 or saline water. The DS response is captured using two types of multi-electrode arrays. The experiments have all been performed under realistic reservoir pressure and temperature conditions ($P \approx 80$ bar, $T \approx 43^{\circ}$C) of a sequestrated CO_2 reservoir. Both the magnitude and the phase of the complex electrical conductivity show a high sensitivity to the CO_2 injection in the pore spaces.

A model developed in Chapter 3, which provides a description of the electrical conductivity as a function of frequency, electrolyte concentration, porosity and temperature, is adapted for the present measurements by including a saturation coefficient as defined in Archie's law to evaluate the CO_2 saturations of the cores. In particular, this model accounts for both the bulk polarization response (located in the frequency range where other polarization effects are negligible) and the pseudo-inductance effect located at higher frequencies. This

pseudo-inductance effect is analyzed in Chapter 4. It is shown that it is possible to find a unique set of parameters (electrolyte concentration and water saturation) when fitting the impedance spectrum of a reservoir rock saturated with a fluid of unknown salinity and saturation. The only requirement is that the porosity and the surface conductivity of a grain introduced in this model are known. These can be easily obtained by predicting the impedance spectrum of the reservoir rock saturated with a known electrolyte at full saturation.

5.1. INTRODUCTION

In the recent decades, the carbon capture and storage (CCS) has been considered as one of the means to reduce the level of greenhouse gases in the atmosphere. To ensure a full compliance with health, safety and environment standards during the CO_2 injection and permanent CO_2 storage, reliable tools and technologies need to be developed for monitoring the CO_2 migration in deep storage reservoirs. These methods should in particular enable quantifying the actual amount of CO_2 stored in the reservoir. Time-lapse direct current (DC) resistivity tomography [Schmidt-Hattenberger et al., 2015] can reliably trace the CO_2 plume migration since the electrical properties of a porous medium are strongly controlled by the ionic characteristics of the fluids that fill the pore space. A number of studies has shown the potential of this method for CO_2 storage monitoring [e.g., Börner et al., 2013, 2015, Christensen et al., 2006]. For instance, at the Ketzin test site in Germany, the feasibility of monitoring the CO_2 migration is investigated [Bergmann et al., 2012, Schmidt-Hattenberger et al., 2011] by injecting CO_2 in a saline aquifer. The monitoring is conducted by means of cross-hole and surface-to-downhole electrical resistivity tomography (ERT). The outcome of this study demonstrates the applicability of ERT to monitor the CO_2 storage in deep saline aquifers and possible CO_2 leakages in shallow ground waters. However, DC measurements can provide erroneous bulk conductivity estimates due to electrode polarisation and heating effects [Binley et al., 2005]. Unlike DC methods, alternating current (AC) methods enable assessing both the magnitude of the impedance (from which DC conductivity can be derived) and the phase lag between electric field and current as a function of frequency. Frequency-dependent electrical methods have been widely used during last decades [e.g., Revil et al., 2012] for measurements in oil-bearing rocks [Olhoeft, 1986, Vinegar and Waxman, 1984] and in a few occasions for geological CO_2 storage monitoring [e.g., Kremer et al., 2016]. Geochemical changes in a shallow aquifer induced by CO_2 leakage from deeper geological storage rock have also been monitored using time-domain electrical methods [Doetsch et al., 2015].

Numerous field and laboratory experiments have been conducted to investigate the frequency-dependence of the electrical properties of porous media such as unconsolidated sands [e.g., Shahidi et al., 1975, Ulrich and Slater, 2004] and sandstones [e.g., Binley et al., 2005, Knight, 1991] saturated with electrolytes at ambient conditions.

The DS measurement of a fluid-bearing reservoir rock is however difficult to interpret quantitatively due to the overlapping of various polarization mechanisms in the frequency domain [Kemna et al., 2012]. Different models have been developed [e.g., Cosenza et al., 2008, Jougnot et al., 2010] and successfully applied to connect the frequency-dependent conductivity to changes in the pore fluid chemistry [e.g., Lesmes and Frye,

2001, Vaudelet et al., 2011] and to detect the presence of fluid in the pore spaces in sands [Schmutz et al., 2010].

In Chapter 3, analytical models are introduced for the electrokinetic response of a fully saturated rock. Chapter 4 introduces a method for extracting a bulk polarization from measured impedance that is affected by the low-frequency phenomenon called "electrode polarization" and a high frequency phenomenon defined as "pseudo-inductance". It has been demonstrated that the model could be used to predict the bulk response which is partially masked by electrode and pseudo-inductance polarizations with no adjustable parameters. The pseudo-inductance polarization contribution can be fitted to the data using one adjustable parameter. This parameter is linked to the surface conductivity of a grain. Building on the work done in Chapter 3, it is demonstrated in this chapter that the model can be adapted and used for the prediction of the partial saturation of saline water in the reservoir rock. The two relevant parameters (electrolyte concentration and water saturation) can be obtained from fitting the data using the extended model, following the protocol described in this chapter.

The chapter is structured as follows. In the first section, the newly-built laboratory experimental setup and calibration techniques are presented, concentrating on Dielectric spectroscopy measurements of brine- and CO_2-bearing reservoir rock. In the next section, the theoretical model is introduced and adapted for partially saturated porous media. Using this model, the DS data acquired during pressure-temperature controlled CO_2 injection into a saline-water-saturated sample of a Bentheimer sandstone is analysed in Section 5.4, for 5 different NaCl concentrations. The conclusions are presented in Section 5.5.

5.2. LABORATORY EXPERIMENTS

In this study two different geometries of the core sample are used to detect the fluid front propagation. A cylindrical core with three electrode pairs is further referred as core A. The lower part of the sample presented in Chapter 2 with four electrode pairs (see Figure 2.2) is defined as core B. A simplified sketch of both geometries of the core is provided in Figure 5.1.

In order to achieve the supercritical state of the CO_2, the experiments are performed on the sandstone core at confining pressure of 85-87 bar, a pore pressure of 77-83 bar, and 41-45°C temperature, which represent in-situ CCS reservoir conditions. The saline water, as the denser phase, is injected from the bottom of the core to avoid gravitational instability. A pump, maintained using the flow rate at a constant value of 1 ml/min, is used to ensure a homogeneous distribution of saline water over the entire length of the core. The CO_2 is injected by another syringe pump from the top end of the core.

The cell constant of the core F, to which planar electrodes are attached, is given by $F = A/d$, where A is the cross-sectional area of one electrode and d is the distance between the electrodes. Because the core A has arcuate-shaped electrodes attached to it, its cell constant has to be evaluated. In order to find this cell constant, tests on materials with known electrical properties (distilled water and air) have been conducted. The electrodes are glued inside a cylindrical container of same dimensions as core A with the same type of arcuate-shaped electrodes. Figure 5.2 depicts measured and theoretical values of electrical amplitude and phase for distilled water and air as a function

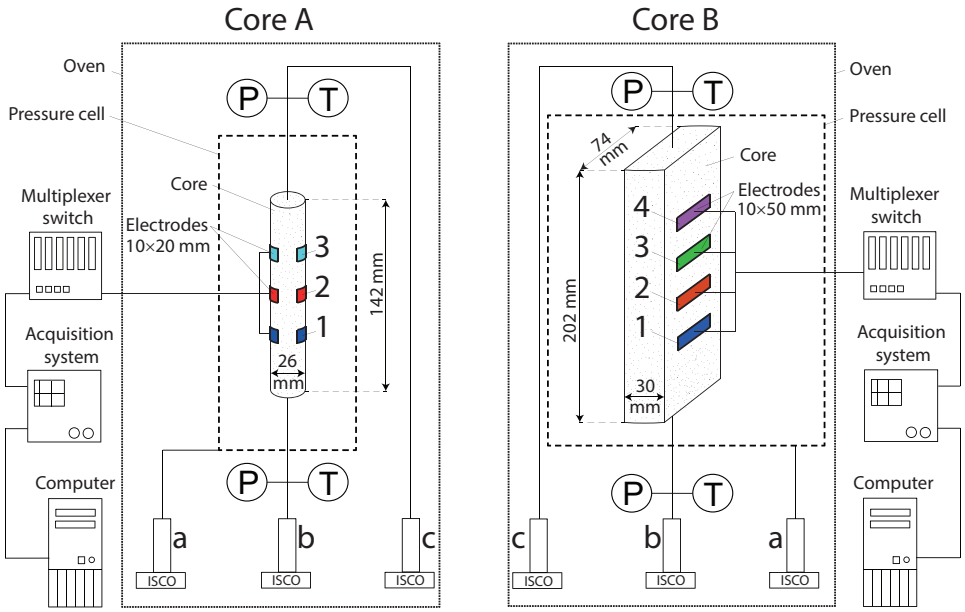

Figure 5.1: Scheme of the experimental setup. The ISCO pumps a, b and c are used for infecting of the NaCl solution, CO_2 flooding and confining pressure control, respectively. The numbers 1–3 and 1–4 indicate the electrode pairs, located at different length-positions of each core.

of frequency using the container setup. These systems are chosen as neither electrode polarization nor pseudo-inductance effect affects the measurements, and the dielectric permittivity of water and air are well-known (see Table 5.1). The total impedance of these systems can be modeled by a simple parallel RC equivalent circuit:

$$\frac{1}{Z_{tot}(\omega)} = \frac{1}{R} + i\omega C \quad \text{with} \quad R = \frac{1}{F\sigma} \quad \text{and} \quad C = F\varepsilon_0\varepsilon_r, \tag{5.1}$$

where R is the resistance, C is the capacitance, i is the imaginary unit, ω is the angular frequency, $F = A/d$ is the formation factor, d is the distance between the electrodes, A is the cross-sectional area of one electrode, σ is the DC electrical conductivity, ε_0 is the electric constant, and ε_r is the relative permittivity.

Table 5.1: Parameters used for the model-fit displayed in Figure 5.2

	σ (mS/m)	ε_r (-)	A (m)	d (m)	C (pF)	R $(k\Omega)$
Distilled water	0.2	80	$2{\cdot}10^{-4}{\pm}10^{-6}$	0.01±0.001	0.14	250
Air	$3{\cdot}10^{-12}$	1	$2{\cdot}10^{-4}{\pm}10^{-6}$	0.01±0.001	18	$17{\cdot}10^{9}$

As shown in Figure 5.2, the measured and modeled values are in a good agreement for the whole frequency range provided that the cell constant for core A is taken to be $F = 0.02 \pm 0.001$ m. This value is obtained using F as the only adjustable parameter in

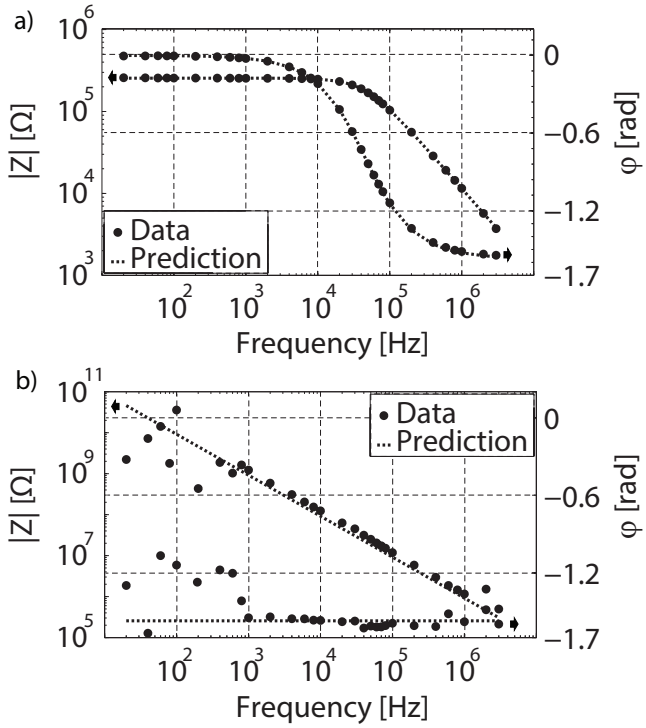

Figure 5.2: Magnitude and phase spectra of complex electrical impedance for (a) distilled water and (b) air. The measurements are performed using a container of same dimensions as the core A. The corresponding values for R and C are to be found in Table 5.1

the fit of C using ε_r given in Table 5.1. σ is then obtained using R and the found value of F. The area of the electrode A can be estimated from the electrode dimensions (see Table 5.1), and therefore, a characteristic length d can be estimated from F using $d = A/F$. It is found that d corresponds to the distance between the centers of mass of two electrodes in an electrode pair.

5.3. MODEL

The Maxwell-Wagner model, presented in Chapter 3, is extended by incorporating a saturation term, S_w^n, in the definition of the conductivity. In Chapter 4, it is shown that the total impedance of a system $Z_{tot}(\omega)$ consisting of a porous medium, which is fully saturated with an electrolyte solution, can be modeled as:

$$Z_{tot}(\omega) = Z_{bulk}(\omega) + \gamma Z_L(\omega) + Z_{ep}(\omega), \tag{5.2}$$

where $Z_{bulk}(\omega)$, $Z_L(\omega)$ and $Z_{ep}(\omega)$ are the impedances of the bulk, pseudo-inductance and electrode polarization, respectively. ω is the angular frequency, γ =1 when a porous media is present and $\gamma = 0$ for a pure electrolyte system. In the case of one phase system (for instance the case where an electrolyte solution is investigated in the absence of

porous media), Equation 5.2 becomes

$$Z_{tot}(\omega) = Z_{bulk}(\omega) + Z_{ep}(\omega) \quad \text{with} \quad Z_{bulk}(\omega) = \frac{d}{A\sigma_e^*(\omega)}. \tag{5.3}$$

If EP is not important ($Z_{ep}(\omega) \ll Z_{bulk}(\omega)$), one finds again Equation 5.1. An expression for Z_{ep} is given in Chapter 4. EP only acts at low frequencies, and it can be neglected in the prediction of the desired bulk properties, i.e. the salinity and saturation. Therefore, EP is not discussed in the present chapter.

The bulk impedance $Z_{bulk}(\omega) = d/(A\sigma^*_{bulk}(\omega))$ is associated to the complex conductivity of the bulk, $\sigma^*_{bulk}(\omega)$, given by:

$$\sigma^*_{bulk}(\omega) = \sigma^*_e(\omega)\,\frac{1+2(1-\phi)\beta^*(\omega)}{1-(1-\phi)\beta^*(\omega)}, \tag{5.4}$$

where ϕ is porosity, $\beta^*(\omega)$ is the dipolar coefficient associated to the grains and $\sigma^*_e(\omega) = \sigma_e(\omega) + i\omega\varepsilon_0\varepsilon_e$ is the complex electrical conductivity of the electrolyte with ε_e being the permittivity of the electrolyte. The conductivity of the electrolyte $\sigma_e(\omega)$ reads:

$$\sigma_e = \frac{\sum_i \nu_i z_i^2 D_i e^2 N_a}{k_b T} C_s = \varepsilon_0\varepsilon_e\kappa^2 D_0, \tag{5.5}$$

where e is the elementary charge, C_s is the salt concentration of the solution given in mM, D_i is the diffusion coefficient of ion i, k_b is the Boltzmann constant, T is the temperature, z_i is the valence of ion i, ν_i is the stoichiometric coefficient, N_a is the Avogadro constant and κ is the inverse Debye length. D_0 has the dimension of a diffusion coefficient and is given by:

$$D_0 = \frac{z_+ D_+ - z_- D_-}{z_+ - z_-}, \tag{5.6}$$

where the electro-neutrality relation $\sum_i \nu_i z_i = 0$ is used. In this work NaCl solution is used as a pore-filling electrolyte. Hence, the following is assumed: $D_+ \approx D_- \approx 2{\cdot}10^{-9}$ m^2/s, $z_+ = -z_-$ and $\nu_+ = \nu- = 1$.

The presence of two miscible fluids in the pore space of a porous material is common in CO_2 sequestration. In particular, the original pore-filling fluid acts as an electrolyte, while the injected supercritical CO_2 has insulating electrical properties. The most commonly used equation for describing the variation of electric conductivity with electrolyte saturation S_w, was introduced by Archie [1942]. This classical equation describes the electric conductivity to be proportional to S_w^n, where n is referred to as the saturation exponent. It enables us to change Equation 5.5 into

$$\sigma_e = S_w^n \varepsilon_0\varepsilon_e\kappa^2 D_0. \tag{5.7}$$

Neglecting any interactions among the neighboring particles, $\beta^*(\omega)$ reads:

$$\beta^*(\omega) = \frac{\sigma^*_g(\omega) - \sigma^*_e(\omega)}{\sigma^*_g(\omega) + 2\sigma^*_e(\omega)}, \tag{5.8}$$

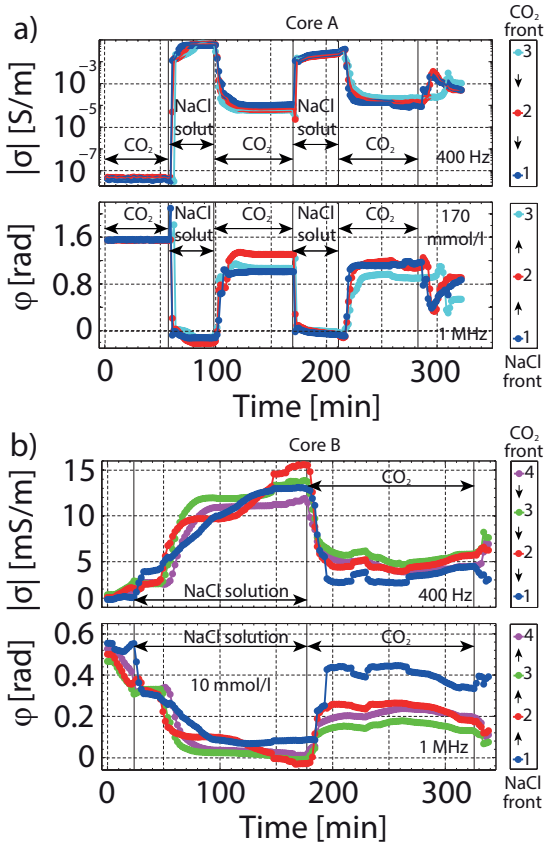

Figure 5.3: Magnitude $|\sigma|$ and phase φ of complex electrical conductivity for the whole time-run representing alternating CO_2 and NaCl solution flooding of the reservoir rock sample at P≈80bar and T≈43°C. The measurements are shown for a specific frequency, where the changes in measurements are the most pronounced: 400 Hz for $|\sigma|$ and 1 MHz for φ. Two different NaCl concentrations are presented: (a) C_s = 10 mmol/l, (b) C_s = 170 mmol/l. The color of the symbols refers to $|\sigma|$ and φ measured by different electrode pairs (see Figure 5.1).

where $\sigma_g^*(\omega) = i\omega\varepsilon_0\varepsilon_g$ is the complex conductivity of the grain, with ε_g being the relative dielectric permittivity of the grain.

The impedance of the pseudo-inductance effect is given by $Z_L(\omega) = d/(A\sigma_L^*(\omega))$ and the complex conductivity of pseudo-inductance by:

$$\sigma_L^*(\omega) = \sigma_e^*(\omega)\,\frac{1+2(1-\phi)\beta_L^*(\omega)}{1-(1-\phi)\beta_L^*(\omega)}, \tag{5.9}$$

where the dipolar coefficient is now taken to be:

$$\beta_L^*(\omega) = \frac{\sigma_g^*(\omega)-\sigma_e^*(\omega)+2\sigma_L^{\parallel}+\sigma_L^{\perp}}{\sigma_g^*(\omega)+2\sigma_e^*(\omega)+2\sigma_L^{\parallel}-2\sigma_L^{\perp}}. \tag{5.10}$$

Here, $\sigma_L^{\perp} \approx \sigma_e$ and $\sigma_L^{\parallel} = \alpha\sigma_e$ are perpendicular and parallel conductivities of any extra

conductive layer close to the grain surface and α is a real dimensionless coefficient. In this chapter, $\alpha = 10^{-4}$ is used for core A and $\alpha = 10^{-3}$ for core B. Chapter 4 is referred for more details.

5.4. RESULTS AND DISCUSSION

Laboratory core flooding experiments have been conducted to study the sensitivity of the complex electrical conductivity to CO_2 migration within a reservoir rock sample. All NaCl/CO_2 flooding experiments are performed over a time span of 350 minutes. During this time it was possible to conduct two consecutive NaCl/CO_2 injection cycles using core A and another injection cycle using core B. The saturation process takes longer for core B because the total pore volume of core B is substantially larger than that of core A. At the initial stage of each experiment, the empty pores of the dry sandstone core are flooded by supercritical CO_2. Once the core is flooded with several pore volumes of CO_2, the cores are assumed to be fully CO_2-saturated, and the CO_2-bearing ISCO pump is switched to standby mode. Saline water is then injected into the core until a new saturation is reached (see Figure 5.3). During the next phase of the experiment the saline water pump is switched to standby mode and the core is flooded again with supercritical CO_2. The CO_2 injection is also conducted at a flow rate of 1 ml/min, like the saline water. The cycle is then repeated for the core A.

The data presented in Figure 5.3 illustrate that DS measurements are saturation dependent as both magnitude, $|\sigma|$, and phase, φ, of complex electrical conductivity change during the CO_2/NaCl injections. This is in agreement with the results of earlier experiments done by Dafflon et al. [2013]. $|\sigma|$ increases and φ decreases with increasing of the saline water saturation. The behavior is opposite when the core is flooded with CO_2. Ulrich and Slater [2004] studied water drainage and imbibition by measuring the spectral induced polarization of unconsolidated sands in the frequency range upto 1 kHz under ambient pressure-temperature conditions using a 4-electrode terminal. Their work suggests to consider saturation in order to predict the measured polarization response of partially saturated reservoirs. In this experiment, the complex electrical conductivity of a consolidated rock is measured. The rock is saturated with the mixture of saline water and CO_2 in the frequency range between 20 Hz and 3 MHz using the 2-electrode terminal. Contrary to Ulrich and Slater [2004], it will be shown that the information about bulk properties can be obtained from the higher frequency range.

Figure 5.3a illustrates the difference between the primary and the secondary saturations of saline water and CO_2. It is clear that the measured values of $|\sigma|$ and φ for the primary CO_2 flooding (conducted between 100 min and 170 min) are unreachable by the secondary saturation of CO_2 (conducted between 210 min and 280 min). This is due to residual water saturation of the core. The same phenomenon is observed for all electrode pairs.

Figure 5.9 show S_w^n values obtained from the best-fit model for the measured $|\sigma|$ and φ. The root-mean-square error is 3.3% and 20% for fits $|\sigma|$ and φ fittings, respectively. For all these figures, only S_w^n is fitted, as C_s is known from the salinity of the injected saline water. The mismatch between the modeled φ and the measured one at low frequencies (see Figure 5.6) is due to EP.

Figure 5.8 shows the frequency dependence of the measured $|\sigma|$ and φ, indicating

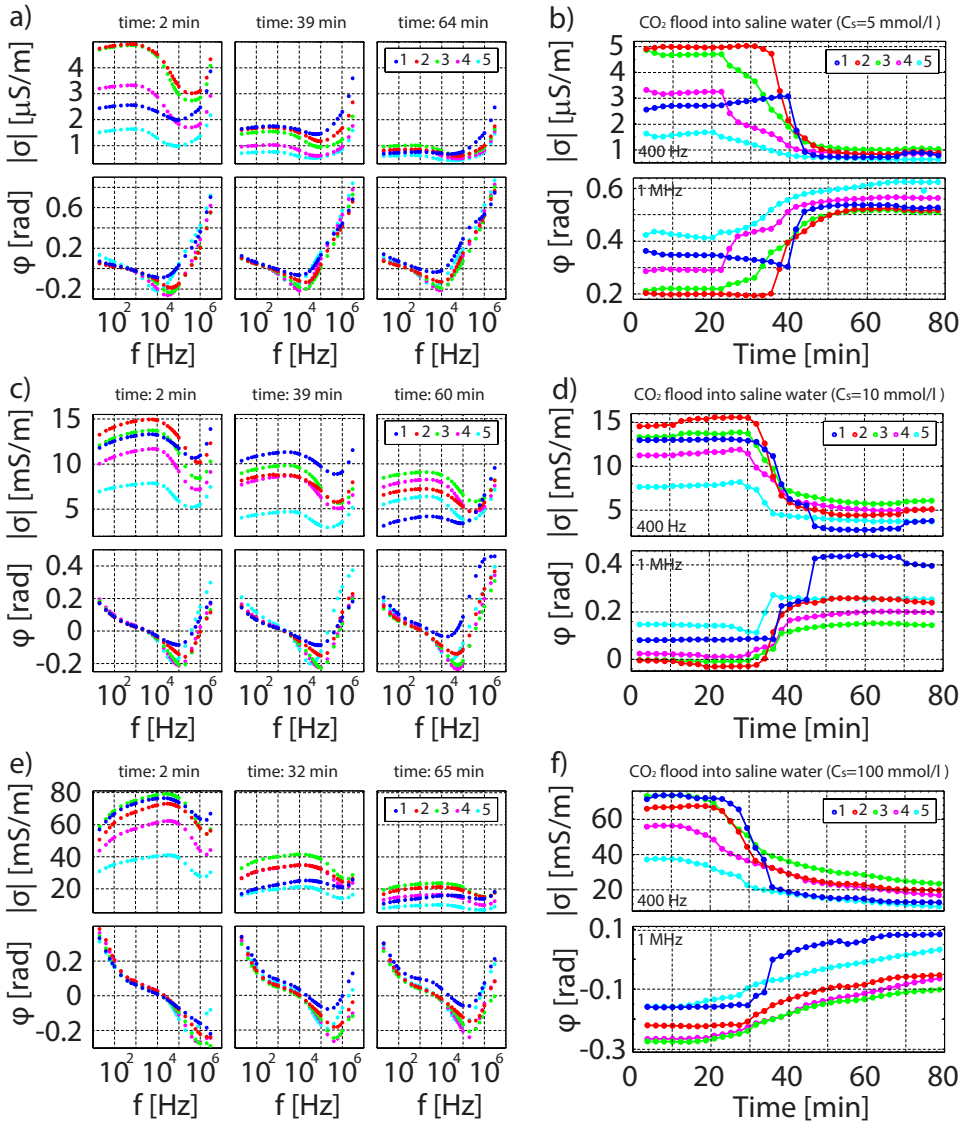

Figure 5.4: $|\sigma|$ and φ time-lapse spectra (a, c) for different electrode pairs correlated to the CO_2 saturation of the saline-water-bearing reservoir rock (b, d). Core B with C_s = 170 and 510 mmol/l.

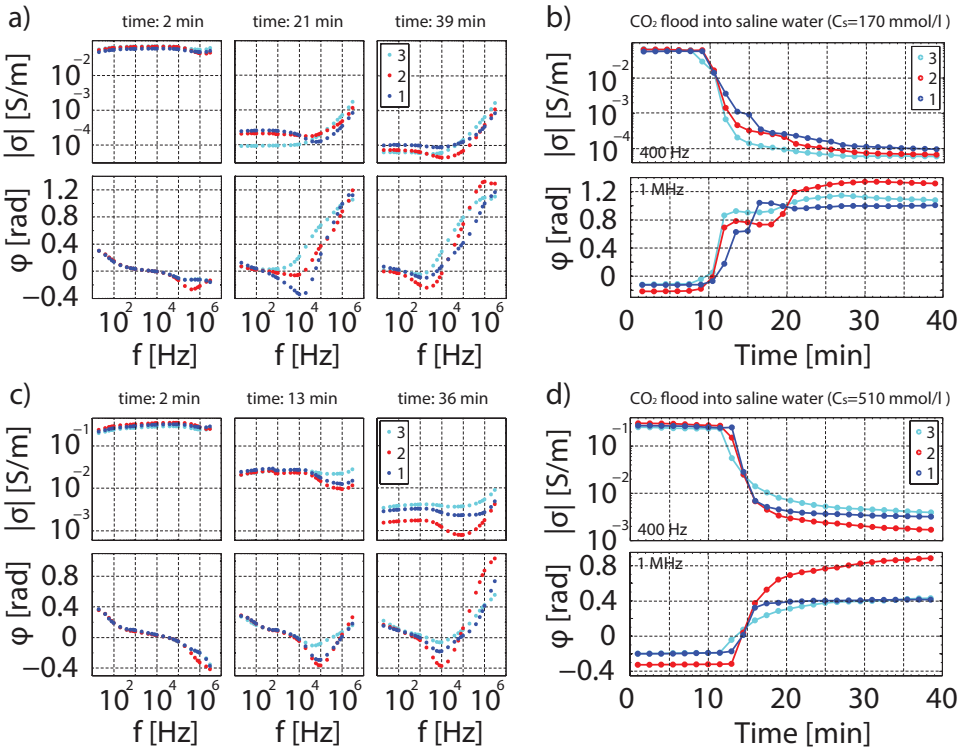

Figure 5.5: $|\sigma|$ and φ time-lapse spectra (a, c, e) for different electrode pairs correlated to the CO_2 saturation of the saline-water-bearing reservoir rock (b, d, f). Core A with C_s = 5, 10 and 100 mmol/l.

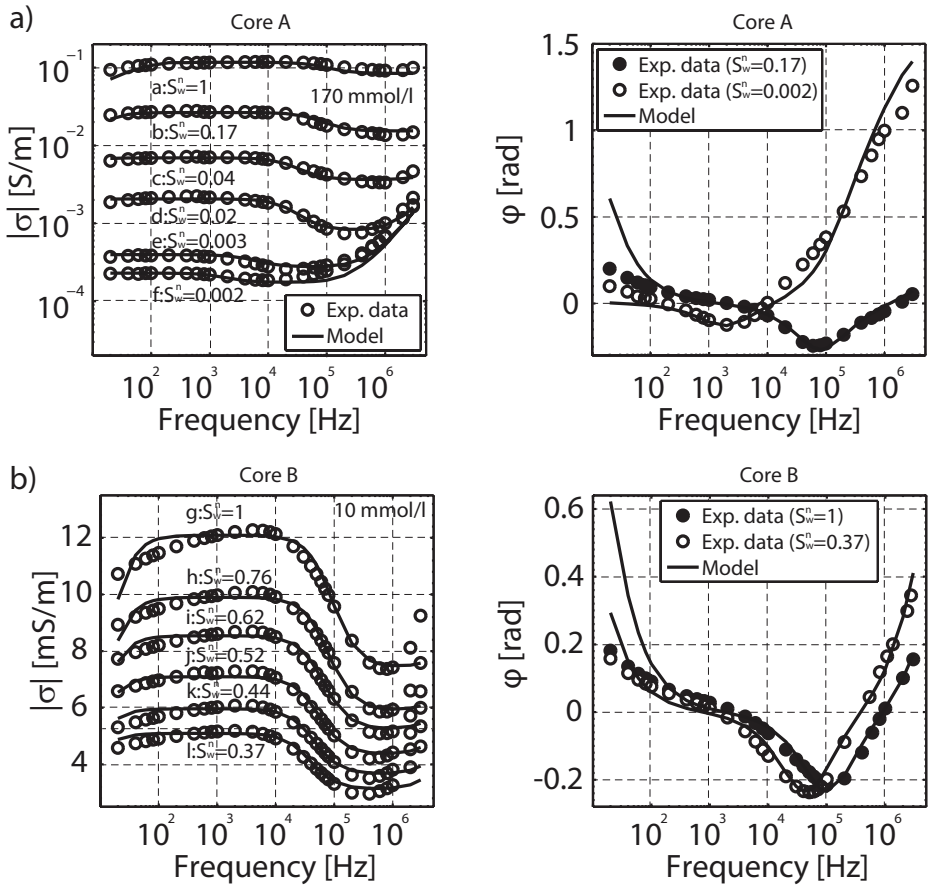

Figure 5.6: $|\sigma|$ and φ spectra for different saturations and NaCl concentrations. The fitting (solid line) is done using S_w^n as the only adjustable parameter. The measurements are shown in symbols.

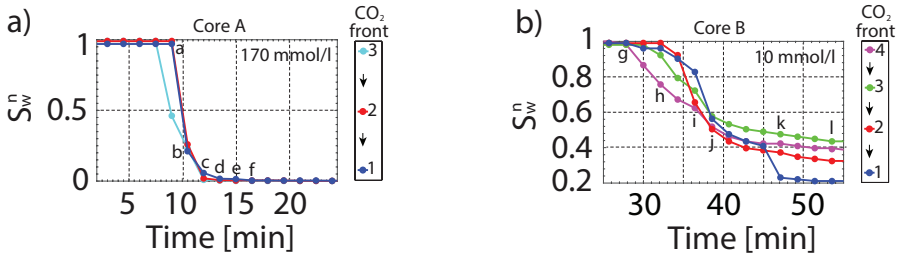

Figure 5.7: Model-fitted S_w^n during CO_2 injection in the saline water-saturated reservoir rock as a function of time. (a) Core A: C_s = 170 mmol/l and (b) Core B: C_s = 10 mmol/l.

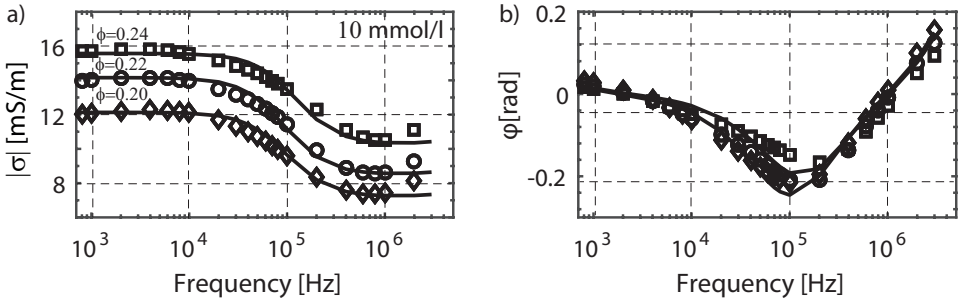

Figure 5.8: $|\sigma|$ and φ spectra for 3 different electrode pairs, indicating differences in effective porosity in core B saturated with 10 mmol/l NaCl. The symbols represent the experimental data. Effective porosity is derived using the model in Section 5.3 (solid line).

the existence of different polarization effects. The bulk polarization is partially masked by electrode polarization at low frequencies as discussed in the previous chapter. All spectral induced polarization ($|\sigma|$ and φ) curves show a peak in the 10 kHz − 1 MHz range, which changes in intensity and peak frequency with varying saturation and concentration of the electrolyte.

Figures 5.8 shows the effect of spatial heterogeneity and fluid filling in the Bentheimer sandstone cores. In the case of a homogeneous core, the porosity is constant over the entire length of the core and $|\sigma|$ and φ are the same at all electrode pairs. The observed differences in the measured values can be attributed to varying local porosities. This is consistent with other works [Ghorbani et al., 2008, Johnson et al., 2013]. These differences can also be due to the fact that only partial saturation is achieved for a given electrode pair. In that case, even though pore distribution is homogeneous in the core, the effective porosity values are different, as some pores are not entirely filled with saline water.

The model described in Section 5.3 is used to derive the effective porosity from the measured data, for each electrode pair, at full saturation ($S_w = 1$), using α found in Chapter 4. The result of the modeling and the predicted effective porosity values are shown in Figure 5.5. A least-square approach is used to minimize the residual between the model and the data. Both residuals for magnitude and phase of complex electrical conductivity are calculated separately. The best fit parameters are calculated by minimizing these two

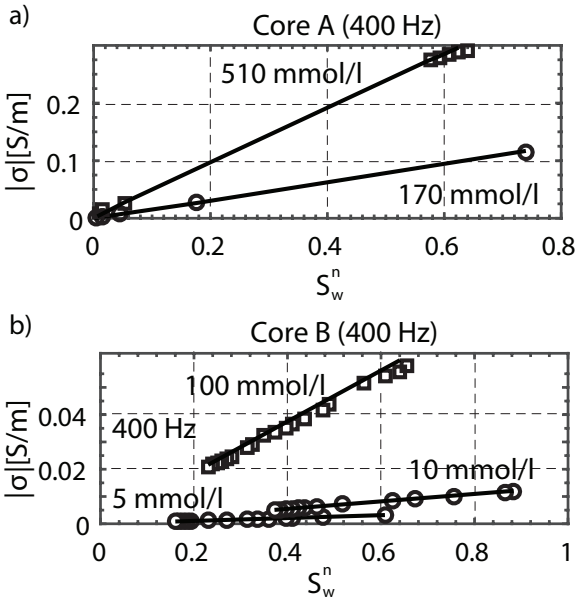

Figure 5.9: Variation of $|\sigma|$ with varying saline water saturations for different NaCl concentrations. The dashed lines represent the model given in Section 5.3. The measurements are given in symbols. Intermediate saturations cannot be recorded for core A because of the instantaneous saturation time during the injections.

residuals simultaneously. As expected, the obtained porosity values differ only by a few percent between electrode pairs. Inversely, knowing the porosity of a reservoir rock, it is possible to estimate α within a few % of uncertainty for each electrode pair.

Once the effective porosity ϕ and α values are found by fitting the measured data on a core which is fully saturated with saline water of known salinity, it is then possible to find both C_s and S_w^n for a saline water of unknown salinity that is injected in the core.

One important remaining question for a given core and unknown CO_2 saturation and electrolyte concentration is: is it possible to determine simultaneously the saturation S_w^n and salt concentration C_s? Figure 5.10 illustrates the example of one fully and one partially saturated sandstone core. Even though the low-frequency conductivity (<10 kHz) is the same for two different sets of electrolyte concentration and saturation values, the conductivity for these two different sets differ at higher frequencies, where the pseudo-inductance effect is most pronounced (>10 kHz). It is therefore possible to fit each curve using a unique set of parameters (S_w^n, C_s) given the broad frequency range (20 Hz - 3 MHz).

5.5. CONCLUSION

Two Bentheimer sandstone samples (of different geometries), flooded repetitively by either CO_2 or saline water of different NaCl concentrations, are investigated using spectral induced polarization. For the first time, such measurements are carried out in the laboratory at carbon capture and storage (CCS) reservoir conditions (P≈80 bar, T≈43°C)

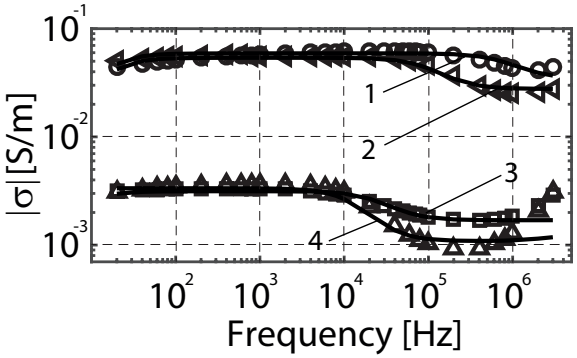

Figure 5.10: $|\sigma|$ spectra for 4 different measurements (symbols) and the corresponding fitting (line). Despite the fact that in the low-frequency range curve 1 coincides with curve 2, and curve 3 coincides with curve 4, each dataset can be fitted with a single set of parameters (S_w^n, C_s). This is because the pseudo-inductance effects are very sensitive to saturation. (1): S_w^n=1, C_s=100 mmol/l; (2): S_w^n=0.44, C_s=170 mmol/l; (3): S_w^n=1, C_s=5 mmol/l; (4): S_w^n=0.08, C_s=510 mmol/l.

using a multiple electrode pair system. These experiments enabled us to follow the supercritical CO_2 front in time along the length of the samples.

The model of complex electrical conductivity including different polarization mechanisms is presented in Chapter 4. It is found that the effective porosity and α coefficients in the model can uniquely be determined by fitting the measurements obtained for a fully saturated sandstone sample with a known electrolyte. In the present chapter, the Maxwell-Wagner model, which is presented in Chapter 3, is extended to account for partial saturation. This led to the inclusion of an additional saturation parameter S_w^n in the definition of electrical conductivity.

Once the porosity and α are found by fitting the impedance spectrum of a reservoir rock, which is saturated with an electrolyte of known concentration (S_w^n=1), it is possible to fit the impedance spectrum of the same rock which is saturated with a fluid of unknown salinity and saturation. A unique set of parameters (S_w^n, Cs) is then found. The fitting is possible due to the fact that the pseudo-inductance effect which is observed at high frequencies is very sensitive to S_w^n.

6

P-WAVE VELOCITY DISPERSION (100 KHZ - 1 MHZ) IN CO_2-SATURATED SANDSTONE: ULTRASONIC MEASUREMENTS AND POROELASTIC MODELING

The mind is like a parachute,
it only works when it is open

Frank Zappa

In this chapter, the applicability of P-wave velocity dispersion and attenuation for CO_2 storage monitoring is studied. The P-wave velocity dispersion and attenuation estimates are obtained during water imbibition and CO_2 drainage of Bentheim sandstone in the laboratory at ultrasonic frequencies. The sensitivity of these estimates is tested by adjusting the pore pressure from 10 bar to 95 bar. Obtained velocities and attenuations show strong sensitivity to pore pressure changes of CO_2-saturated reservoir rock. The pore pressure is varied from 10 bar to 95 bar and the temperature from 27°C to T=33°C to monitor the transition between vapor, liquid and supercritical CO_2. During these experiments the CO_2 and water are subsequently injected into the pore space of the sandstone. The obtained estimates in fully- and partially-saturated sandstone are analyzed using the theory of poroelasticity. The partial and patchy saturation phenomena are used to predict saturation of sandstone from velocity dispersion estimates. The measured data can be potentially used in combination with electrokinetic measurements for more reliable and efficient CO_2 storage monitoring.

6.1. INTRODUCTION

Seismic geophysical surveys are well suited for monitoring of geological CO_2 storage [Arts et al., 2004, Daley et al., 2008, Lüth et al., 2011]. In particular, time-lapse seismic surveys have been successfully adopted at Ketzin and Sleipner CO_2 storage locations for tracking CO_2 plumes propagation in the reservoir. Understanding the physics of wave propagation in porous rocks is thus important for CO_2 storage monitoring. Predicting reservoir properties such as pressure, temperature, water saturation, permeability and porosity can be useful in the quantitative interpretation of seismic data. Underlying rock physics controlling intrinsic losses can give us valuable insight into the stratigraphy, lithology, and fluid contents of the survey area. Distinguishing the nature of reservoir fluids by their elastic signature is a key issue in reservoir monitoring. Water and CO_2 commonly coexist in CO_2 storage reservoirs, and an accurate assessment of the CO_2 and water contents are of a primary importance for assessing the storage potential of the reservoir and for verifying that the injected CO_2 is safely contained in the reservoir as planned. The uncertainty in the geophysical interpretation of the CO_2 storage monitoring data can, however, be unacceptable [Chadwick et al., 2008]. In this pursuit, laboratory experiments can be of fundamental importance for the interpretation of in-situ seismic measurements [Bourbiè et al., 1987].

Unlike field geophysical surveys, laboratory experiments provide data, where the values of controlling physical parameters (e.g. pore and confining pressures, temperature and fluid saturation) can be independently measured. These data are necessary in order to obtain a better understanding of the elastic wave velocity dispersion and attenuation mechanisms in porous media during CO_2 storage. Conventionally, seismic attributes, i.e. P-wave and S-wave velocities and attenuations of rocks, are measured at the laboratory conditions [Subramaniyan et al., 2014, Winkler and Plona, 1982]. P-wave velocity has provided most of the known information about the structure and properties of reservoir rocks. Studying experimentally the role of fluid content, viscosity, size of heterogeneities and permeability are well-known challenges [Müller et al., 2010, Vogelaar, 2009]. Batzle et al. [2006] conducted laboratory experiments over a broad frequency range, from 5 Hz to 800 kHz. These authors show a significant velocity dispersion in rocks at low seismic-strain amplitudes. Distinguished fluid mobility effect is reported on the velocity dispersion in porous rocks. The authors clearly demonstrated that mesoscopic and microscopic fluid-flow models can successfully explain their data. Adam et al. [2009] studied the fluid effect on P-wave, S-wave, extensional wave and bulk compressibility attenuations at both seismic (10-1000 Hz) and ultrasonic (800 kHz) frequencies in carbonate rocks. This work reports attenuation measurements of P-waves in the range $10^{-2} < Q^{-1} < 0.5$. Unlike P-wave velocity measurements, P-wave attenuation estimates are much more limited in use, partly because it is difficult to obtain the value of intrinsic dispersion (both velocity and attenuation), but also because it is difficult to interpret in terms of rock properties due to the lack of knowledge of the physical processes involved in attenuation mechanisms. Attenuation is referred to the total loss of energy of an elastic wave along its propagation path resulting from absorption, scattering and diffraction. The loss of energy of an elastic wave, that leads to temperature rises of a medium, results in absorption. Scattering and diffraction result in a redirection of wave energy from the original direction of propagation.

Frequency dependence of the P-wave velocity and attenuation in porous CO_2 storage reservoir rocks can potentially be used to bridge laboratory ultrasonic measurements to the quantities that are conventionally determined from in-situ seismic surveys or cross-well seismic data. An experimental approach consists in investigating the wave induced fluid flow and fluid heterogeneities in consolidated rocks using ultrasonic transducers [e.g., Bourbiè et al., 1987, Mavko and Nolen-Hoeksema, 1994]. One of the first CO_2-related laboratory studies on P-wave velocities in rocks was carried out by Wang and Nur [1989]. In this study P- and S-wave velocities were measured before and after CO_2 injection into reservoir rock which was initially saturated with n-hexadecane. Later on the signatures of seismic velocities were captured during CO_2 injection into core samples, which were initially saturated by an oil/water mixture [Wang et al., 1998]. In both cases, the experiments were conducted under realistic reservoir conditions. These experiments revealed profound sensitivity of P-velocities to CO_2 flooding. One of the first applications of ultrasound studies that are related to CO_2 storage were done by Xue and Ohsumi [2004] and Xue et al. [2005]. Using an array of sixteen piezoelectric transducers, the authors monitored the gaseous CO_2 front propagation in a water-bearing reservoir rock. It was shown that the largest velocity decrease can be measured by injecting supercritical CO_2 [Shi et al., 2007, Xue and Lei, 2006]. Later on, Lei and Xue [2009] developed tomographic images of relative attenuation coefficient to capture the CO_2 migration in a water-saturated sandstone. It was reported that the attenuation coefficient increased most during the injection of supercritical CO_2. Purcell et al. [2010] performed seismic velocity measurements on a sandstone at reservoir temperatures, varying pore pressure while maintaining constant confining pressure. Their results showed large velocity fluctuations with phase changes. Alemu et al. [2013] used CT-methods to monitor the CO_2 distribution into brine-saturated sandstone through acoustic velocity variations. Recent works were dedicated to velocity measurements during CO_2 injection in various type of porous rocks [e.g., Kim et al., 2013, Lebedev et al., 2013, Siggins et al., 2010, Zemke et al., 2010]. In particular, Cadoret et al. [1995] and Lebedev et al. [2009] showed that mesoscopic patches are created during the drainage process, implying strong differences of velocity contrary to imbibition where the saturation is more homogeneous.

The main objective of this research is to study, in the context of geological CO_2 storage monitoring, P-wave velocity dispersion and attenuation by using a new well-controlled laboratory setup that allows us to control pore and confining pressures, temperatures, and saturating fluids. The novelty of this work is estimating of P-wave velocity and attenuation from laboratory ultrasonic measurements, which are conducted on the 2-layered sample mimicking both the cap rock and the reservoir for CO_2 storage. Realistic reservoir conditions can be effectively achieved by controlling pore and confining pressures, temperature and saturating fluids of the samples. The ultrasonic measurements are conducted simultaneously with electrokinetic measurements presented in Chapter 5. The integration of both ultrasonic and electrokinetic measurements can potentially result in reliable geophysical monitoring methods, potentially resulting in scientifically-proven quantification of CO_2 storage monitoring. The discussion on the integration of two monitoring methods is presented in the following chapter.

This chapter is structured as follows. First, the main principles of the theory of poroelasticity are briefly recalled. The ultrasonic measurements, data processing and estima-

tion of P-wave velocity dispersion and attenuation are presented in the following sections. Finally, it is discussed how these measurements can be interpreted.

6.2. THEORY OF POROELASTICITY

Interfacial interactions between fluid and solid phases during elastic wave propagation in porous media are originally described by Biot's poroelastic theory [Biot, 1956a,b, 1962]. Appendix A is referred for the details of Biot theory. Three kinds of body waves, two longitudinal (P) and one transverse (S), are originated because of the energy dissipation due to the relative fluid/solid motion. The faster longitudinal wave (fast P-wave) is weakly dispersive whereas the slower P-wave (Biot's slow wave), is highly dispersive and diffusive at low frequencies. This work is focused only on the fast P-wave.

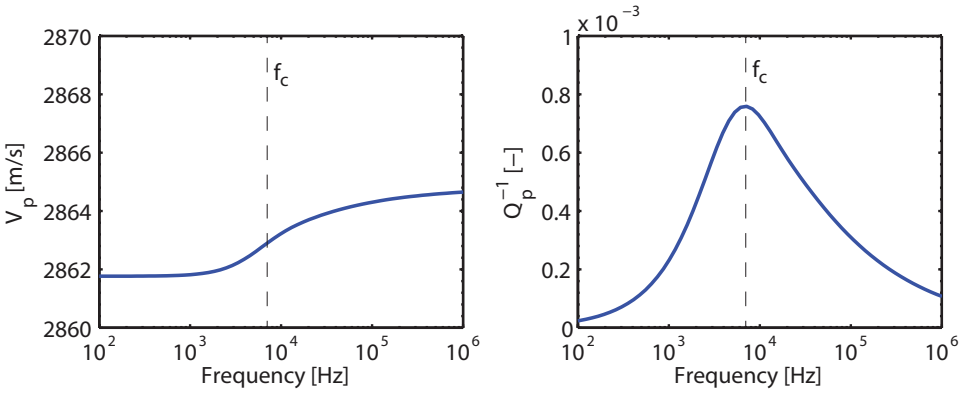

Figure 6.1: Theoretical velocity and attenuation spectra from the Biot theory.

Biot theory assumes that the porous medium is saturated and that wavelengths are larger than the grain size. To account for a partial saturation, the most conventional approach is to introduce the concept of 'effective fluid' into the original Biot's poroelastic model. This method is valid as long as wavelengths are larger than the size of the heterogeneities in the porous medium. In this case, the full pressure equilibration between fluids is possible during one period of wave propagation and the well-known Biot-Gassmann's relations are valid. When this equilibration is not totally achieved, wave induced fluid flow phenomena at microscopic [Barrière et al., 2012, Dvorkin and Nur, 1993, Mavko and Nur, 1979, Pride et al., 2004] or mesoscopic scale [Johnson, 2001, White, 1975] are considered to be the main dispersion and attenuation mechanisms. At microscopic scale, water is squeezed due to an elastic wave, resulting in a local flow often called 'squirt flow' (see Appendix B for more details). At a larger scale, energy is dissipated by fluid pressure diffusion between mesoscopic patches of gas and the surrounding water. In consolidated rocks, squirt flows can be strong at ultrasonic frequency [Müller et al., 2010], therefore it will be considered here.

In Biot's theory, the elastic wave propagation induces a frequency dependent relative motion of the fluid with respect to the solid matrix. Figure 6.1 shows the relaxation frequency f_c, also known as characteristic Biot's frequency, that is defined as

$$f_c = \frac{\phi\eta}{2\pi\alpha\rho_f\kappa} \tag{6.1}$$

where ϕ is the porosity of the reservoir rock, η is the dynamic viscosity of the fluid, α is the tortuosity, ρ_f is the density of the fluid and κ is the permeability of the reservoir rock. Biot showed that the motion of fluid flow at $f < f_c$ is controlled by viscous shearing whereas at $f > f_c$ inertial forces are dominant. He showed that the seismic attenuation peaks at f_c since both viscous and inertial forces play an important role at that particular frequency.

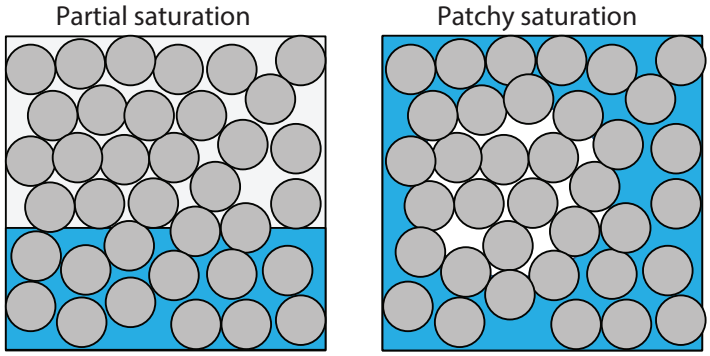

Figure 6.2: Schematic representation of partial and patchy saturations of a porous medium.

It has been proven that the Biot loss mechanism can accurately predict the P-wave velocity dispersion. However, it gives an under-prediction of P-Wave attenuation in porous media. In the quasistatic limit, at e.g. seismic frequencies, Biot's model is consistent with Gassmann's theory and is equivalent to the case of elasticity theory. It has been found that the pore-filling fluid does not have sufficient time to redistribute itself so as to locally equilibrate the pore pressure at higher frequencies, in particular in the logging (10 kHz) or laboratory ultrasonic (1 MHz) bands. In this regime, the mesoscopic effective models can not resemble the physics of elastic wave attenuation of a fluid-saturated porous medium.

6.2.1. PARTIAL SATURATION

The most conventional approach in modeling the effect of partial saturation on velocity dispersion and attenuation is using the effective fluid method. Since bulk moduli of the different fluid phases have different stress-induced pore pressure, the effective fluid method considers the time, that is necessary to equilibrate between these pore pressures, to be smaller than the relaxation time $\tau = 1/f$, with f being the frequency. In this case, the fluid phases are finely mixed at the smallest scales so that the pore-pressure increments equilibrate with each other to a single effective value. Following the definition of the characteristic relaxation time [Mavko et al., 2009]

$$\tau \simeq \frac{L^2}{D}, \tag{6.2}$$

where the heterogeneous pore pressure of scale L must satisfy the following condition:

$$L \leq \sqrt{\tau D} \tag{6.3}$$

in which $D = \kappa K_f/\eta$ is the diffusivity coefficient, κ is permeability, K_f and η, are fluid bulk modulus and viscosity, respectively. If this condition is satisfied, then the effective fluid bulk modulus can be described well by the Reuss average [Mavko et al., 2009]. If the porous material is saturated with CO_2-water mixture, the contributions of water (subscript w) and the CO_2 (subscript $co2$) are taken into account in by

$$\frac{1}{K_f} = \frac{S_w}{K_w} + \frac{S_{co2}}{K_{co2}} \tag{6.4}$$

and

$$\frac{1}{\eta_f} = \frac{S_w}{\eta_w} + \frac{S_{co2}}{\eta_{co2}}, \tag{6.5}$$

The effective density of fluid can be estimated by a standard mixing rule

$$\rho_f = S_w \rho_w + S_{co2} \rho_{co2}. \tag{6.6}$$

6

6.2.2. PATCHY SATURATION

Patchy saturation is commonly considered if the fluid distribution in the porous material has various degrees of heterogeneity. Typically, patches of different size can occur in the porous rock. In this case the bulk modulus of considered media varies spatially and the shear modulus remains uniform due to it's insensitivity to the pore filling fluid. The effective bulk modulus can be obtained by the patchy (or Gassmann-Hill) limit that reads

$$\left(K_u + \frac{4}{3}G\right)^{-1} = S_w \left(K_b^w + \frac{4}{3}G\right)^{-1} + S_{co2}\left(K_b^{co2} + \frac{4}{3}G\right)^{-1}, \tag{6.7}$$

where K_u and G are the undrained bulk and shear moduli. The bulk moduli of the water- and CO_2-saturated porous material, K_b^w and K_b^{co2}, are defined as

$$K_b^w = K_b + \frac{(1 - K_b/K_s)^2}{\phi/K_w + (1-\phi)/K_s - K_b/K_s^2} \tag{6.8}$$

and

$$K_b^{co2} = K_b + \frac{(1 - K_b/K_s)^2}{\phi/K_{co2} + (1-\phi)/K_s - K_b/K_s^2}, \tag{6.9}$$

respectively. Figure 6.2 shows the conceptual difference between partial and patchy saturations. In case of partial saturation two fluid phases are mixed at the finest scale. Hence, the saturation is homogeneous. Patchy saturation is more heterogeneous than partial saturation. Therefore, isolated CO_2 pockets, CO_2 channels or gas bubbles in the porous rock can be considered as examples of patchy saturation.

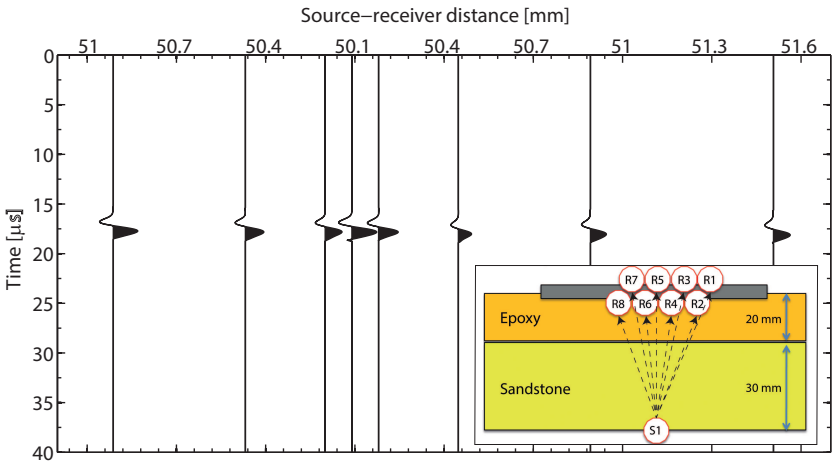

Figure 6.3: An example of the recorded common-source gather for the transmitted P-waves through the 2-layer sample.

6.3. LABORATORY EXPERIMENTS

A series of well-controlled laboratory experiments has been conducted in order to understand the influence of reservoir properties on the P-wave velocity dispersion and attenuation. In particular, the effects of pore pressure and temperature on the P-wave velocity dispersion and attenuation have been analyzed during the first experiment. The goal of the second experiment is to study the P-wave velocity dispersion and attenuation during the water and CO_2 saturations.

6.3.1. LABORATORY SETUP

The test sample consists of two layers. The Bentheimer sandstone layer representing a CO_2 storage reservoir and the overlying layer of epoxy have a width of 30 mm and 20 mm, respectively. In total nine piezoelectric transducers are used in these experiments. One transducer serves as a source and the other eight transducers, that are mounted on the epoxy layer, serve as receivers. An example of a common-source gather, that is generated using this acquisition geometry, is shown in Figure 6.3. Figure 6.4 shows the spectra of the recorded (transmitted) signal at 8 receivers from a common source that is located on the other side of the sample. With the high center frequency of 1 MHz of the source transducer, the peak frequency of the received signal is less than 600 kHz. This is due to attenuation of higher frequencies in the porous sample.

Stainless-steel end pieces are attached to both sample ends and a grooved plate was placed between the end piece and the sample at each end. Concentric grooves connected by radial grooves are carved on the plate surface to ensure uniform injection over the entire surface of the sample's end. The sample is sealed with a silicone rubber to prevent immersion of oil that is used as the confining pressure medium. This assembly is then placed in a pressure chamber and installed inside the oven. The assembled setup allows to conduct water/CO_2 flooding experiments under reservoir con-

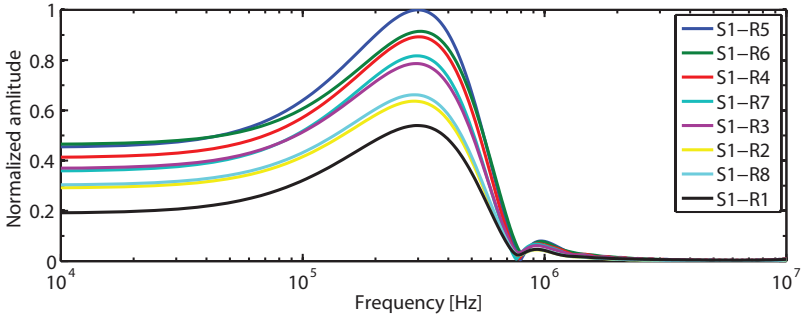

Figure 6.4: Amplitude spectra of recorded signal generated by piezoelectric transducer with center frequency of 1 MHz.

ditions (P=110 bar, T=50 °C).

The gaseous/supercritical CO_2 is flooded from the top end and water is injected from the bottom end of the sample at a constant pressure controlled by two syringe pumps. Pore pressure is monitored at both ends of the sample. The third syringe pump is used to keep the confining pressure constant in the vessel. By keeping constant pore pressure at both ends, and holding constant confining pressure, velocity changes caused by pore pressure build-up are minimized. Hence, changes in observed data reflect only displacement between CO_2 and water within the pore-space of the sample. A more detailed description of the laboratory setup and measuring equipment is given in Chapter 2.

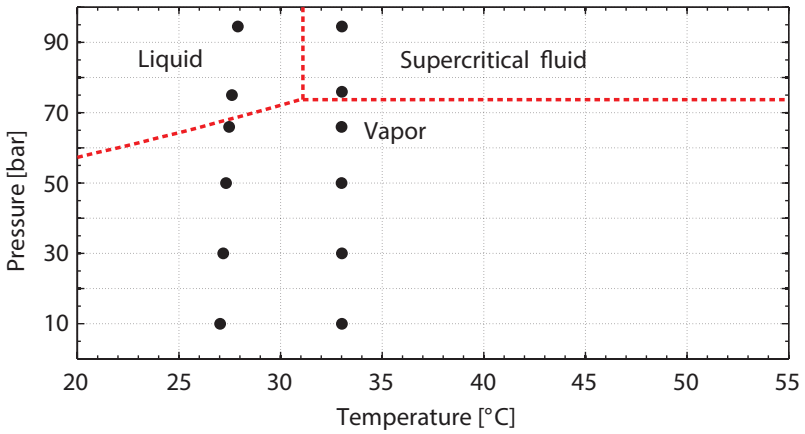

Figure 6.5: The sequence of pressure/temperature change and CO_2 phase transitions in the experiment. Black circles show the conditions when the velocity dispersion and attenuation are estimated.

6.3.2. EXPERIMENT 1: PORE PRESSURE AND TEMPERATURE VARIATIONS

Figure 6.5 shows the diagram of this experiment. Gaseous CO_2 is firstly injected from the top of the water-saturated sample at a pressure of 10 bar while the pressure at the bottom was kept constant. When the sample is saturated with gaseous CO_2 and with residual wa-

ter, the pore pressure and confining pressure are continuously increased while keeping the effective pressure constant at 10 bar. The measurements are conducted at maintained temperature of 27°C when the pore pressure reaches 10, 30, 50, 65, 75 and 95 bar covering the CO_2 phase transition from gaseous to liquid state. When the pore pressure reaches 95 bar, the temperature is increased up to 33 °C. This stage of the experiment guarantees the transition of CO_2 from liquid to supercritical fluid phase. During the next stage, the pore pressure drops from 95 bar to 10 bar. During this pressure drop, the phase of CO_2 is changed from supercritical fluid to gaseous.

6.3.3. EXPERIMENT 2: WATER/CO_2 SATURATION VARIATIONS

The experiment is conducted in three phases. During the Phase 1, water is injected into a pore space of a dry sample. The water imbibition experiment has been performed under reservoir conditions in the Phase 2. The supercritical CO_2 drainage has been conducted during the Phase 3.

PHASE 1: WATER INJECTION INTO A DRY SAMPLE

Ensuring homogeneous saturation of the pore volumes within the porous rock sample is a challenging task. With low water saturation, the distribution of water would most likely be in the region where it is injected or even possibly on the surface of the sample. This water distribution is not representative of the bulk properties since much of the pore spaces of the sandstone is saturated by moisture and not representative of situations likely to occur in reservoirs. If the subsurface saturation occurs over a long time scale, then this allows for enough time for the capillary redistribution of saturation. Hence, a more homogeneous saturation distribution has to be achieved by using low injection rates of the saturating fluids.

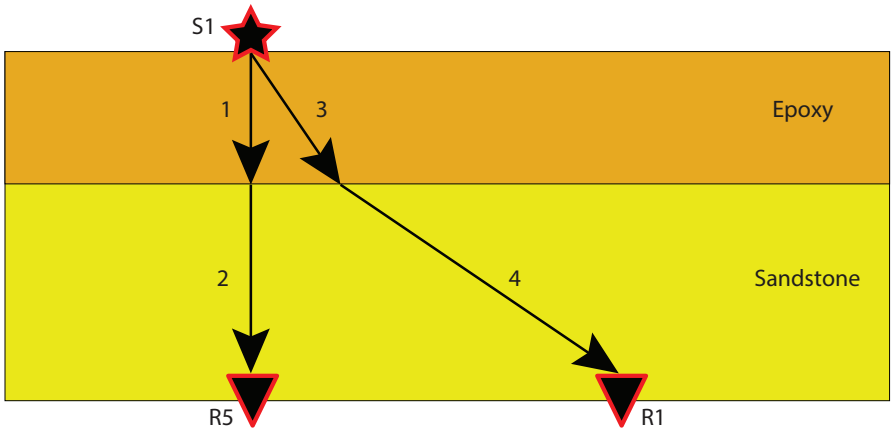

Figure 6.6: Sketch of seismic raypaths within the 2-layered sample. The raypaths labeled 1,3 and 2,4 illustrate transmissions through the epoxy and sandstone layers, respectively.

The sample is dried at room conditions for several weeks and further vacuumed for several hours before the start of the experiment. Once the dry state is verified, the CO_2

is flooded through the pore space of the reservoir rock and the temperature is set up to 43°C. Confining and pore pressure are then slowly increased to 15 bar and 10 bar, respectively. Next, 1 pore volume of fresh distilled water is injected from the bottom end of the sample at a constant flow of 1 ml/min.

PHASE 2: WATER IMBIBITION UNDER RESERVOIR CONDITIONS

During this phase of the experiment the pore pressure, confining pressure and temperature are maintained at 95 bar, 105 bar and 43°C, respectively. Initially, the sample has CO_2 and residual water in the pores. Water imbibition is carried out with constant flow of 1 ml/min. In total, three pore volumes of water are subsequently injected. The imbibition process is equivalent to the water injection into a dry porous rock that is described above.

PHASE 3: SUPERCRITICAL CO_2 DRAINAGE

The pore pressure, confining pressure and temperature of this phase of the experiment are equivalent to those of Phase 2. Two pore volumes of CO_2 are used for the supercritical CO_2 drainage experiment with constant flow of 1 ml/min. The drainage process is quite different from the imbibition [Lei and Xue, 2009]. The thick surface water layers and the thin interconnected CO_2 phase structure are not considered during the drainage process. In contrast, the water is substituted by CO_2 from each pore as it was progressed through the rock, removing all but the first few mono-layers of water from the grains surface.

In the end of the experiment the Phases 2 and 3 are repeated in order to check the consistency of the P-wave velocity estimates and repeatability of the experiment. In this case, 4 pore volumes of supercritical CO_2 are subsequently injected into the sample.

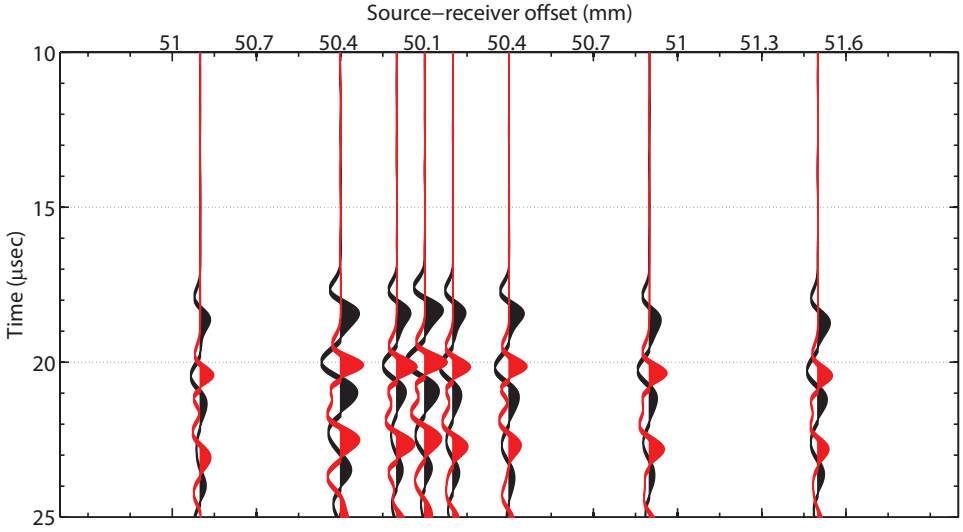

Figure 6.7: Recorded common-source gather for transmitted P-waves through the 2-layered sample that is saturated with CO_2 (red color) and water (black color).

6.4. P-WAVE VELOCITY DISPERSION

6.4.1. ESTIMATION OF P-WAVE VELOCITY DISPERSION FROM THE DATA

Figure 6.6 illustrates the seismic raypaths inside the 2-layered sample. Since both layer thicknesses of the 2-layered sample are known, the propagation velocity of the P-wave inside the sandstone layer can be obtained from the recorded transmission, which has propagated along path 1-2. Using independent transmission measurements on an epoxy cylinder, the P-wave velocity in epoxy is estimated to be 2880 m/s. This velocity is used to estimate the P-wave velocity inside the sandstone layer from the recorder transmission from the source S1 to the receiver R5. Both velocities, the measured one inside the epoxy layer and the estimated one inside the sandstone layer, are then utilized for calculating the length of P-wave propagation paths 3 and 4 using Snell's law.

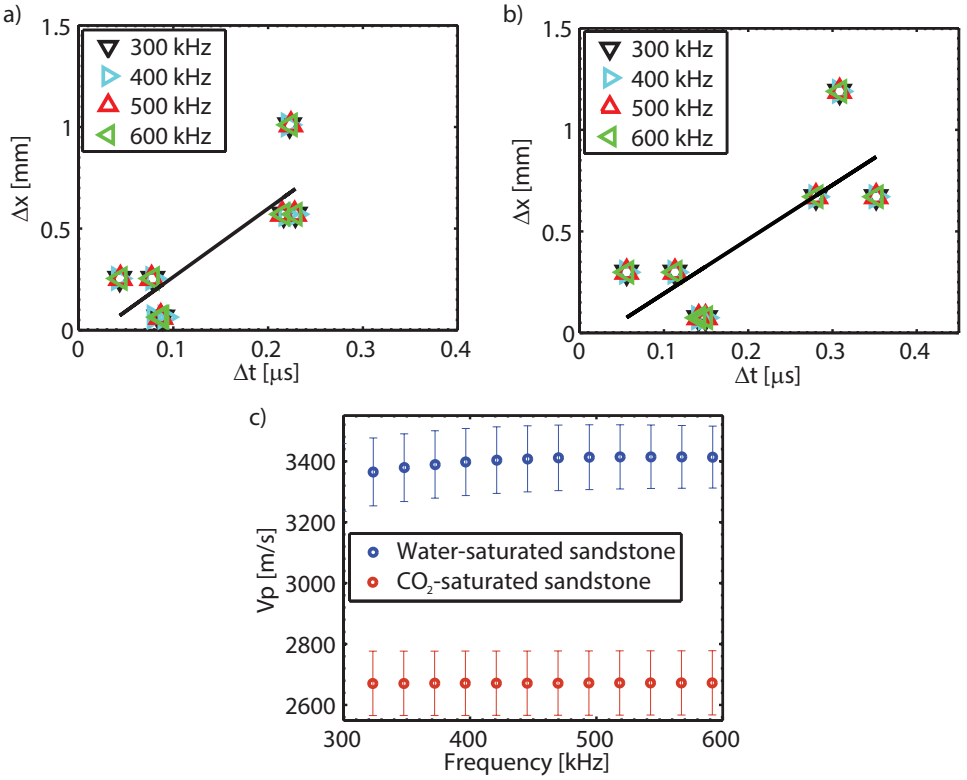

Figure 6.8: P-wave velocity estimation inside the sandstone later. The best line fitting in a least-square sense for the water-saturated (a) and CO_2-saturated (b) sandstone layers at P_p=77 bar and T=39°C. c) The slope of the best-fit provides the estimates of V_p in the frequency range of 300-600 kHz.

The estimated lengths of propagation paths inside both layers of the 2-layered sample are then accounted while estimating the phase difference for a given frequency $\Delta\phi$. The phase velocity inside the sandstone layer $V_p(f)$ for a given frequency f can be obtained for every propagation path inside the sandstone layer as follows [Molyneux and

Schmitt, 2000, Zhubayev, 2014, Zhubayev and Ghose, 2012b]:

$$V_p(f) = \frac{\Delta x}{\Delta t} = \frac{2\pi\Delta x}{\Delta\phi(f)} f, \tag{6.10}$$

where Δx is the relative distance between the propagation paths inside the sandstone layer and Δt is the relative phase delay time for a given frequency.

Figure 6.7 shows the common-source gather for transmitted recordings through the 2-layered sample that is saturated with CO_2 and water. These data are used to retrieve Δt inside the sandstone layer for estimating the slope of the best-fit line by linear regression of Δx-Δt distribution, that corresponds to the phase velocity. These regressions for 300, 400, 500 and 600 kHz are depicted in Figures 6.8a and 6.8b for CO_2-saturated and water-saturated sandstone data, respectively. The frequency band 300-600 kHz lies in the band of the signal frequency (see Figure 6.4); therefore, this band is demonstrated here. The velocity dispersion curve, that is obtained for all frequencies within 300-600 kHz, is shown in Figure 6.8c. The standard deviation of the calculated velocity dispersion for each frequency is calculated from the scatter in Figures 6.8a and 6.8b. The vertical bars indicate the standard deviations of the estimates.

6.4.2. EXPERIMENT 1: PORE PRESSURE AND TEMPERATURE VARIATIONS

The P-wave velocity dispersion that is obtained during well-controlled pore pressure variations inside the sample are shown in Figure 6.9. Remarkably, the velocities measured at P_p=65 bar, T =27°C and P_p=75 bar, T =33°C are much lower than other estimated velocities. The proximity of these pressure-temperature conditions is very close to the critical ones, when pore-filling CO_2 is in the state of transition between the gas and liquid phase during pore pressure rise (Figure 6.9a) and between supercritical fluid and gaseous phase during pore pressure decrease (Figure 6.9b). Apart from these two estimates, obtained P-wave velocities exhibit a stable and consistent variation with the pore pressure. In both cases, a steady increase in velocity values is observed during the pore pressure build-ups.

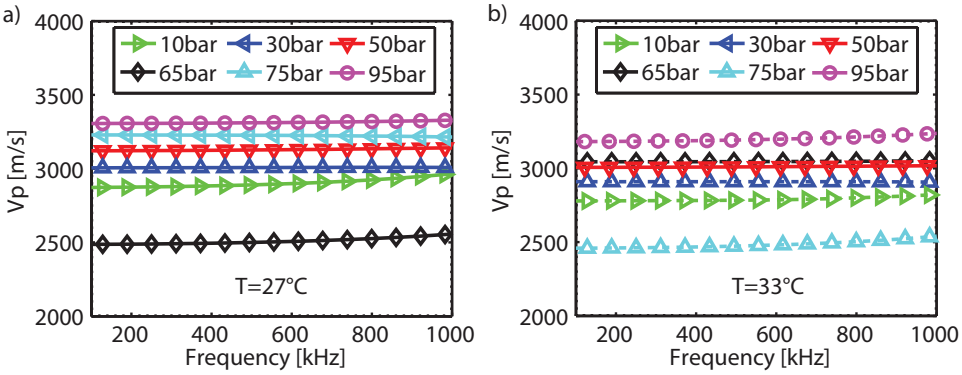

Figure 6.9: Obtained P-wave velocity dispersion in the sandstone layer that is saturated with CO_2 and residual water. a) Pore pressure is elevated from 10 to 95 bar at T = 27 °C. b) Pore pressure is reduced from 95 to 10 bar T = 33°C.

The rise in temperature from T =27°C to T =33°C results in a velocity drop by 3% for high pore pressures (50-95 bars) and by 1-1.5% for low pore pressures (10-30 bars). High pressure variations with temperature are most probably related to a compressibility change of CO_2 that is in the pore space of the sandstone layer. The compressibility of liquid CO_2 is typically higher that the one of the supercritical CO_2. The low pressure variations can be attributed to residuals, or local pressure build-ups, that still contribute to estimated P-wave dispersion at the final stage of the experiment.

This experiment shows that reliable estimates of the P-wave velocity dispersion can be extracted from laboratory measurements, keeping well-controlled pressure and temperature conditions. Further work should be focused on scientifically-proven links between P-wave velocity dispersion estimates and pore pressure/temperature variations.

6.4.3. EXPERIMENT 2: WATER/CO_2 SATURATION VARIATIONS

Figure 6.10 shows the estimates of P-wave velocity dispersion inside the 2-layered sample and inside the sandstone layer during water injection into the pore space of the rock. At the beginning of the water injection, water saturation in a dry sandstone is increased through the adsorption of water on the surfaces of the pore space. During this process, thick surface layers of water with an interconnected CO_2 phase are developed. A small frequency dependence of V_p is already observed at $S_w = 0.2$. Below a critical water saturation, the existence of a thin interconnected CO_2 phase keeps essentially all pores in a partially saturated state. The water/CO_2 mixture is effectively homogeneous in the pore space and its compressibility is given by volume averaged water and CO_2 compressibilities. The variation in V_p at low water saturations is due primarily to a bulk density effect with a slight V_p drop due to an increase of the bulk density.

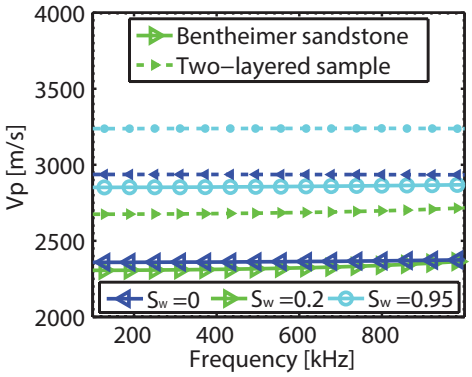

Figure 6.10: Estimation of velocity dispersion of 2-layered sample (dashed line) and sandstone layer (solid line) from the measured data. The measurements are conducted during water injection into the sandstone's pore space. The estimates are shown for water saturations of 0, 0.2 and 0.95.

When the injection of water continues by soaking up the porous sandstone, the water continues to move along and coat the surfaces until the closure occurs between the layers of surface water. At this moment the rearrangement of water and gas to a more thermodynamically stable configuration occurs, resulting in the filling of the central vol-

umes of the pores with water. At this saturation range, the P-wave velocity increases until full water saturation is achieved. The same effect is observed during the imbibition experiments. The results of P-wave velocity dispersion estimates, which are obtained during the imbibition at realistic reservoir conditions, are shown in Figure 6.11. The estimated velocities for the sample with CO_2 and residual water are considerably higher than the ones obtained during the water injection into the pores of a dry sample. This is not only because of different pore pressure and temperature, but also because of a difference in the initial saturation conditions.

At high saturation levels, pore water is forced from completely saturated regions to dry regions of porous media. This effect can be achieved by injecting more volumes of water into the pore space. Figure 6.11 illustrates the variation of the P-wave dispersion estimates with injected pore volumes of water. Clearly, the estimates are higher with injecting more pore volumes of water, suggesting that full water saturation has not been achieved.

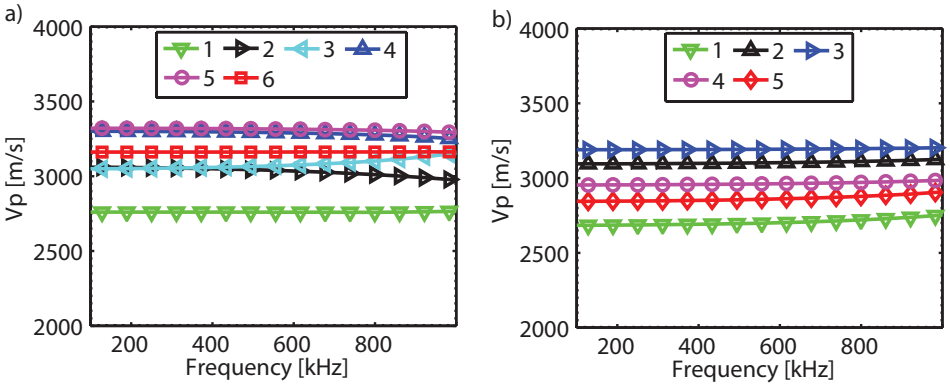

Figure 6.11: P-wave velocity dispersion obtained during water imbibition and supercritical CO_2 drainage at P_p =95 bar, T =43°C. a) [1] the sample is saturated with supercritical CO_2 and residual water. The sample is flooded with: [2] one pore volume of water; [3] two pore volumes of water; [4] three pore volumes of water; [5] one pore volume of supercritical CO_2; [6] two pore volumes of supercritical CO_2. b) [1] the sample is saturated with supercritical CO_2 and residual water. The sample is flooded with: [2] one pore volume of water; [3] two pore volumes of water; [4] three pore volumes of supercritical CO_2; [5] four pore volumes of supercritical CO_2.

The drainage shows a remarkably different behavior. Injection of one pore volume of supercritical CO_2 results into a very small change of the P-wave velocity estimate. In contrast to gaseous CO_2 drainage, when the water is drained from the pore space as CO_2 propagates [Kirichek et al., 2013], the supercritical CO_2 drainage experiment suggests that non-homogeneous CO_2 saturation has typically occurred. It is a fair assumption that a fingering effect occurs in water saturated sandstone during supercritical CO_2 flooding. As is shown in Figure 6.11b, the injection of additional pore volumes of CO_2 results into a further P-wave velocity decrease of 10% with respect to the water-bearing sandstone. Additional pore volumes of CO_2 enlarge the width of the CO_2 channels and secondary fingers as CO_2 propagate into the pore space of the sandstone. Accurate ultrasonic monitoring of CO_2 saturation can potentially be achieved by coupling ultrasonic measurements with the method that provide the imaging of the CO_2 saturation distribu-

tion (fingering) as a function of time.

6.4.4. PREDICTION OF P-WAVE VELOCITY DISPERSION

Prediction of the P-wave velocity dispersion is shown in Figure 6.12. The P-wave velocity dispersion is obtained from ultrasonic measurements conducted on a water saturated sample under P_p =10 bar and T =43°C. Biot theory is used here to predict the obtained P-wave velocity dispersion curves. This model is given in the previous subsection and the parameters used for modeling can be found in Tables 6.1 and 6.2. The values for ϕ, k, ρ_s, K_s, G and α are taken from Smeulders [1992] and Wisse [1999].

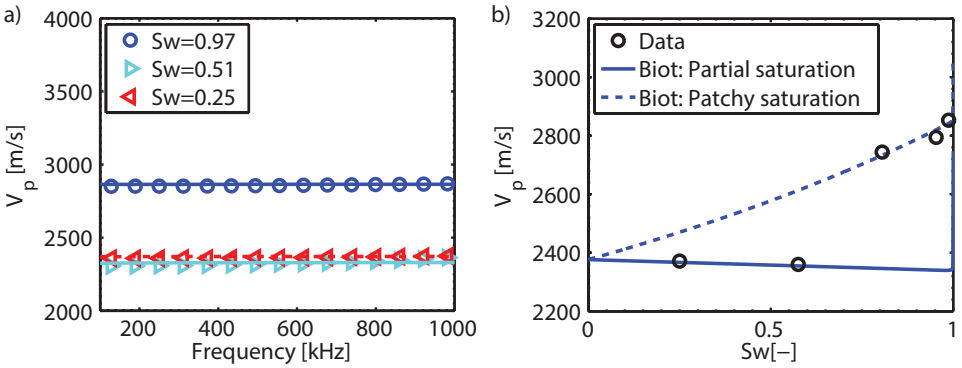

Figure 6.12: a) Prediction of the P-wave velocity dispersion by Biot theory. b) Partial and patchy saturation mechanisms for imbibition and drainage experiments. The data is shown for f = 800kHz.

Figure 6.12 shows the effect of partial and patchy saturation on the P-wave velocity during imbibition and drainage experiments. The obtained P-wave velocity dispersion estimates in water-saturated rock are verified by employing classical Biot theory with partial and patchy saturation concepts. During the imbibition process, water injection produces a homogeneous distribution of water and CO_2 phases. The total pore spaces contains both water and CO_2, leading to saturations that are approximately constant at all locations and directions. The P-velocity estimates obtained during the imbibition experiment confirm homogeneous water distribution within the pore space. Thus, the partial saturation concept is suitable for the velocity estimates which are obtained during imbibition experiments.

Table 6.1: List of bulk parameters for predicting the P-wave velocity dispersion

ϕ –	k μm^2	ρ_s kg·m^{-3}	K_b GPa	K_s GPa	G GPa	α –
0.23	3.7	2650	7	36	3.4	2.37

Contrary to imbibition, CO_2 drainage experiments reveal a patchy saturation effect. In contrast, the CO_2 drainage results in a more heterogeneous distribution of fluids in the pore space. This leads to the segments of fully saturated pores and regions adjacent

to partially saturated parts of the sample. These channels can be treated as patches of CO_2 that result into a steady velocity decrease during the CO_2 drainage.

Table 6.2: List of fluid parameters for predicting the P-wave velocity dispersion

ρ_f kg·m^{-3}	ρ_{gas} kg·m^{-3}	K_f GPa	K_{gas} kPa	η_f cP	η_g cP
1000	19	2.3	101	1	0.15

6.5. CONCLUSION

The P-wave velocity dispersion is estimated during water imbibition and supercritical CO_2 drainage from a 2-layered sample at ultrasonic frequencies. The obtained estimates in water-saturated rock are verified by employing classical Biot theory. The sensitivity of estimates is investigated by adjusting the pore pressure from 10 bar to 95 bar. Velocity estimates show strong sensitivity to pore pressure changes of CO_2-saturated reservoir rock. The effect of CO_2 channeling is captured by velocity dispersion during CO_2 drainage at reservoir conditions. It should be verified whether the estimates of P-wave velocity dispersion could be coupled to electrokinetic measurements in order to predict reservoir properties for CO_2 storage monitoring. The partial and patchy saturations are used to predict water saturation during imbibition and CO_2 drainage experiments. CT-scan experiments might provide valuable insight into the correlation of multiphase saturation experiments with P-wave velocity dispersion estimates of partially saturated rock.

6.6. APPENDIX A: BIOT THEORY

The porous medium is considered to be isotropic, with rigid skeleton that has a uniform porosity and compressible pore-filling fluid [Biot, 1956a,b]. The deformations are assumed to be reversible and elastically linear. Thus, the strains for the solid phase yields [Landau and Lifshitz, 1970]

$$e_{ij} = \frac{1}{2}\left(\frac{\partial u_j}{\partial x_i} + \frac{\partial u_i}{\partial x_j}\right) \tag{6.11}$$

The symmetry principle is applied, thus $e_{ij} = e_{ji}$. Here, $\mathbf{u}$ represents the displacement vector of solid.

Assuming isothermal conditions the constitutive equations read [Sivukhin, 2005]

$$\tau_{ij} = 2Ge_{ij} + (H - 2G)e\delta_{ij} + C\zeta\delta_{ij} \tag{6.12}$$

and

$$p_f = M\zeta - Ce. \tag{6.13}$$

where τ_{ij} is the total stress on a solid component of the porous structure, p_f is the pore pressure, δ_{ij} is the Kronecker delta function, $e = \nabla \cdot \mathbf{u}$ is the volumetric strain, $\zeta = \nabla \cdot (\phi(\mathbf{u} - \mathbf{U}))$ is the in/out flow of fluid and $\mathbf{U}$ is the displacement vector of fluid. The elastic coefficients H, C, M are related to measurable quantities, e.g. to the bulk modulus of a

porous skeleton K_b, the bulk modulus of a grain K_s, the bulk modulus of the pore-filling fluid K_f, by [Biot, 1962, Stoll, 1977]

$$H = \frac{(K_s - K_b)^2}{D - K_b} + K_b + \frac{4}{3}G, \tag{6.14}$$

$$C = \frac{K_s(K_s - K_b)}{D - K_b}, \tag{6.15}$$

$$M = \frac{K_s^2}{D - K_b}, \tag{6.16}$$

where

$$D = K_s\left(1 + \phi\left(\frac{K_s}{K_f} - 1\right)\right). \tag{6.17}$$

Equations 6.12, 6.13 are then combined with the equation of flow in a porous medium in order to derive the equations of motion governing the propagation of dilatational waves [Stoll, 1977]

$$\nabla^2(He - C\zeta) = \frac{\partial^2}{\partial t^2}\left(\rho e - \rho_f \zeta\right), \tag{6.18}$$

$$\nabla^2(Ce - M\zeta) = \frac{\partial^2}{\partial t^2}\left(\rho_f e - m\zeta\right) - \frac{\eta}{k}\frac{\partial \zeta}{\partial t}, \tag{6.19}$$

where ρ and ρ_f are the densities of total mass and fluid, respectively, η is the fluid viscosity, k is the permeability of the porous system, $m = \alpha\rho_f/\phi$ is the added mass and α is the tortuosity. To deviate from Poiseuille flow, Biot [1956b] introduced a frequency dependence to the drag coefficient η/k by multiplying it by

$$F^* = \frac{1}{4}\frac{\xi T^*}{1 + 2iT^*/\xi} \tag{6.20}$$

with

$$T^* = \frac{ber'(\xi) + ibei'(\xi)}{ber(\xi) + ibei(\xi)} \tag{6.21}$$

and

$$\xi = a\sqrt{\frac{\omega\rho_f}{\eta}}, \tag{6.22}$$

where $ber(\xi)$ and $bei(\xi)$ are the real and imaginary parts of the Kelvin function, ω is the angular frequency and a is a pore shape and size dependent parameter that is experimentally found to be between 1/6 and 1/7 of the mean grain diameter [Stoll, 1974].

6.7. APPENDIX B: Q^{-1} SPECTRA

Similar to Jeng et al. [1999], Zhubayev [2014], Zhubayev and Ghose [2012a], an adaptation of the spectral ratio method is used to estimate effective attenuation (Q^{-1}) in the sandstone layer. A time window around the peak amplitude of the first arrival of the P-wave is automatically selected for all measurements. Figure 6.13a shows the logarithmic spectral amplitude ratio of the first-arrival P-wave for 300, 400, 500 and 600 kHz as

a function of time difference between the source-receiver pairs in the sandstone layer. The effective Q^{-1} is estimated from the best fit-line through the data for all the frequencies. The results are shown in Figure 6.13b, where the vertical bars indicate the standard deviations of the data. The estimates have been corrected for the geometrical spreading.

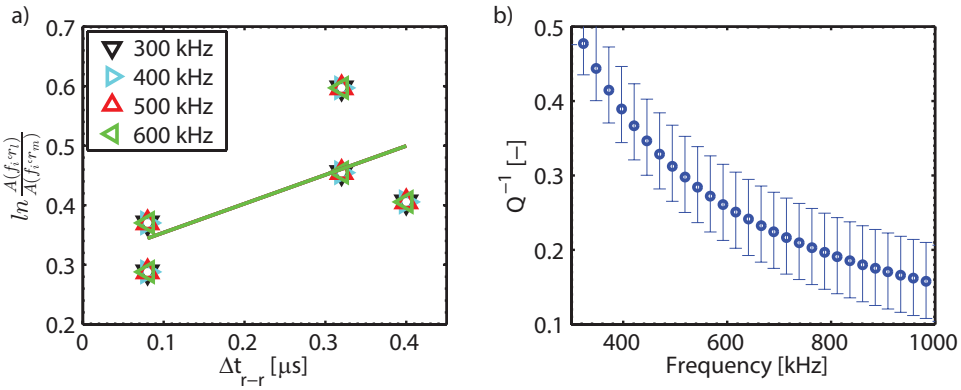

Figure 6.13: Estimation of velocity dispersion and attenuation for water-saturated sandstone layer at P=77 bar and T=39°C. a) Velocity estimation by best line fitting in a least-squares sense in the frequency range of 300-600 kHz. b) Logarithmic ratio of spectral amplitudes versus difference of the arrival time. The estimates are for the P-wave attenuation in the frequency range of 300-1000 kHz.

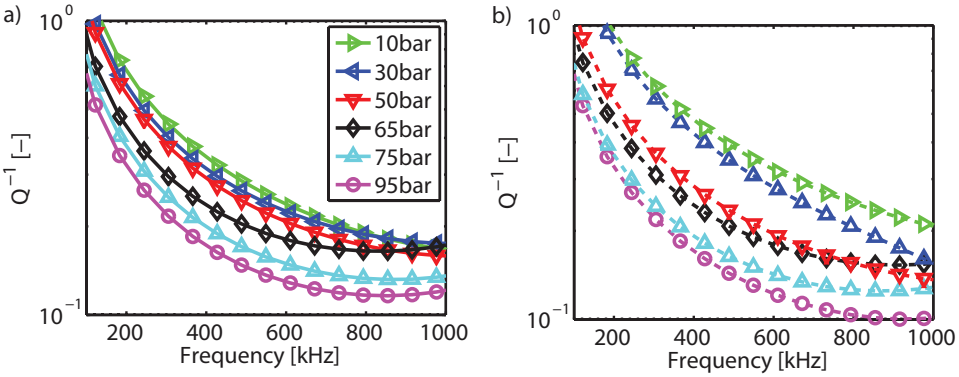

Figure 6.14: Estimated Q^{-1} in the sandstone layer that is saturated with CO_2 and residual water. a) Pore pressure is elevated from 10 to 95 bar at $T = 27$ °C. b) Pore pressure is reduced from 95 to 10 bar $T = 33$°C.

The obtained estimates at frequencies 800 kHz - 1 MHz are close to the Q^{-1} values which are reported in the literature for saturated porous rock [e.g., Marketos and Best, 2010, Mayr and Burkhardt, 2006, Toksöz et al., 1979]. However, the attenuation values that are obtained for frequencies lower than 800 kHz are higher than the literature data. Excluding the possibility of a measuring error (due to a coupling between the transducer and the sample or sample's imperfectability), there are two most possible scenarios that

can explain the obtained high values of attenuation. First, if the size of anomaly, x_a, is much greater than the wavelength λ, $\lambda << x_a$, reflection, refraction and conversion takes place. Therefore, significant amplitude losses of transmitted signal can occur on the epoxy-sandstone interface while the P-wave propagates through the 2-layered sample. Second, the geometrical divergence can result in the apparent loss of energy from a P-wave as it spreads during propagation. There is still an open question why the estimates are higher than in the literature. In this appendix, only the effective attenuation estimates in the sandstone layer are shown.

The estimated attenuation values for this experiment are shown in Figure 6.14. The estimates are consistent showing the sensitivity of Q^{-1} to pore pressure and temperature changes. The obtained values of Q^{-1} are one order higher than the ones found in the literature [e.g., Marketos and Best, 2010, Mavko and Nolen-Hoeksema, 1994]. This suggests that the intrinsic attenuation is not a dominant mechanism here.

Figure 6.15 shows the Q^{-1} estimates during water/CO_2 injections into the pore space of the sandstone layer. Again, the values of the estimates are very high. In this type of the experiment, the high values of attenuation can be attributed to different heterogeneities that dynamically develop in the sample.

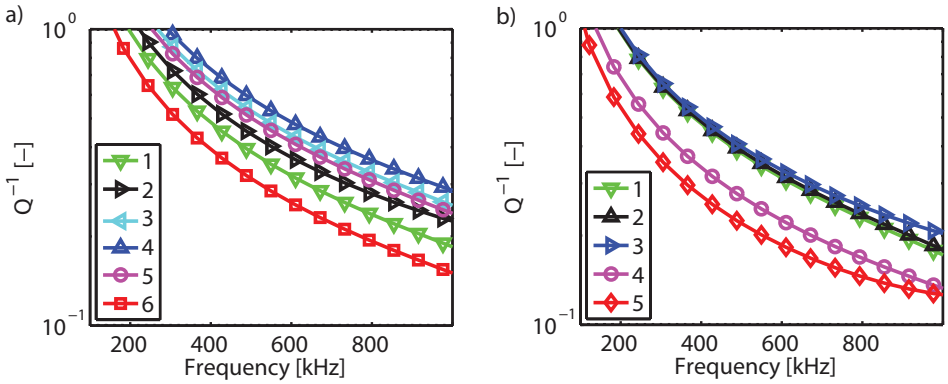

Figure 6.15: Estimated Q^{-1} during water imbibition and supercritical CO_2 drainage at P_p =95 bar, T =43°C. a) [1] the sample is saturated with supercritical CO_2 and residual water. The sample is flooded with: [2] one pore volume of water; [3] two pore volumes of water; [4] three pore volumes of water; [5] one pore volume of supercritical CO_2; [6] two pore volumes of supercritical CO_2. b) [1] the sample is saturated with supercritical CO_2 and residual water. The sample is flooded with: [2] one pore volume of water; [3] two pore volumes of water; [4] three pore volumes of supercritical CO_2; [5] four pore volumes of supercritical CO_2.

7

PREDICTING RESERVOIR PROPERTIES FROM SIMULTANEOUS ELECTROKINETIC AND ULTRASONIC MEASUREMENTS

There are more things in heaven and earth, Horatio,
than are dreamt of in your philosophy.

William Shakespeare

A reliable estimate of the reservoir properties of a porous rock is extremely challenging to obtain. It has been observed that poroelastic and electrokinetic responses of a porous material can differ in such a way that their combination gives unique estimates of permeability and porosity, water saturation and porosity simultaneously. This finding is used in the integration of complex conductivity and permittivity with P-wave velocity dispersion and attenuation in a cost function by using pertinent electrokinetic and poroelastic theories. Realistic numerical simulations show that the estimated values of permeability and porosity are robust against uncertainties in the employed physical mechanism and in the data. The frequency range of 1 Hz - 5 MHz is used in the numerical simulations for generating both poroelastic and electrokinetic responses of a porous rock. In particular, the method is applied on low-frequency synthetic field data and tested on actual laboratory measurements. The results show a high potential of this method for characterization of reservoir rocks.

7.1. INTRODUCTION

Geophysical methods have been successfully employed for quantitative characterization of fluid-bearing reservoirs in last decades. In particular, electrical methods are well-suited for characterization of shallow subsurfaces for environmental purposes [Kemna et al., 2012]. These methods have also been extensively used for cross-well measurements and well-logging [Bergmann et al., 2012, Schmidt-Hattenberger et al., 2011]. As electrical methods, seismic and sonic methods are also widely used for shallow, cross-well and log characterization [Arts et al., 2002, Lüth et al., 2011]. However, seismic methods have undisputed advantage since these methods can also be used for extracting important reservoir properties from deeper subsurface formations.

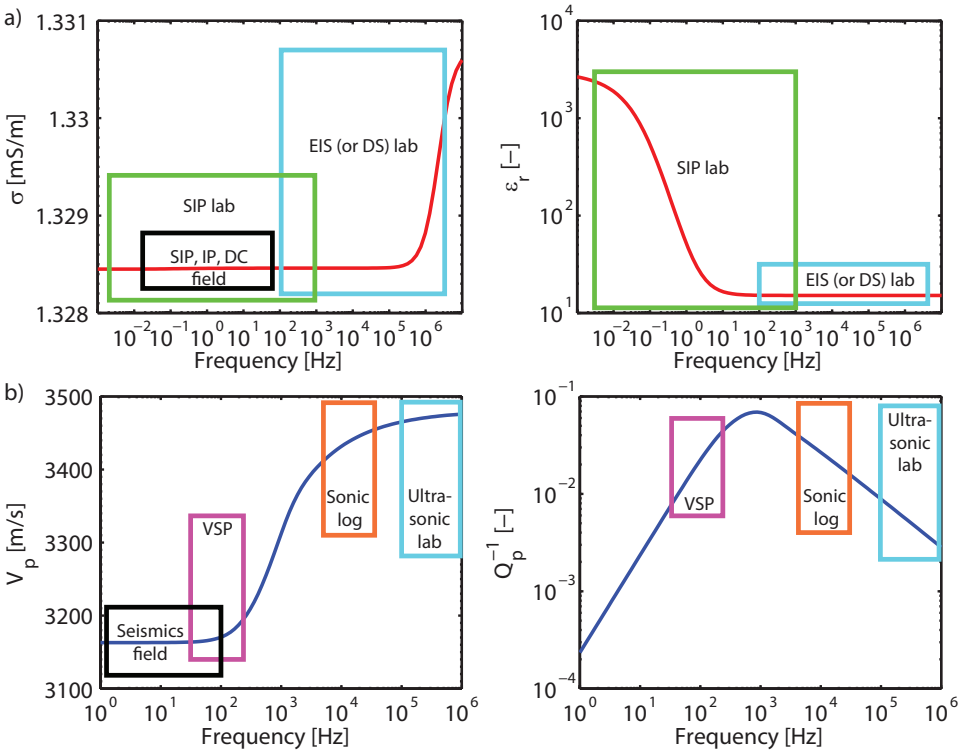

Figure 7.1: Practical applications of electrokinetic and poroelastic theories which lead to reservoir rock characterization. The spectra of spectral induced polarization (SIP), induced polarization (IP), direct current (DC), electrical impedance spectroscopy (EIS) that is also sometimes called dielectric spectroscopy (DS), seismic, vertical seismic profiling (VSP), sonic log and ultrasonic measurements are shown by rectangular boxes. a) Electrical conductivity and permittivity spectra obtained by extended Bruggeman model (see Chapter 3). b) Velocity dispersion and attenuation estimated by Biot theory (see Chapter 6).

Simultaneous application of seismic and electrical geophysical methods has not been implemented for CO_2 storage monitoring. Combining these two methods can be advantageous for reservoir characterization during CO_2 storage. On the one hand, based on electrokinetic theory, electrical methods can potentially provide valuable information

about reservoir properties. In particular, porosity salinity, temperature, zeta potential (or surface charge density), grain size and permeability can be estimated using theoretical models which explain electrical conductivity of the medium and polarization phenomena of charged reservoir grain particles [Kirichek et al., 2017, Revil et al., 2014]. On the other hand, the velocity and attenuation estimates can be deduced during seismic exploration. These estimates are later used to predict porosity, permeability, viscosity, densities and bulk moduli of reservoir rock by employing the poroelastic models that are based on Biot theory [Bourbiè et al., 1987, Mavko et al., 2009]. These reservoir properties are of primary importance for the CO_2 storage monitoring because they can be used to update the existing reservoir models and support eventual mitigation measures in case of deviation from the CO_2 storage plan.

Table 7.1: List of physical parameters and constants used in electrokinetic and poroelastic theories

Electrokinetic theory			Poroelastic theory		
Parameter	Value	Unit	Parameter	Value	Unit
Salinity, Cs	1	mM	Shear modulus, G	4.5	GPa
Diffusion coefficient, D	200	mm^2/s	Grain density, ρ_s	2650	kg/m^3
Zeta potential, ζ	100	kT/e	Water density, ρ_w	1000	kg/m^3
Temperature, T	320	K	CO_2 density, ρ_{CO2}	19	kg/m^3
Water permittivity, ε_w	80	–	Frame bulk modulus, K_b	7	GPa
Grain permittivity, ε_g	4.5	–	Grain bulk modulus, K_s	36	GPa
Vacuum permittivity, ε_0	8.85	pF/m	Water bulk modulus, K_w	2.3	GPa
Elementary charge, e	16	aC	CO_2 bulk modulus, K_{CO2}	100	kPa
Boltzmann constant, k	138	zJ/K	Water viscosity, η_w	1	mPa s
Avogadro's number, Na	600	1/zmol	CO_2 viscosity, η_{CO2}	0.15	mPa s
Stoichiometric coef., ν	1	–	Tortuosity	2.37	–

In this Chapter, an attempt is made to combine seismic and electrical methods in order to reduce the uncertainty in predicting reservoir properties. A multi-parameter cost function is used to obtain reservoir properties from electrokinetic and poroelastic models. This approach is tested on a electrokinetic and ultrasonic laboratory data for fully and partially saturated sandstone.

7.2. INTEGRATION METHOD

The integration method applied in this study has been used for inverting different reservoir properties from geophysical measurements [e.g., Ghose and Slob, 2006, van Dalen et al., 2010, Zhubayev, 2014, Zhubayev and Ghose, 2012]. The individual cost functions for P-wave velocity, V_p, P-wave attenuation Q^{-1}, electrical conductivity, σ and relative dielectric permittivity ε are defined as

$$C_N(\omega) = \left(\frac{\sum_\omega |\Delta N|^\beta}{\max\left(\sum_\omega |\Delta N|^\beta\right)} \right)^{\frac{1}{\beta}}, \tag{7.1}$$

where N indicates V_p, Q^{-1}, σ or ε, $\Delta N = \left(N^{mod}\left(\phi,\kappa,\omega\right) - N^{meas}\left(\omega\right)/s\left(\omega\right)\right)$, ω is the angular frequency, subscripts mod and $meas$ stand respectively for modeled and measured, ϕ is the porosity, κ is the permeability, $s(\omega)$ is the standard deviation, $\beta = 2$ for the L_2 norm.

A general expression for the integrated cost functions reads

$$C_{NN}\left(\omega\right) = \left(\sum_{n} \frac{\sum_{\omega} |\Delta N|^{\beta}}{\max\left(\sum_{\omega} |\Delta N|^{\beta}\right)}\right)^{\frac{1}{\beta}}, \tag{7.2}$$

where $n = 2, 3, 4$.

7.3. INTEGRATION RESULTS

To obtain σ and ε spectra, electrokinetic theory in combination with the extended Bruggeman model can be used. This model is rigorously discussed in Kirichek et al. [2017] and in Chapter 3 of this thesis and therefore not repeated in this chapter. The underlying physics of seismic wave propagation in water-saturated porous media allows to model V_p and Q^{-1} dispersions using the theory of poroelasticity. In this study, the Biot theory of poroelasticity is employed. The model description and assumptions can be found in Chapter 3 of this thesis. The physical parameters used for electrokinetic and Biot theories are given in Table 7.2.

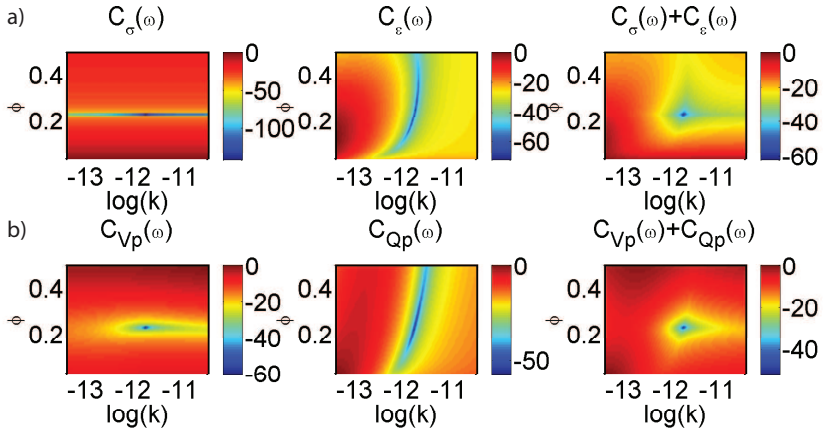

Figure 7.2: Individual and integrated cost functions in the ϕ-κ domain. a) Individual cost functions for σ, ε and integrated cost function for σ and ε. b) V_p, Q^{-1} and integrated cost function for V_p and Q^{-1}. The frequency range is 1 Hz - 5 MHz. The dark blue color points out the minimum every cost function.

Figures 7.2 illustrates all the cost functions in ϕ-κ domain for the frequency range of 1 Hz - 5 MHz. Figures 7.2a and 7.2b shows the individual costs functions for electrical and seismic attributes, respectively. Here, $\phi = 0.23$ and $\kappa = 1.5$ μm are used to obtain the minimum of the cost functions that is shown in dark blue color.

Electrical and poroelastic cost functions show similar alignment. The orientation of the cost function's minima line is totally different between σ and ε. The same holds for

V_p and Q^{-1}. While for σ and V_p, the cost function minima line is parallel to the κ-axis, this line is nearly parallel to the ϕ-axis for attenuation. This indicates that frequency dependent σ and V_p dispersion are particularly sensitive to ϕ and less sensitive to κ. This is due to the relation of κ with the relaxation frequencies of both electrokinetic and poroelastic theories. At the same time, the spectra of ε and Q^{-1} are more sensitive to κ and less to ϕ. Obviously, individual cost functions provide ambiguous global minima, thus non-unique reservoir parameters can be obtained in the $\phi-\kappa$ domain.

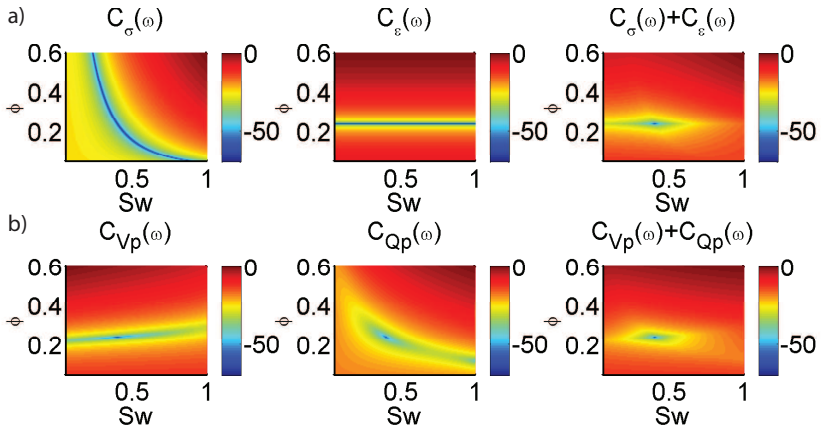

Figure 7.3: Individual and integrated cost functions in the ϕ-S_w domain. a) Individual cost functions for σ, ε and integrated cost function for σ and ε, b) V_p, Q^{-1} and integrated cost function for V_p and Q^{-1}. The frequency range is 1 Hz - 5 MHz. The dark blue color points out the minimum every cost function.

The orientations of the cost functions' minima lines of both σ and V_p are nearly perpendicular to those of respectively ε and Q^{-1} in the ϕ-κ domain. Hence, the integrated electrical and seismic cost functions are expected to result in a sharp convergence and thus into a global minimum. The integrated seismic and electrical cost functions are shown in Figure 7.2. As the result of the integration, the lines of local minima have become sharp points that indicate the global minima. Now, unique estimates of both ϕ and κ can be obtained.

Figures 7.3 shows the individual and integrated cost functions in $\phi - S_w$ domain. Here, $\kappa = 0.1$ m^2 is used to estimate S_w and ϕ values. Note, that all the cost functions are similar for partial and patchy saturations that are incorporated in the Biot theory. Therefore, only partial saturation case is considered. Individual cost functions of σ and ε resemble similar behavior as expected. Thus, the integration of these cost functions does not result into a global minimum as is shown in Figures 7.3a. The orientation of the cost function's minima line of individual V_p and Q^{-1} cost functions is totally different. First, the individual cost functions obtained for the whole frequency range (1 Hz - 5 MHz) can already independently provide not a sharp, but a unique global minimum. Second, these individual cost functions are almost orthogonal at low S_w values. Hence, sharper global minimum can be achieved by integrating the individual V_p and Q^{-1} cost

functions. These cost functions can be seen in Figures 7.3b. However, it possible to obtain a more accurate global minimum that leads to robust prediction of singular ϕ and S_w values. Figures 7.3c illustrates the result of integration of the electrical and poroelastic integrated cost functions. In this case, the maximum accuracy can be achieved and both ϕ and S_w can be explicitly obtained.

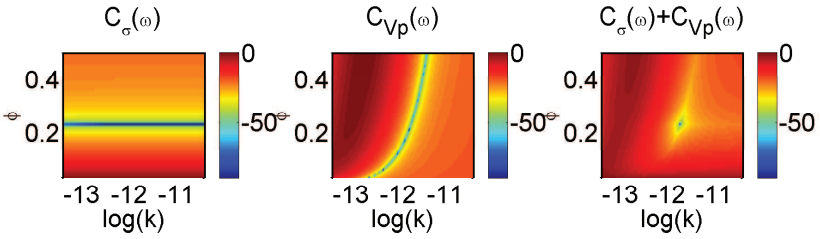

Figure 7.4: Individual cost functions for σ, V_p and integrated cost function for σ and V_p in the $\phi - \kappa$ domain in the frequency range of 1 - 100 Hz.

7.3.1. LOW FREQUENCIES

The field surveys are typically conducted in the low frequency range (see Figures 7.1). In this study, the frequency range of 1 - 100 Hz is considered representing the field scale. Obviously, it is difficult to measure ε and Q^{-1} in-situ. Therefore, only individual cost functions of σ and V_p are analyzed in this frequency range. As is shown in Figure 7.4, both individual cost functions estimate the lines of local minima in $\phi - \kappa$ domain. The orientation of these lines permits to obtain a unique global minimum by the integrated cost function.

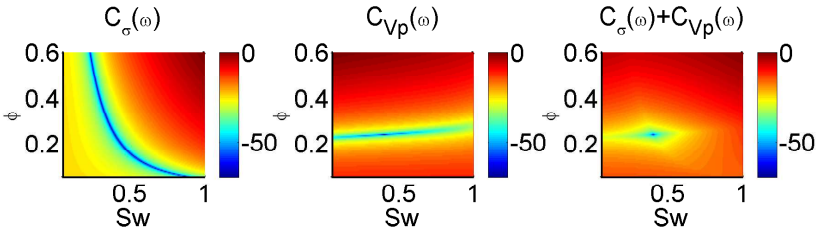

Figure 7.5: Individual cost functions for σ, V_p and integrated cost function for σ and V_p in the $\phi - S_w$ domain in the frequency range of 1 kHz - 1MHz.

A similar situation can be observed in the the $\phi - Sw$ domain. Non-exclusive local minima are produced by individual cost functions. However, the integrated cost function results in a sharp global minima. This is explicitly shown in Figure 7.5.

7.3.2. HIGH FREQUENCY

Ultrasonic and dielectric spectroscopy methods are usually carried out in the laboratory at high frequencies as schematized in Figure 7.1. Here, the frequency range of 100 kHz - 1 MHz is considered. The electrokinetic and ultrasonic laboratory data on water and

CO_2 saturated reservoir rock has been obtained in this study. Hence, velocity dispersion and complex conductivity have been estimated from the raw measurements. More details about estimation σ spectra and V_p dispersion can be found in Chapters 5 and 6, respectively.

The relaxation frequency associated with fluid mobility and grain size of the reservoir rock are well below the high frequencies considered here. Therefore, prediction of κ becomes challenging. Thus, the estimation of ϕ and S_w is only considered in the high frequency band. Figure 7.6 shows the individual and integrated cost functions for laboratory estimates of σ and V_p in $\phi - S_w$ domain. Both electrical and ultrasonic laboratory data represent the frequency range of 1 kHz - 1MHz. The global minimum can not be determined from the individual cost function of σ over the whole frequency range. This is due to the small variation of σ values with frequency at high salinities. Contrary to the electrical cost function, the individual V_p cost function reveals a possible global minimum. However, this minimum is not sharp, thus it can lead to wrong estimates of the reservoir properties. The integrated σ and V_p cost function leads to robust estimates of ϕ and S_w values. This is explicitly shown by the dark blue point on the figure.

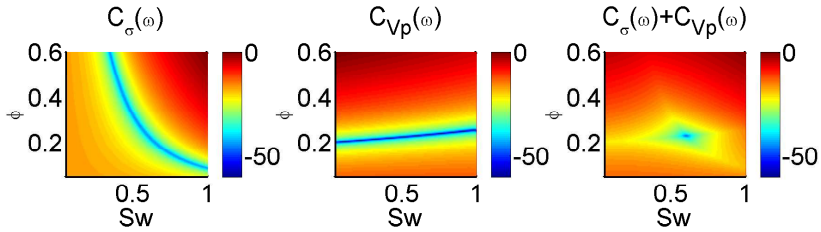

Figure 7.6: Individual cost functions for σ, V_p and integrated cost function for σ and V_p in the $\phi - S_w$ domain in the frequency range of 100 kHz .

7

7.4. CONCLUSION

A new approach for quantitative integration of acoustic/ultrasonic and electrokinetic data is presented. It has been observed that the poroelastic and electrokinetic response of a granular material can differ in such a way that their combination gives unique estimates of in-situ and lab-based permeability and porosity (or water saturation and porosity) simultaneously. This knowledge is used in the integration of complex conductivity and permittivity with velocity dispersion and attenuation in a cost function by using the pertinent electrokinetic and poroelastic theories. Realistic numerical simulations show that the estimated values of permeability and porosity are robust against uncertainties in the employed physical mechanism and in the data. The approach is analyzed for the field scale and tested on laboratory data. The results show a high potential of this method for characterization of reservoir rocks.

8

CONCLUSIONS

To conquer fear is the beginning of wisdom

Bertrand Russell

1. A new laboratory setup for electrical and ultrasonic characterization of the processes occurring in the reservoir rock is developed. Various fluid injection scenarios show that the setup can be used for CO_2 storage monitoring purposes. The presence of CO_2 in the pore space gives the contrast in bulk electrical and seismic properties, which is relevant to geoelectrical and seismic methods. This consequently allows for a quantitative prediction of the pore contents, influence of pressure, temperature and salinity of the pore water. Finally, the conductivity and permittivity measurements show minor alterations due to the change of the CO_2 phase from vapor to liquid and consequently supercritical conditions. Theses changes are rather occurring due to elevations in temperature in the reservoir rock.

2. Analytical expressions for the electrokinetic response of immobile grains representative for (un)compacted sands and sandstones in an electrolyte solution are presented. The grains can be charged and the associated electrolyte can be of any ionic strength. The main assumption made is that the grains' double layers do not overlap. The extension to spheroidal particles and polydisperse grains is given. Two main expressions are presented, one based on the Maxwell-Wagner and the other on the Bruggeman formalism. It is found that both expressions lead to not so different results, and that they could correctly reproduce the features of some representative measured data given in the third section, using at most two adjustable parameters. These parameters, the mean particle size and the particle's mean surface charge (or the mean particle size and mean Dukhin number) are found to

be in the range of what can be expected for sands and sandstones. Percolation thresholds are not considered, nor is pore clogging. This implies that the models are valid for porous media in which each particle (grain) has nearly all of its surface in contact with the electrolyte.

3. It is shown that the electrokinetic response of a porous sandstone saturated with NaCl solutions of different concentrations can correctly be modeled using a new protocol. The model accounts for 3 distinct polarization phenomena: electrode polarization, bulk polarization, and pseudo-inductance effect. The electrode polarization response is correctly predicted in this case using $\varepsilon_{ep} = \varepsilon_{bulk}$ for all investigated concentrations. The pseudo-inductance effect can also be accounted for using only one adjustable parameter. The characteristic frequency ω_L is attributed to the pseudo-inductance effect. In the frequency range ω_{ep} - ω_L, the contribution of bulk polarization is dominant. With no adjustable parameters, the bulk response of the sandstone can be predicted.

4. Two Bentheimer sandstone samples (of different geometries), flooded repetitively by either CO_2 or saline water of different NaCl concentrations, are investigated using spectral induced polarization. For the first time, such measurements are carried out in the laboratory at carbon capture and storage (CCS) reservoir conditions (P≈80 bar, T≈43°C) using a multiple electrode pair system. These experiments enabled us to follow the supercritical CO_2 front in time along the length of the samples.

   The model of complex electrical conductivity including different polarization mechanisms is presented. It is found that the effective porosity and α coefficients in the model can uniquely be determined by fitting the measurements obtained for a fully saturated sandstone sample with a known electrolyte. The model is extended to account for partial saturation. This led to the inclusion of an additional saturation parameter S_w^n in the definition of electrical conductivity.

   Once the porosity and α are found by fitting the impedance spectrum of a reservoir rock, which is saturated with an electrolyte of known concentration (S_w^n=1), it is possible to fit the impedance spectrum of the same rock which is saturated with a fluid of unknown salinity and saturation. A unique set of parameters (S_w^n, Cs) is then found. The fitting is possible due to the fact that the pseudo-inductance effect which is observed at high frequencies is very sensitive to S_w^n.

5. The velocity dispersion and attenuation are estimated during water imbibition and CO_2 drainage of sandstone at ultrasonic frequencies. The obtained estimates in water-saturated rock are verified by employing classical Biot theory. The sensitivity of the estimates is investigated by adjusting the pore pressure from 10 bar to 95 bar. Velocity and attenuation estimates show strong sensitivity to pore pressure changes of CO_2-saturated reservoir rock. The effect of CO_2 channeling is captured by velocity dispersion and attenuation during CO_2 drainage at reservoir conditions. The obtained estimates in water-saturated rock are predicted using Biot models. The partial and patchy saturations are used to predict reservoir properties of a partially saturated sandstone. This work suggests that velocity dispersion and

attenuation can potentially be used for characterization of the CO_2-stored reservoir. CT-scan experiments might provide valuable insight into the correlation of multiphase saturation experiments with velocity dispersion estimates of partially saturated rock.

6. A new approach for quantitative integration of ultrasonic and electrokinetic data is developed. It has been found that the poroelastic and electrokinetic responses of a granular material can differ in such a way that their combination gives unique estimates of permeability and porosity (or water saturation and porosity) simultaneously. This finding is used in the integration of complex conductivity and permittivity with velocity dispersion and attenuation in a cost function by using the electrokinetic and classical Biot theories. Realistic numerical simulations show that the estimated values of permeability and porosity are robust against uncertainties in the employed physical mechanism and in the data. The approach is analyzed for the field scale and tested on laboratory data. The results show a high potential of this method for characterization of reservoir rocks.

REFERENCES

F. Abdulsamad, N. Florsch, M. Schmutz, and Camerlynck C. Assessing the high frequency behavior of non-polarizable electrodes for spectral induced polarization measurements. *J. of Appl. Geoph.*, 135:449–455, 2016.

L. Adam, M. Batzle, K.T. Lewallen, and K. van Wijk. Seismic wave attenuation in carbonates. *J. of Geoph. Res.*, 114:B06208, 2009.

B. L. Alemu, E. Aker, M. Soldal, O. Johnsen, and P. Aagaard. Effect of sub-core scale heterogeneities on acoustic and electrical properties of a reservoir rock: a CO_2 flooding experiment of brine saturated sandstone in a computed tomography scanner. *Geoph. Prosp.*, 61(14):235–250, 2013.

G. E. Archie. The electrical resistivity log as an aid in determining some reservoir characteristics. *Petr. Trans. of AIME*, 146:54–62, 1942.

R. Arts, R. Elsayed, L. van der Meer, O. Eiken, S. Ostmo, and A. Chadwick. Estimation of the mass of injected CO_2 at Sleipner using time-lapse seismic data. *64th EAGE Conference*, page 4, 2002.

R. Arts, O. Eiken, A. Chadwick, P. Zweigel, L. van der Meer, and B. Zinszner. Monitoring of CO_2 injected at Sleipner using time-lapse seismic data. *Energy*, 29:1383–1392, 2004.

J. Barrière, C. Bordes, D. Brito, P. Sénéchal, and H. Perroud. Laboratory monitoring of P waves in partially saturated sand. *Geophys. J. Int.*, 191:1152–1170, 2012.

M.L. Batzle, D. Han, and R. Hofmann. Fluid mobility and frequency-dependent seismic velocity-direct measurements. *Geophysics*, 71:N1–N9, 2006.

S. H. Behrens and D. G. Grier. The charge of glass and silica surfaces. *The J. of Chem. Ph.*, 115(14):6716–6721, 2001.

P. Bergmann, C. Schmidt-Hattenberger, D. Kiessling, C. Rücker, T. Labitzke, J. Henninges, G. Baumann, and H. Schütt. Surface-downhole electrical resistivity tomography applied to monitoring of CO_2 storage at Ketzin, Germany. *Geophysics*, 77(6):B253–B267, 2012.

O. Bernard, W. Kunz, P. Turq, and L. Blum. Conductance in electrolyte solutions using the mean spherical approximation. *J. Phys. Chem.*, 96:9833–3840, 1992.

J. J. Bikerman. Electrokinetic equations and surface conductance. a survey of the diffuse double layer theory of colloidal solutions. *Trans. of the Faraday Soc.*, 36:154–160, 1940.

A. Binley, L. D. Slater, M. Fukes, and G. Cassiani. Relationship between spectral induced polarization and hydraulic properties of saturated and unsaturated sandstone. *Water Resour. Res.*, 41:W12417, 2005.

M. A. Biot. Theory of propagation of elastic waves in a fluid saturated porous solid, I: Low frequency range. *J. Acoust. Soc. Am.*, 28:168–178, 1956a.

M. A. Biot. Theory of propagation of elastic waves in a fluid saturated porous solid, II: High frequency range. *J. Acoust. Soc. Am.*, 28:179–191, 1956b.

M. A. Biot. Mechanics of deformation and acoustic propagation in porous media. *J. of Appl. Phys.*, 3(4):1482–1498, 1962.

A. Bolève, A. Crespy, A. Revil, F. Janod, and J. L. Mattiuzzo. Streaming potentials of granular media: Influence of the Dukhin and Reynolds numbers. *J. of Geoph. Res.*, 112(1): B08204, 2007.

F. D. Börner, J. R. Schopper, and A. Weller. Evaluation of transport and storage properties in the soil and groundwater zone from induced polarization measurements. *Geophys. Prospect.*, 44:583–601, 1996.

J. H. Börner, V. Herdegen, J.-U. Repke, and K. Spitzer. The impact of CO_2 on the electrical properties of water bearing porous media - laboratory experiments with respect to carbon capture and storage. *Geoph. Prosp.*, 61:446–460, 2013.

J. H. Börner, V. Herdegen, J.-U. Repke, and K. Spitzer. The electrical conductivity of CO_2−bearing pore waters at elevated pressure and temperature: a laboratory study and its implications in co_2 storage monitoring and leakage detection. *Geophys. J. Int.*, 203:1072–1084, 2015.

J. H. Börner, V. Herdegen, J.-U. Repke, and K. Spitzer. Spectral induced polarization of the three-phase system CO_2 – brine – sand under reservoir conditions. *Geophys. J. Int.*, 208(1):289–305, 2016.

T. Bourbiè, O. Coussy, and B Zinszner. *Acoustics of porous media*. Houston, TX: Gulf Publishing Co., 1987.

R. P. Buck. Diffuse layer charge relaxation at the ideally polarized electrode. *J. Electroanal. Chem.*, 23:219–240, 1969.

A. E. Bussian. Electrical conductance in a porous medium. *Geophysics*, 48(9):1258–1268, 1983.

T. Cadoret, D. Marion, and B. Zinszner. Influence of frequency and fluid distribution on elastic wave velocities in partially saturated limestones. *J. Geophys. Res.*, 100(B6): 9789–9803, 1995.

A. Chadwick, R. Arts, C. Bernstone, F. May, S. Thibeau, and P. Zweigel. *Best practice for the storage of CO_2 in saline aquifers*. Keyworth, Nottingham, 2008.

C. Chassagne and D. Bedeaux. The dielectric response of a colloidal spheroid. *J. Coll. Interf. Sc.*, 326:240–253, 2008.

C. Chassagne, D. Bedeaux, and G. J. M. Koper. Dielectric response of colloidal spheres in non-symmetric electrolytes. *Physica A*, 317:321–344, 2003.

C. Chassagne, F. Mietta, and J.C. Winterwerp. Electrokinetic study of kaolinite suspensions. *J. Coll. Interf. Sc.*, 336:352–359, 2009.

C. Chassagne, E. Dubois, M. L. Jimenez, J. P. M. van der Ploeg, and J. van Turnhout. Compensating for electrode polarization in dielectric spectroscopy studies of colloidal suspensions: theoretical assessment of existing methods. *Frontiers in Chemistry*, 4(30): 1–19, 2016.

N. B. Christensen, D. Sherlock, and K. Dodds. Monitoring CO_2 injection with cross-hole electrical resistivity tomography. *Expl. Geophys.*, 37:44–49, 2006.

P. Cosenza, A. Ghorbani, A. Revil, M. Zamora, M. Schmutz, D. Jougnot, and N. Florsch. A physical model of the low-frequency electrical polarization of clay-rocks. *J. Geophys. Res.*, 113:B08204, 2008.

B. Dafflon, Y. Wu, S. S. Hubbard, J. T. Birkholzer, T. M. Daley, J. D. Pugh, J. E. Peterson, and R. C. Trautz. Monitoring CO_2 intrusion and associated geochemical transformations in a shallow groundwater system using complex electrical methods. *Environmental Science and Technology*, 47:314–321, 2013.

T. M. Daley, L. R. Myer, J.E. Peterson, E. L. Majer, and G. M. Hoversten. Time-lapse cross-well seismic and VSp monitoring of injected CO_2 in a brine aquifer. *Environ. Geol.*, 54: 1657–1665, 2008.

E. H. DeLacey and L. R. White. Dielectric response and conductivity of dilute suspensions of colloidal particles. *J. of the Ch. Soc. , Faraday Transactions 2: Mol. and Ch. Ph.*, 77(11):2007–2039, 1981.

J. Doetsch, G. Fiandaca, E. Auken, A. V. Christiansen, A. G. Cahill, and R. Jakobsen. Field-scale time-domain spectral induced polarization monitoring of geochemical changes induced by injected CO_2 in a shallow aquifer. *Geophysics*, 80(2):WA113—-WA126, 2015.

H. R Dukhin. *Colloid Science: Volume I: Irreversible Systems (Volume 1)*. Elsevier, 1952.

S. S. Dukhin. *Dielectric phenomena and the double layer in disperse systems and polyelectrolytes*. John Wiley and Sons, New York, 1974.

J. Dvorkin and A. Nur. Dynamic poroelasticity: A unified model with the squirt and the Biot mechanisms. *Geophysics*, 58:524–533, 1993.

European Commission. *Implementation of Directive 2009/31/EC on the Geological Storage of Carbon Dioxide. Guidance Document 2: Characterisation of the Storage Complex, CO_2 Stream Composition, Monitoring and Corrective Measures*. European Communities, 2011.

M. Fixman. Charged macromolecules in external fields. I. the sphere. *The J. of Ch. Ph.*, 72(9):5177–5186, 1980.

M. Fixman. Thin double layer approximation for electrophoresis and dielectric response. *The J. of Ch. Ph.*, 78(3):1483–1491, 1983.

J. Fleig, J. Jamnik, and J. Maier. Inductive loops in impedance spectroscopy caused by electrical shielding. *J. Electrochem. Soc.*, 143(11):3636–3641, 1996.

A. A. Garrouch and M. M. Sharma. The influence of clay content, salinity, stress, and wettability on the dielectric properties of brine-saturated rocks: 10 Hz to 10 MHz. *Geophysics*, 59:909–917, 1994.

A. Ghorbani, P. Cosenza, S. Ruy, C. Doussan, and N. Florsch. A variational non-invasive monitoring of water infiltration in a silty clay loam soil using spectral induced polarization. *Water. Resour. Res.*, 44:W08402, 2008.

R. Ghose and E. C. Slob. Quantitative integration of seismic and GPR reflections to derive unique estimates for water saturation and porosity in subsoil. *Geoph. Res. Let*, 33(5): L05404, 2006.

P. W. J. Glover, P. G. Meredith, P. R. Sammonds, and S. A. F. Murrell. Ionic surface electrical conductivity in sandstone. *J. Geoph. Res.*, 99(B11):21635–21650, 1994.

C. Grosse. Relaxation mechanisms of homogeneous particles and cells suspended in aqueous electrolyte solutions. In A. Delgado, editor, *Interfacial Electrokinetics and Electrophoresis*, volume 106, pages 279–327. Marcel Dekker, Inc, 2002.

C. Grosse and A. V. Delgado. Dielectric dispersion in aqueous colloidal systems. *Current Op. in Col. and Int. Sc.*, 15(3):145–159, 1984.

E. J. Hinch, J. D. Sherwood, W. C. Chew, and P. N. Sen. Dielectric response of a dilute suspension of spheres with thin double layers in an asymmetric electrolyte. *J.of the Ch. Soc., Faraday Transactions 2: Mol. and Ch. Ph.*, 80(5):535–551, 1984.

A. D. Hollingsworth and D. A. Saville. A broad frequency range dielectric spectrometer for colloidal suspensions: cell design, calibration, and validation. *J. of Col. Int. Sc.*, 257: 65–76, 2003.

Y. Jeng, J. Tsai, and S. Chen. An improved method of determining near-surface Q. *Geophysics*, 64:1608–1617, 1999.

D. L. Johnson. Theory of frequency dependent acoustics in patchy saturated porous media. *J.of Acoust. Soc. of Amer.*, 110:682–694, 2001.

T. C. Johnson, M. Oostrom, M. J. Truex, J. N. Thomle, and T. W. Wietsma. Determination of water saturation using gas phase partitioning tracers and time-lapse electrical conductivity measurements. *Vadose Zone J.*, 12(2):1–14, 2013.

D. Jougnot, A. Ghorbani, A. Revil, P. Leroy, and P. Cosenza. Spectral induced polarization of partially saturated clay-rocks: a mechanistic approach. *Geophys. J. Int.*, 180(1): 210–224, 2010.

M. Kavian, E.C. Slob, and W.A. Mulder. Measured electric responses of unconsolidated layered and brine-saturated sand and sand-clay packs under continuous fluid flow conditions. *Journal of Applied Geophysics*, 80:83–90, 2012.

A. Kemna, A. Binley, G. Cassiani, E. Niederleithinger, A. Revil, L. Slater, K. H Williams, A. Flores Orozco, F. H. Haegel, A. Hördt, S. Kruschwitz, V. Leroux, K. Titov, and E. Zimmermann. An overview of the spectral induced polarization method for near-surface applications. *Near Surface Geophysics*, 10:453–468, 2012.

D. Kiessling, C. Schmidt-Hattenberger, H. Schuett, K. Schilling, H. Krueger, B. Schoebel, E. Danckwardt, J. Kummerow, and the CO2SINK Group. Geoelectrical methods for monitoring geological CO_2 storage: First results from cross-hole and surface–downhole measurements from the CO2SINK test site at Ketzin (Germany). *International Journal of Greenhouse Gas Control*, 4:816–826, 2010.

A. J. Kijlstra, H. P. van Leeuwen, and J. Lyklema. Effects of surface conduction on the electrokinetic properties of colloid. *J. of the Chem. Soc. Faraday Trans.*, 88(23):3441–3449, 1992.

J. Kim, M. J. Nam, and T. Matsuoka. Estimation of CO_2 saturation during both CO_2 drainage and imbibition processes based on both seismic velocity and electrical resistivity measurements. *Geoph. J. Int.*, 195(1):292–300, 2013.

J. Kim, M. J. Nam, and T. Matsuoka. Monitoring CO_2 drainage and imbibition in a heterogeneous sandstone using both seismic velocity and electrical resistivity measurements. *Expl. Geoph.*, 47(1):24–31, 2016.

A. Kirichek, R. Ghose, and H. K. J. Heller. Laboratory monitoring of CO_2 migration and phase transition using complex electrical conductivity. *75th EAGE Conference and Exhibition*, page We 10 10, 2013a.

A. Kirichek, R. Ghose, and H. K. J. Heller. Laboratory monitoring of CO_2 migration within brine-saturated reservoir rock though complex electrical impedance. *SEG Technical Program Expanded Abstracts*, pages 2742–2746, 2013b.

A. Kirichek, C. Chassagne, and R. Ghose. Dielectric spectroscopy of granular material in an electrolyte solution of any ionic strength. *Coll. and Surf. A: Physicochem.l and Eng. Asp.*, 533:356–370, 2017.

R. J. Knight. Hysteresis in the electrical resistivity of partially saturated sandstones. *Geophysics*, 56:2139–2147, 1991.

K. Koch, A. Revil, and K. Holliger. Relating the permeability of quartz sands to their grain size and spectral induced polarization characteristics. *Geophys. J. Int.*, 190:230–242, 2012.

T. Kremer, M. Schmutz, A. Maineult, and P. Agrinier. Laboratory monitoring of CO_2 injection in saturated silica and carbonate sands using spectral induced polarization. *Geophys. J. Int.*, 207:1258–1272, 2016.

L.D. Landau and E.M. Lifshitz. *The course of theoretical physics. The theory of elasticity (Volume 7)*. Pergamon Press, 1970.

M. Lebedev, J. Toms-Stewart, B. Clennell, Pervukhina M., V. Shulakova, L. Paterson, T. M. Möller, B. Gurevich, and F. Wenzlau. Direct laboratory observation of patchy saturation and its effects on ultrasonic velocities. *The Leading Edge*, 28(1):24–27, 2009.

M. Lebedev, V. Mikhaltsevich, O. Bilenko, T. Dance, M. Pervukhina, and B. Gurevich. Experimental laboratory study on the acoustic response of sandstones during injection of supercritical CO_2 on CRC2 sample from otway basin australia. *Energy Procedia*, 37: 4106 – 4113, 2013.

X. Lei and Z. Xue. Ultrasonic velocity and attenuation during CO_2 injection into water-saturated porous sandstone: Measurements using difference seismic tomography. *Physics of the Earth and Planetary Interiors*, 176:224–234, 2009.

P. Leroy and A. Revil. A mechanistic model for the spectral induced polarization of clay materials. *J. Geophys. Res.*, 114:1–21, 2009.

P. Leroy, A. Revil, A. Kemna, P. Cosenza, and A. Ghorbani. Complex conductivity of water-saturated packs of glass beads. *J. of Colloid and Int. Sc.*, 321:103–117, 2008.

D. P. Lesmes and K. M. Frye. Influence of pore fluid chemistry on the complex conductivity and induced polarization responses of Berea sandstone. *J. Geophys. Res.*, 106(B3): 4079–4090, 2001.

S. Lüth, P. Bergmann, C. Cosma, N. Enescu, R. Giese, J. Götz, A. Ivanova, C. Juhlin, A. Kashubin, C. Yang, and F. Zhang. Time-lapse seismic surface and down-hole measurements for monitoring CO_2 storage in the CO2SINK project (Ketzin, Germany). *Energy Procedia*, 4:3435–3442, 2011.

V. F. Lvovich. *Impedance spectroscopy: Applications to Electrochemical and Dielectric Phenomena*. John Wiley and Sons, New York, 2012.

J. Lyklema and M. Minor. On surface conduction and its role in electrokinetics. *Coll. and Surf. A: Physicochem. and Eng. Asp.*, 140(1):33–41, 1998.

J. Lyklema, S. S. Dukhin, and V. N. Shilov. The relaxation of the double layer around colloidal particles and the low-frequency dielectric dispersion: PartI. theoretical considerations. *J. of El. Chem. and Int. Electrochem.*, 143(1):1–21, 1983.

J. R. MacDonald and W. R. Kenan. *Impedance Spectroscopy*. John Wiley and Sons, New York, 1987.

C.S. Mangelsdorf and L.R. White. Dielectric response of a dilute suspension of spherical colloidal particles to an oscillating electric field. *J. Chem. Soc. Faraday Trans.*, 93(17): 3145–3154, 1997.

G. Marketos and A.I. Best. Application of the BISQ model to clay squirt flow in reservoir sandstones. *J. of Geoph. Res.*, 115:B06209, 2010.

D. J. Marshall and T. R. Madden. Induced polarization, a study of its causes. *Geophysics*, 24:790–816, 1959.

H. P. Maruska and J. G. Stevens. Technique for extracting dielectric permittivity from data obscured by electrode polarization. *IEEE Trans. El. Ins.*, 23(2):197–200, 1988.

G. Mavko and R. Nolen-Hoeksema. Estimating seismic velocities at ultrasonic frequencies in partially saturated rocks. 1994.

G. Mavko and A. Nur. Wave propagation in partially saturated rocks. *Geophysics*, 44: 161–178, 1979.

G. Mavko, T. Mukerji, and J. Dvorkin. *The Rock Physics Handbook*. Campridge University Press, 2009.

S. I. Mayr and H. Burkhardt. Ultrasonic properties of sedimentary rocks: effect of pressure, saturation, frequency and microcracks. *Geoph. J. Int.*, 164(1):246–258, 2006.

J.B. Molyneux and D.R. Schmitt. Compressional-wave velocities in attenuating media: A laboratory physical model study. *Geophysics*, 65:1162–1167, 2000.

T.M. Müller, B. Gurevich, and M Lebedev. Seismic wave attenuation and dispersion resulting from wave-induced ow in porous rocks: A review. *Geophysics*, 75:A147–A164, 2010.

Y. Nakatsuka, Z. Xue, Y. Yamada, and T. Matsuoka. Experimental study on CO_2 monitoring and quantification of stored CO_2 in saline formations using resistivity measurements. *Int. J. of Greenhouse Gas Control*, 4:209–216, 2010.

Q. Niu, A. Revil, and M. Saidian. Salinity dependence of the complex surface conductivity of the portland sandstone. *Geophysics*, 81(2):D125–D140, 2016.

R. W. O'Brien. The response of a colloidal suspension to an alternating electric field. *Adv.in Col. and Int. Sc.*, 16(1):281–320, 1982.

R. W. O'Brien. The high-frequency dielectric dispersion of a colloid. *J. of Col. and Int. Sc.*, 113(1):81–93, 1986.

G. Okay, P. Leroy, A. Ghorbani, P. Cosenza, C. Camerlynck, J. Cabrera, N. Florsch, and A. Revil. Spectral induced polarization of clay-sand mixtures: Experiments and modeling. *Geophysics*, 79:E353–E375, 2014.

C. T. O'Konski. Effect of interfacial conductivity on dielectric properties. *The J. of Ch. Ph.*, 23(8):1559, 1955.

C. T. O'Konski. Electric properties of macromolecules. v. theory of ionic polarization in polyelectrolytes. *The J. of Ch. Ph.*, 64(5):605–619, 1960.

G. R. Olhoeft. Direct detection of hydrocarbon and organic chemicals with ground-penetrating radar and complex resistivity: Petroleum, hydrocarbons and organic chemicals, in proceedings of the NWWA/API conference on petroleum hydrocarbons and organic chemicals in ground water prevention. *Detection and Restoration*, pages 119–139, 1986.

A. E. Peksa, K.-H.A.A. Wolf, and P.L.J. Zitha. Bentheimer sandstone revisited for experimental purposes. *Mar.and Petr. Geology*, 67:701–719, 2015.

S.R. Pride, J.G. Berryman, and J.M. Harris. Seismic attenuation due to wave-induced flow. *J. of Geoph. Res.*, 109:BO1201, 2004.

C. Purcell, A. Mur, Y. Soong, R. Mclendon, I.V. Haljasmaa, and W. Harbert. Integrating velocity measurements in a reservoir rock sample from the SACROC unit with an AVO proxy for subsurface supercritical CO_2. *The Leading Edge*, 29:192–195, 2010.

A. Revil. On charge accumulation in heterogeneous porous rocks under the influence of an external electric field. *Geophysics*, 78(4), 2013.

A. Revil and L. M. Cathles. Permeability of shaly sands. *Wat. Res. Res.*, 35(3):651–662, 1999.

A. Revil and N. Florsch. Determination of permeability from spectral induced polarization in granular media. *Geoph.J. Int.*, 181(3):1480–1498, 2010.

A. Revil and P. W. J. Glover. Theory of ionic-surface electrical conduction in porous media. *Phys. Rev. B*, 55:1757–1773, 1997.

A. Revil, M. Karaoulis, T. Johnson, and A. Kemna. Review: Some low-frequency electrical methods for subsurface characterization and monitoring in hydrogeology. *Hydrogeology Journal*, 20:617–658, 2012.

A. Revil, P. Kessouri, and C. Torres-Verdèn. Electrical conductivity, induced polarization, and permeability of the Fontainebleau sandstone. *Geophysics*, 79(5), 2014.

J. A. Reynolds and J. M. Hough. Formulae for dielectric constant of mixtures. *Proceedings of the Physical Society: Section B*, 70(8):769, 1957.

L. A. Rosen, J. C. Baygents, and D. A. Saville. The interpretation of dielectric response measurements on colloidal dispersions using the dynamic Stern layer model. *The J.of Chem. Physics*, 98(5):4183, 1993.

W.B. Russel, D.A. Saville, and W.R. Schowalter. *Colloidal dispersions*. Cambridge University Press, Cambridge, 1989.

W. Scheider. Theory of the frequency dispersion of electrode polarization. topology of networks with fractional power frequency dependence. *J. Phys. Chem.*, 79(2):127–136, 1975.

C. Schmidt-Hattenberger, P. Bergmann, T. Labitzke, S. Schröder, K. Krüger, C. Rücker, and H. Schütt. Monitoring of geological CO_2 storage with electrical resistivity tomography (ERT): Results from a field experiment near Ketzin/Germany. *Berichte Geol. B.-A.*, 93: 75–81, 2011.

C. Schmidt-Hattenberger, P. Bergmann, D. Bössing, T. Labitzke, M. Möller, S. Schröder, F. Wagner, and H. Schütt. Electrical resistivity tomography (ert) for monitoring of co_2 migration – from tool development to reservoir surveillance at the ketzin pilot site. *Energy Proc.*, 37:4268–4275, 2015.

M. Schmutz, A. Revil, P. Vaudelet, M. Batzle, P. Femenía Viñao, and D. D. Werkema. Influence of oil saturation upon spectral induced polarization of oil bearing sands. *Geophys. J. Int.*, 183:211–224, 2010.

G. Schwarz. A theory of the low-frequency dielectric dispersion of colloidal particles in electrolyte solution. *The J. of Ph. Chem.*, 66(12), 1962.

P. N. Sen, Scala C., and M. H. Cohen. A self-similar model for sedimentary rocks with application to the dielectric constant of fused glass beads. *Geophysics*, 46:781–795, 1981.

M. Shahidi, J. B. Hasted, and A. K. Jonscher. Electrical properties of dry and humid sand. *Nature*, 258:595–597, 1975.

J.-Q. Shi, Z. Xue, and S. Durucan. Seismic monitoring and modelling of supercritical CO_2 injection into a water-saturated sandstone: Interpretation of P-wave velocity data. *Int. J. of Greenh. Gas Contr.*, 1:473–480, 2007.

A.F. Siggins, M. Lwin, and P. Wisman. Laboratory calibration of the seismo-acoustic response of CO_2 saturated sandstones. *Int. J. of Greenh. Gas Contr.*, 4:920–927, 2010.

D.V. Sivukhin. *The course of general physics. Mechanics (Volume 1)*. Fizmatlit/MFTI, 2005.

L. D. Slater and D. R. Glaser. Controls on induced polarization in sandy unconsolidated sediments and application to aquifer characterization. *Geophysics*, 68:1547–1588, 2003.

D. M. J. Smeulders. *On wave propagation in saturated and partially saturated porous media*. PhD thesis, 1992.

R.D. Stoll. Controls on induced polarization in sandy unconsolidated sediments and application to aquifer characterization. *Geophysics*, 68:1547–1588, 1974.

R.D. Stoll. Acoustic waves in ocean sediments. *Geophysics*, 42:715–725, 1977.

S. Subramaniyan, B. Quintal., N. Tisato, E. H. Saenger, and C. Madonna. An overview of laboratory apparatuses to measure seismic attenuation in reservoir rocks. *Geoph. Prosp.*, 62:1211–1223, 2014.

Y Sun, Q. Li, D. Yang, and X. Liu. Laboratory core flooding experimental systems for CO_2 geosequestration: An updated review over the past decade. *J. of Rock Mech. and Geotech. Eng.*, 8:113–126, 2016.

M. N. Toksöz, D. H. Johnston, and A. Timur. *Attenuation of seismic waves in dry and saturated rocks. I. Laboratory measurements.* Soc. of Expl. Geoph., 1979.

C. Ulrich and L. D. Slater. Induced polarization measurements on unsaturated, unconsolidated sands. *Geophysics*, 69:762–771, 2004.

K.N. van Dalen, R. Ghose, G.G. Drijkoningen, and D.M.J. Smeulders. In-situ permeability from integrated poroelastic reflection coefficients. *Geoph. Res. Let.*, 37:L12303, 2010.

P. Vaudelet, A. Revil, M. Schmutz, Franceschi M., and P. Bégassat. Changes in induced polarization associated with the sorption of sodium, lead, and zinc on silica sands. *J. of Colloid and Int. Sc.*, 360:739–752, 2011.

H. J. Vinegar and M. H. Waxman. Induced polarization of shaly sands. *Geophysics*, 49: 1267–1287, 1984.

B. Vogelaar. *Fluid effect on wave propagation in heterogeneous porous media.* PhD thesis, Delft University of Technology, 2009.

Z. Wang and A. Nur. Effects of CO_2 flooding on wave velocities in rocks with hydrocarbons. *SPE Reservoir Engineering*, 4(4):429–436, 1989.

Z. Wang, M. E. Cates, and R. T. Langan. Seismic monitoring of a CO_2 flood in a carbonate reservoir: A rock physics study. *Geophysics*, 63(5):1604–1617, 1998.

S. H. Ward. *Resistivity and induced polarization methods. In: Geotechnical and Environmental Geophysics.* Tulsa, SEG, 1990.

A. Weller, K. Breede, L. Slater, and S. Nordsiek. Effect of changing water salinity on complex conductivity spectra of sandstones. *Geophysics*, 76(5):F315–F327, 2011.

J.E. White. Computed seismic speeds and attenuation in rocks with partial gas saturation. *Physics of Solid Earth*, 40:224–232, 1975.

O. Wiener. Die theorie des mischkörpers für das feld der stationären strömung. erste abhandlung. die mittelwertsatze für kraft, polarisation und energie. *Abhandl. Math. Phys. Klas. Köngl. Sächs. Gesellsch. Wissensch*, 23:509–604, 1912.

K.W. Winkler and T.J. Plona. Technique for measuring ultrasonic velocity and attenuation spectra in rocks under pressure. *J. Geoph.Res.*, 87(B13):10776–10780, 1982.

C. J. Wisse. *On frequency dependence of acoustic waves in porous cylinders.* PhD thesis, 1999.

Z. Xue and X. Lei. Laboratory study of CO_2 migration in water-saturated anisotropic sandstone, based on P-wave velocity imaging. *Expl. Geoph.*, 37:10–18, 2006.

Z. Xue and T. Ohsumi. Seismic wave monitoring of CO_2 migration in water-saturated porous sandstone. *Expl. Geoph.*, 35:25–32, 2004.

Z. Xue, T. Ohsumi, and H. Koide. An experimental study on seismic monitoring of a CO_2 flooding in two sandstones. *Energy*, 30:2352–2359, 2005.

H. Yam. *CO_2 rock physics: a laboratory study.* MSc thesis, University of Alberta, 2011.

K. Zemke, A. Liebscher, and M. Wandrey. Petrophysical analysis to investigate the effects of carbon dioxide storage in a subsurface saline aquifer at Ketzin, Germany (co2sink). *Int. J. of Greenh. Gas Contr.*, 4:990–999, 2010.

A. Zhubayev. *Soil properties from seismic intrinsic dispersion.* PhD thesis, Delft University of Technology, 2014.

A. Zhubayev and R. Ghose. Contrasting behavior between dispersive seismic velocity and attenuation: Advantages in subsoil characterization. *J. of Ac.Soc.of America*, 131: EL170–EL176, 2012a.

A. Zhubayev and R. Ghose. Physics of shear-wave intrinsic dispersion and estimation of in situ soil properties: a synthetic VSP appraisal. *Near Surf. Geoph.*, 10:613–629, 2012b.

E. Zimmermann, A. Kemna, J. Berwix, W. Glaas, H. M. Münch, and J. A. Huisman. A high-accuracy impedance spectrometer for measuring sediments with low polarizability. *Meas. Sci. Technol.*, 19:105603, 2008.

C.F. Zukoski and D.A. Saville. The interpretation of electrokinetic measurements using a dynamic model of the stern layer: I. the dynamic model. *J. Colloid Interface Sci.*, 114 (1):32–44, 1986.

SUMMARY

Monitoring the properties of a CO_2 storage reservoir is important for two main reasons: firstly, to verify that the injected CO_2 is safely contained in the reservoir rock as planned, and secondly, to provide data which can be used to update the existing reservoir models and support eventual mitigation measures in case of deviation from the CO_2 storage plan. Reliable quantitative monitoring of reservoir rocks and pore-filling fluids remains a challenging task in geophysical prospecting. Typically, geophysical electrical and seismic surveys are used to predict reservoir properties. Electrical properties of rocks are strongly controlled by the chemistry of the fluids that fill the pore space. Thus, electrical surveys can provide accurate estimates of pore-filling fluid composition and porosity of reservoir rock. Seismic methods are particularly sensitive to elastic heterogeneities in the subsurface. Elastic properties of reservoir rocks can be extracted from recorded seismic data. Potentially, the simultaneous use of electrical and seismic geophysical surveys can reduce the uncertainty in the quantitative characterization of reservoir rocks. In this thesis, theoretical and experimental research is conducted to show the feasibility of such an integrated approach for a CO_2 storage reservoir.

First, a home-made multi-sensor core-flooding laboratory setup was developed. The setup allows conducting continuous dielectric spectroscopy and ultrasonic measurements during imbibition and drainage experiments under reservoir pressure/temperature conditions. A number of CO_2/water injection scenarios has been performed, showing the sensitivity of measured electrical impedance and ultrasonic response of a fully or partially saturated Bentheimer sandstone under different pressure and temperature conditions. An array of electrodes and ultrasonic transducers has been used to monitor the CO_2 propagation and CO_2 phase transition between vapor, liquid and supercritical fluid within the sandstone's pore space. The measured data is used to derive the electrical conductivity and dielectric permittivity spectra, and the P-wave velocity dispersion and attenuation changes in the (partially) saturated sandstone.

Next, new analytical expressions for the dielectric (electrokinetic) response of saturated porous media are developed. The low-frequency (0.01 Hz - 10 MHz) response of reservoir rocks and soils is until now always modeled using theories based on the work of Schwartz. The theory for the low-frequency electrokinetic signature of suspensions, on the other hand, has been developed much further over the last decades both numerically and analytically. In the new models the grains of porous rock can be charged and the associated electrolyte can be of any ionic strength. In the present research, a main assumption made is that the grains' double layers do not overlap significantly. The extension to spheroidal particles and polydisperse grains is obtained. Two main expressions for the complex conductivity are presented here, one based on the Maxwell-Wagner and the other on the Bruggeman formalism. It is found that both expressions lead to not so different results, and that they could correctly reproduce the features of some representative measured data using at most two adjustable parameters. These parameters, the

mean particle size and the particle's mean surface charge (or the mean particle size and mean Dukhin number) are found to be in the range of what can be expected for investigated samples. Percolation thresholds are not considered, nor is pore clogging. This implies that the models are valid for porous media in which each grain has nearly all of its surface in contact with the electrolyte.

The interpretation of dielectric measurements in a 2-electrode systems is a challenging task due to the presence of different polarization effects. An integrated model is developed in this research which accounts for not only the bulk material polarization, but also two other effects that appear in the laboratory measurements. The first one is related to electrode polarization, occurring at a very low frequency (<1 kHz). The second one, termed "pseudo-inductance effect", arises in the frequency range 10 kHz - 1 MHz. Using the full model, three spectral regions (electrode polarization, pseudo-inductance effect and bulk polarization) could be identified. The "true" bulk conductivity could be modeled using as input parameters the porosity, the conductivity of the electrolyte, and the dielectric permittivities of the grains and of water.

The dielectric spectroscopy measurements presented in this thesis have been performed on a Bentheim sandstone saturated with either CO_2 or saline water. The response of the water imbibition and CO_2 drainage experiment is captured using two types of multi-electrode arrays under realistic reservoir pressure and temperature conditions of a sequestrated CO_2 reservoir. The developed model is adapted for the present measurements by including a saturation coefficient as defined in Archie's law, in order to evaluate the CO_2 saturations of the cores. In particular, it is shown that by fitting the measurements with the model a unique set of parameters (electrolyte concentration and water saturation) can be found for a sandstone of known porosity but a fluid of unknown salinity and saturation.

The velocity dispersion and attenuation estimates are obtained during water imbibition and CO_2 drainage of Bentheimer sandstone in the laboratory at ultrasonic frequencies. These estimates show a strong sensitivity to pore pressure changes of the CO_2-saturated reservoir rock. The pore pressure is varied from 10 bar to 95 bar and the temperature from 27 °C to 33°C to monitor the transition between vapor, liquid and supercritical CO_2. During these experiments the CO_2 and water are consecutively injected into the pore space of the sandstone. The obtained estimates in fully- and partially-saturated sandstone are analyzed using the theory of poroelasticity. It is shown how the partial and patchy saturation descriptions can be used for predicting water saturation of the CO_2-bearing sandstone from velocity dispersion estimates.

Finally, it has been observed that the poroelastic and electrokinetic response of a granular material can be combined in such a way that they provide unique estimates of permeability and porosity (or water saturation and porosity). This knowledge is used in the integration of the complex conductivity and permittivity with velocity dispersion and attenuation in a cost function, by using the electrokinetic and poroelastic theories. Realistic numerical simulations show that the estimated values of permeability and porosity are robust against uncertainties in the employed physical mechanism and in the data. The frequency range of of 1 Hz - 5 MHz is analyzed. The approach is analyzed for the field scale and tested on laboratory data. The results show a high potential of this method for the characterization of reservoir rocks.

SAMENVATTING

Samenvatting in het Nederlands...

LIST OF PUBLICATIONS

1. **Kirichek, A., Ghose, R. and Heller, H. K. J**, *Laboratory monitoring of CO_2 migration and phase transition using complex electrical conductivity*, 75th EAGE Conference and Exhibition, We 10 10 (2013).

2. **Kirichek, A., Ghose, R. and Heller, K.**, *Laboratory monitoring of CO_2 migration within brine-saturated reservoir rock though complex electrical impedance*, SEG Technical Program Expanded Abstracts, 2742-2746 (2013).

3. **Draganov, D., Kirichek, A., Heller, K. and Ghose, R.**, *Laboratory measurements monitoring supercritical CO_2 sequestration using ghost reflections retrieved by seismic interferometry*, SEG Technical Program Expanded Abstracts, 5516-5520 (2016).

4. **Kirichek, A., Chassagne, C. and Ghose, R.**, *Dielectric spectroscopy of granular material in an electrolyte solution of any ionic strength*, Coll. and Surf. A: Physicochem. and Eng. Asp. **533**, 356-370 (2017).

5. **Kirichek, A., Chassagne, C. and Ghose, R.**, *Predicting the dielectric response of saturated sandstones using a 2-electrode measuring system (on review)*, Geoph. J. Int..